PhD-FSTC-2016-12
The Faculty of Sciences, Technology and Communication

DISSERTATION

Defence held on 15/04/2016 in Luxembourg

to obtain the degree of

DOCTEUR DE L'UNIVERSITÉ DU LUXEMBOURG

EN SCIENCES DE L'INGÉNIEUR

by

Lin WANG
Born on 17 February 1989 in Jiangxi, PR. China

REGIONAL CONTINENTAL WATER STORAGE VARIATIONS INFERRED FROM THREE-DIMENSIONAL GPS COORDINATES TIME SERIES

Dissertation defence committee

Dr Tonie Van Dam, dissertation supervisor
Professor, Université du Luxembourg

Dr Olivier Francis, Chairman
Professor, Université du Luxembourg

Dr Nico Sneeuw, Vice Chairman
Professor, Universität Stuttgart

Dr Jürgen Kusche
Professor, Rheinische Friedrich-Wilhelms-Universität Bonn

Dr Patrick Matgen
Lead Research and Technology Associate, Luxembourg Institute of Science and Technology

Abstract

Recent advances in space geodetic techniques (including but is not limited to, Global Navigation Satellite System, GNSS, Very-long-baseline interferometry, VLBI) allow us to observe changes in continental water storage (CWS) depending on the extend and the amplitude of the load. Among the geodetic techniques, GPS is the most common observational tool because of its global distribution. GPS observations are used for many fields of studies, including seismology and tectonics. This thesis presents a method to obtain regional changes in continental water storage by inverting the three-dimensional GPS time series.

The error sources from a regional study are studied first. In theory, the surface motions from each GPS station are caused by loads acting over the entire surface of the Earth. As we are only interested in the changing water storage in a particular region, the loading signal from the far field, outside the region of interest, must be accounted for. From our simulation studies, we conclude that the mass changes locate outside of the study region cannot be neglected. We find that the coverage of the area need to extend to about 20 degrees (about 20 000 km) of the basin center for a regional study.

The second concern is the GPS time series. We find discrepancies over the globe between GPS observed displacements and forward modelled displacements using models of water storage. At annual periods, the thermal expansion of the GPS monuments and underlying bedrock, atmospheric loading, and the draconitic signal if not

accounted for will introduce an error into the inversion. These errors may contribute to the disagreement between our forward modelled and observed ground motions. For 88% of the stations analyzed, we are able to reduce the WRMS on the GPS vertical time series by removing the modelled displacements using estimates CWS loading obtained from WaterGAP. We conclude that the most likely cause of the discrepancies come from the GPS observations themselves. Due to the observed discrepancy, we find that the uncertainties of the GPS time series should be re-estimated in any inversion study.

Finally, we determine monthly CWS variations from GPS three-dimensional coordinate time series for the major river basins in Europe and North America. The results at the basin scale are validated against GRACE and hydrological models, the correlation between inferred CWS and GRACE or models are close to 0.9 and WRMSR are as high as 50% for some basins. We also demonstrate that the relative contributions of the GPS horizontal coordinates are about one third those of the vertical signals. We prove that by including the horizontal coordinates in the inversion that we are able to improve the inversion results.

Contents

Acknowledgements

Within this Ph.D. study period, many people and groups need to be acknowledged. I know that without the help from any of you, it is definitely impossible for me to accomplish this study and make the final thesis. I would like to thank all the members of Geophysics Laboratory in University of Luxembourg. I had such a great time here and it is a truly honor to be a member among any of you.

At first, I would like to express my deepest appreciation to my supervisor, Tonie van Dam. Your patience and suggestions give me encourages when I am facing any trouble during the study. Thank you for introducing me this interesting and challenging topic. Supervisions from the co-supervisors Nico Sneeuw and Olivier Francis can also never been forgotten by me. Discussions with you just like a light tower in the dark ocean. A special thanks to un-official mentor, Matthias Weigelt. Without your help, I know that I cannot make it to the end.

Thanks to Matthias Weight, Nico Sneeuw and Balaji Devaraju for providing the GSHS software bundle for analyzing the GRACE time variable gravity field and the loading displacements calculations from Stokes coefficients.

I would like to thank Qiang Chen and German Olivier for providing me insights for the modelling the GPS errors and the corresponding error models. I appreciate Williams Simon, Weiwei Li and Addisu Hunegnaw for the helps on GPS time series analysis and the usage of the CATS and HECTOR software.

I would like to acknowledge Mohammad Tourian, Bramha Dutt Vishwakarma for the helpful discussions during my one-month visit in Stuttgart and for discussion about the leakage in the GRACE processing, respectively.

Thanks to Petra Döll for providing WaterGAP water storage dataset, Jim Ray, Zuheir

Altamimi and Xavier Collilieux for the special processing of the GPS time series of removing the discontinuity in the time series.

I appreciate Xiaoping Wu for a long and helpful discussion in the IUGG 2015 about the inversion applications of GPS time series. I appreciate Danan Dong, Zhao Li and Na Wei for the discussions on the thermal expansions.

I appreciate Raphaël De Plaen for the help of using LaTeX and Adobe Illustrator software, Sajad Tabibi for the introductions and discussions on GPS processing.

I acknowledge Luxembourg National Research Fund (FNR) and University of Luxembourg for the financial support for my Ph.D. study. I appreciate the travel award grant support from IAG Potsdam 2013.

Last but not least, I appreciate the endless encouragements and understandings from my parents and parents-in-law. I wish that I could express it by words. My wife, Wei Huang, is always supportive and patient. Without your understandings, I just cannot make this. Meeting and marrying you are the best thing in my life.

List of Tables

List of Figures

Abbreviations

ATML	ATMospheric Loading
CE	Center of Earth
CF	Center of Figure
CHAMP	CHAllenging Minisatellite Payload
CM	Center of Mass
CWS	Continental Water Storage
ECCO	Circulation and Climate of the Ocean
ECMWF	European Center for Medium Range Weather Forecasts
EWH	Equivalent Water Height
FNR	Luxembourg National Research Fund
GB	Gutenberg-Bullen
GLDAS	Global Land Data Assimilation System
GNSS	Global Navigation Satellite System
GRACE	Gravity Recovery and Climate Experiment
IERS	International Earth Rotation and Reference Systems Service

LS	Least Squares
NCAR	National Center for Atmospheric Research
NCEP	National Center for Environmental Prediction
OBP	Ocean Bottom Pressure
PREM	Preliminary Reference Earth Model
RMS	Root-Mean Square
SNR	Signal-to-Noise Ratio
STE	Spatial Truncation Error
SVD	Singular Value Decomposition
VLBI	Very-Long-Baseline Interferometry
WaterGAP WGHM	Water Global Assessment and Prognosis
WLS	Weighted Least Squares
WRMS	Weight Root Mean Squares
WRMSR	WRMS Reduction

Chapter 1. Introduction

1.1. GPS for mass loading research

The circulation of water from the ocean and land surfaces into the atmosphere and back again represents a large transport of matter in the Earth system. Continental fresh water, consisting of groundwater, soil moisture, surface water, ice, and vegetation storage, is an important natural resource, which is required by all terrestrial species including humans. Understanding changes in continental water storage are essential for water resource management and the support of daily life. In this thesis, we define continental water storage (CWS) as the total water in all its forms stored on the continents at any time epoch.

Changes in CWS had been observed by the Global Navigation Satellite System (GNSS) (e.g. van Dam et al., 1994; Wahr et al., 2001; Plag and van Dam, 2002) and Very-long-baseline interferometry (VLBI) (e.g. van Dam and Herring, 1994; Petrov and Boy, 2004; Tesmer et al., 2009; McMillan et al., 2013). In the literatures, GPS observations are the most common technique for observing CWS reported due to its global distribution. These stations are used for many fields of studies, especially seismology and tectonics.

The theory of estimating the amplitude of environmental loading signals in geodetic observations using global atmospheric mass was first introduced by (van Dam and Wahr, 1987). van Dam and Wahr (1987) demonstrated that GPS coordinate time series could be explained by atmospheric loading induced displacements. Since

then, may papers have been written on the analysis of environmental loading using GPS. Based on classical loading theory from Farrell (1973), we know that surface displacements observed by any GPS site are particularly sensitive to the mass changes in the near field. For example, numerous studies have demonstrated that GPS is able to detect the elastic response of the Earth to changes in water storage (or ice mass) at regional scales (Sauber et al., 2000; Heki, 2001; Wahr et al., 2001; Bevis et al., 2012) and local scales (Bevis et al., 2004; Wahr et al., 2013).

Surface displacements due to environmental loading observed by GPS have also been observed with the Gravity Recovery and Climate Experiment (GRACE) satellite mission derived mass changes. Davis et al. (2004) found a good agreement between the GPS height coordinate time series in the Amazon Basin with predictions of surface displacements derived from the GRACE monthly gravity fields, as the WRMS differences between GRACE and GPS is at level of 1.5 mm. These results are in contrast to the analysis of van Dam et al. (2007) who found only moderate agreement between the GPS and GRACE signals in Europe. The differences were attributed to the signal-to-noise ratio (SNR). In the Amazon Basin, that ratio of water storage to the noise is significantly greater than that over Europe. In addition, van Dam et al. (2007) proposed that the difference between GPS and GRACE can be partly explained by errors in the GPS technique. Subsequent comparisons of GRACE with reprocessed GPS coordinate time series (Tregoning and Watson, 2009; Tesmer et al., 2011; Fritsche et al., 2012) show slightly improved agreement (as compared to van Dam et al. (2007)) but the signals still do not agree at all sites. On the other hand, GRACE estimates of water storage agree with models of water storage at long spatial wavelengths (Swenson and Milly, 2006; Fritsche et al., 2012). The consensus in the community is that some of the disagreement between GPS and GRACE can be attributed to the GPS technique. However, some of the disagreement is also likely due to the inability of GRACE to observe short-wavelength changes in water storage.

Changes in regional water storage from models have also been observed in time series of GPS vertical components. van Dam et al. (2001) compared estimates of vertical surface displacements predicted from a water storage model with GPS vertical coordinates. They found a reasonable agreement, the phase of annual signal in height residuals differs by less than 1.2 month. Recently Fritsche et al. (2012) compared GPS coordinate time series with predicted surface displacements from the Water Global Assessment and Prognosis (WaterGAP) Hydrology Model. They found admittances between the north and east signals of 0.74 ±0.09 and 0.66 ± 0.10 respectively. In the vertical coordinate, the admittance is 0.90 ± 0.06. These comparisons of GPS with GRACE and GPS with water storage models, indicate that GPS is sensitive to CWS variations.

Various authors have used three-dimensional surface displacements from the global GPS network to derive low-degree CWS estimates. The non-uniform site distribution, errors in the GPS products, and sparse distribution of GPS stations in Asia, Africa, South America, and over the oceans limit these inversions. Blewitt et al. (2001) used data from sixty-six globally distributed GPS sites to invert for annual variations in the degree-1 load. They were the first to identify the global annual and semi-annual water mass exchange between the northern and southern hemispheres. Their results were limited by the network of stations as the stations were restricted to continental areas. The higher spatial degrees of the water storage effect aliased into their degree-1 solution.

Wu et al. (2003) used priori statistics about the GPS observation errors to determine the appropriate degree of truncation for the least squares estimation. The problem of the lack of observations over the ocean basins has led others to derive the low degree water storage variations from joint inversions of GPS and GRACE gravity data (Kusche and Schrama, 2005) or GPS with support of ocean bottom pressure models (Jansen et al., 2009; Rietbroek et al., 2012).

Wahr et al. (2013) recently introduced a method to use vertical and horizontal crustal motions from GPS to determine water storage changes in Lake Shasta in northern California. The results suggest that GPS horizontal coordinates are valuable for analyzing regional and local mass changes, especially to unveil the potential source from the possible options.

Recently, vertical GPS time series were used in a regional water storage inversion from a dense GPS network in Washington and Oregon (Argus et al., 2014; Fu et al., 2015). The water storage changes inferred from the vertical GPS time series from dense GPS network have proven to be able to provide quantitative estimates of regional CWS variations.

1.2. Motivation

Up until recently, the only way to detect the water storage was to use in situ observations that were usually only reliable at the basin or sub-basin scale. In-situ observations, such as ground water depth from wells, lake levels, and soil moisture observations, can provide accurate information on the water storage but they are labour intensive and only include point estimates of water storages (Famiglietti et al., 1998; Rosenbaum et al., 2012). Observations of run-off from river gauging stations provide observations of water discharge but they are limited to the scale of catchments or basins. Micro-wave remote sensing satellites are used for measuring the soil moisture, but they only provide information from the top surface (< 5 cm) (Jackson and Le Vine, 1996; Rosenbaum et al., 2012). Groundwater levels are usually monitored using sparsely spaced wells, but the structure of the underground is not sufficient to derive precise groundwater storage.

In the last decade, global observations of the temporal and spatial variability of water storage have become possible with GRACE (Tapley et al., 2004). GRACE currently provides monthly observations of global water storage at wavelengths of about 500

km. GRACE observes gravity field variations by sensing range changes between the twin satellites with K-band microwave interferometer.

Many publications have demonstrated that GPS observations of surface displacement agree with modelled estimates of the displacement at maybe the 50% level. Figure 1.1 shows the GPS up coordinate, GRACE estimates of surface displacement, and the forward modelled estimates of the vertical component. The explanations of the discrepancies between the GPS and modelled displacements can be found in Chapter 5.

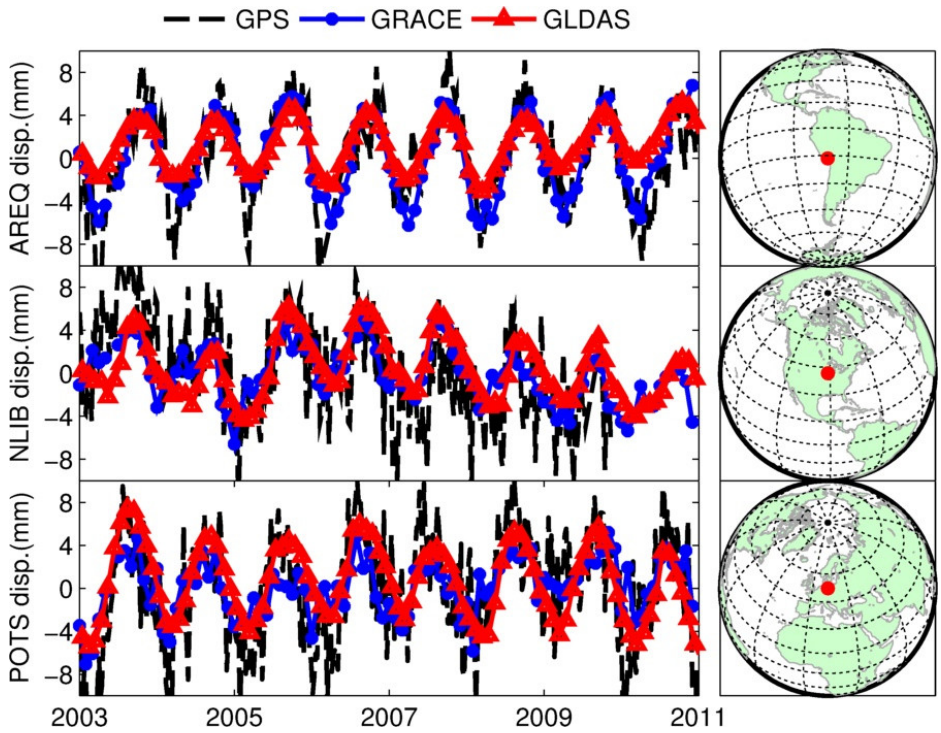

Figure 1.1: GPS weekly vertical observations (black) from IGN overlapped with displacements obtained from GRACE (blue) and GLDAS (red) at three GPS sites : AREQ, NLIB and POTS, showed in red dots on the corresponding maps on the right side, respectively.

Discrepancies between the GPS and modelled displacement require further analysis. One focus of this research is demonstrating that the contribution of signals load displacements induced from the region outside of the study area. Commonly, when authors use GPS time series (after removing all the known effects, such as orbit

error, clock error, ionosphere and atmospheric delay, Tectonics, etc.) to investigate changes in regional water storage, the consider that the load is only driven by CWS changes from the region of interest (Argus et al., 2014; Fu et al., 2015), e.g. Fu et al. (2015) extended the inversion to include one degree of coverage outside the region of interest for the inversion study. However, according to the classical loading theory (Farrell, 1972), mass changes over the whole globe contribute to the surface displacement at any point. In the inversion, this far-field effect (details in Section 4.1) can introduce an error into the inversion. Similar studies show that the loading signals from the far field are small for a constant load or disk load (Schrama, 2005). But in the terrestrial gravitational observations, far-field load signals cannot be ignored (Spratt, 1982; Merriam, 1992). Thus, the far-field effects for the loading displacements will be discussed in section 4.1.

The horizontal GPS coordinates are compared with the GRACE estimates. For the regions where large hydrologic signals occurs (e.g. Amazon River basin) the correlation between GRACE and GPS can reach as high as 0.9 (Tregoning et al., 2009). The horizontal coordinates of the GPS time series have been used to determine the mass changes, inferring lake level and glacial mass loss determination by introducing the ratio between vertical and horizontal coordinates (Wahr et al., 2013). We demonstrate that the horizontal displacements can and should be used in the inversion, more details in Section 3.4.

Vertical displacements are the mostly used in loading displacements studies, both for environmental displacement comparison and for inferring the water storage variations. Recently, the ratio between the horizontals and vertical displacements of GPS observations are used in the continental water storage determination at regional scale (Wahr et al., 2013). Unlike other observation techniques (such as GRACE), GPS observations are relatively sparse except in some regions, e.g. Japan and California. Including as many as available observations from GPS should, in

theory, make the water storage determination more stable, as more redundant observations are included in the inversion. GPS horizontal displacements have proven to be useful for global low degree mass field variation determinations (Wu, 2003; Kusche and Schrama, 2005; Rietbroek, 2014). Thus, a new inversion scheme is required to make use of the horizontal observations for regional continental water storage determination.

1.3. Outline

This thesis is organized according to the motivations presented in the previous section. We first introduce the theoretical basis in Chapter 2, then present the inversion applications in Chapter 3. The pre-studies of the inversion schemes and the corresponding findings are described in Chapter 4 and Chapter 5.

Chapter 2 introduces the mass loading theory for a point load and global mass load as well as the inversion methodologies. We demonstrate the requirements of the loading calculation using mass loading Green's functions as well as its properties for near-field regions. Then, the inversion schemes for determining the continental water storage from the displacements are introduced and described.

Chapter 3 presents three inversion schemes developed in this thesis, and we apply them to different regions demonstrating their applicability. Three-dimensional GPS observations are all used in the inversion schemes and the contributions from the horizontal displacements are shown with the analysis. The results demonstrated that the horizontal coordinates improves the inversion.

Chapter 4 discusses the commonly ignored signals/errors for the regional studies and their impact amplitudes. The results in this chapter are based on simulations and are presented and discussed for all regions over the globe. The goal is to provide a better approach to make use of the GPS observations for regional studies and to determine the amplitude of the error if the far-field or near-field loads are ignored.

Chapter 5 compares GPS time series and forward modelled displacements from GRACE and hydrological models. The discrepancies between GPS and modelled displacements are determined and then discussed. The possible cause of these discrepancies, such as some local effects, thermal expansion of the monument and bedrocks are discussed. In this thesis, the comparisons of all the time series are performed both in the temporal and the spectral domain.

Chapter 2. Inferring surface displacements from changes in surface mass

2.1. Mass loading Green's function

Farrell (1972) derived mass loading Green's functions for a Guttenberg-Bullen (GB) Earth model. For this problem, vertical and horizontal surface displacements U and V, at a particular location are provided as a function of the angular distance between the point and the point load, ψ and its mass m:

$$\begin{aligned} U &= G^u(\psi)m \\ V &= G^v(\psi)m \end{aligned}, \tag{2.1}$$

where $G^u(\psi)$ and $G^v(\psi)$ are vertical and horizontal mass load Green's functions, respectively, shortened here to Green's function.

Green's functions are obtained from the loading Love numbers (Longman, 1963), h and l, and the Legendre polynomials of degree n, P_n, as follows:

$$\begin{aligned} G^u(\psi) &= \frac{a}{m_e}\sum_{n=0}^{\infty} h_n P_n(\cos\psi) \\ G^v(\psi) &= \frac{a}{m_e}\sum_{n=1}^{\infty} l_n \frac{\partial P_n(\cos\psi)}{\partial\psi} \end{aligned}, \tag{2.2}$$

where a denotes the radius of the Earth and m_e represents the total Earth mass.

Loading Love numbers differ from the original Love numbers (Love, 1909) as the former are used to determine the response of the Earth to tidal forcing driven by the moon and sun. In this thesis, only surface mass loading is discussed. Thus, the term mass loading Love numbers will be shortened to Love numbers.

Green's functions are obtained by summing Eq. (2.2) from degree 0 (or 1) to infinity for the vertical and horizontal displacements, respectively. In practice, the Love number used in Eq. (2.2) are calculated using a limited degree, e.g. 10,000. rather than infinity (Farrell, 1972).

Although the Love numbers of high degree are available, the direct summation is not suggested due to the low speed of convergence, as $P_n(1)=1$. Kummer's series transformation (Abramowitz and Stegun, 1964) is applied to enhance the speed of convergence:

$$\begin{aligned} G^u(\psi) &= \frac{ah_\infty}{m_e}\sum_{n=0}^{\infty} P_n(\cos\psi) + \frac{a}{m_e}\sum_{n=0}^{\infty}(h_n - h_\infty)P_n(\cos\psi) \\ G^v(\psi) &= \frac{al_\infty}{m_e}\sum_{n=1}^{\infty}\frac{1}{n}\frac{\partial P_n(\cos\psi)}{\partial\psi} + \frac{a}{m_e}\sum_{n=1}^{\infty}(nl_n - l_\infty)\frac{1}{n}\frac{\partial P_n(\cos\psi)}{\partial\psi}\ , \end{aligned} \tag{2.3}$$

where the h_∞ and l_∞ are constants, following the definition in (Farrell, 1972):

$$\lim_{n\to\infty}\begin{bmatrix} h_n \\ nl_n \end{bmatrix} = \begin{bmatrix} h_\infty \\ l_\infty \end{bmatrix} \tag{2.4}$$

for n sufficiently large. Then the first summation in Eq. (2.3) become constants. The second summation approaches zero since $h_n - h_\infty = 0$ and $nl_n - l_\infty = 0$, respectively, for the n larger than the cut-off degree. Francis and Dehant (1987) further discussed the convergence error for the second terms and provide a routine to compute the Green's function depending on the value of ψ, in order to reduce the error of computing the Green's function.

Green's functions for the displacements are usually normalized by $F(\psi) = 10^{12}a\psi$ (more details in Section 2.2.1) and provided in tabular form (e.g. Farrell, 1972; Francis and Dehant, 1987). Normalized Green's functions for GB and Preliminary Reference Earth Model (PREM) (Dziewonski and Anderson, 1981) are plotted in Figure 2.1. The GB Earth model is conveniently listed in (Alterman et al., 1961) and the corresponding Green's function is obtained in (Longman, 1963; Farrell,

1972; Francis and Dehant, 1987). The Love numbers for the one-dimensional PREM model is presented in (Wahr et al., 1998) and the corresponding Green's function is presented in (Plag and van Dam, 2002). The differences in Love numbers between different Earth models are on the order of 1-1.5 percent (Plag and van Dam, 2002). Discrepancies mainly exist in the near field, i.e. for loads at an angular distance $\psi < 1$ degree (see Figure 2.1). Thus, we conclude that Green's function derived for PREM are more sensitive to the mass change in the near field, but the differences between GB and PREM for $\psi \geq 1$ degree are not significant.

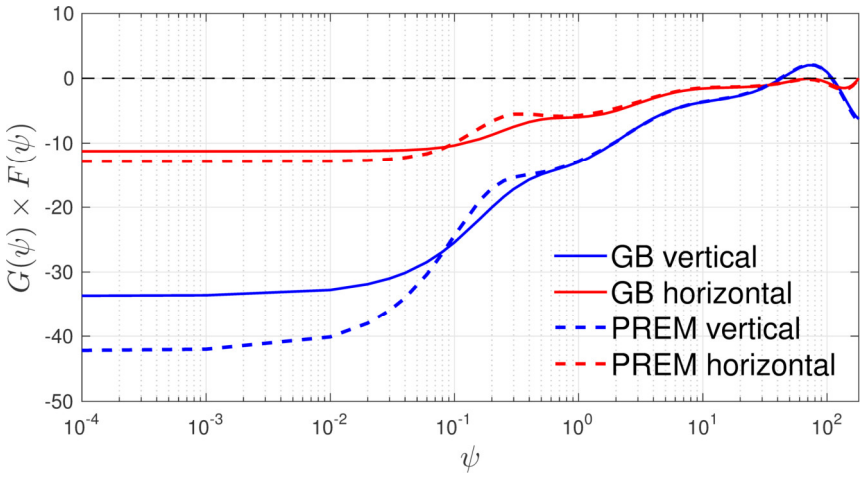

Figure 2.1: Vertical and horizontal normalized Green's function for the GB and PREM Earth models.

2.2. Obtaining displacements from Green's function

Implementing Green's functions from the corresponding Earth model into Eq. (2.1), a point mass located at position P would induce a 3-D displacement in local topocentric coordinate system, N, E and U at position A as showed in Figure 2.2:

$$\begin{bmatrix} N \\ E \\ U \end{bmatrix} = \begin{bmatrix} -G^v(\psi_{AP})\cos(\alpha) \\ -G^v(\psi_{AP})\sin(\alpha) \\ G^u(\psi_{AP}) \end{bmatrix} m \tag{2.5}$$

For a global surface mass load, $P(\psi_{PA},\alpha) \in \Omega$ which is in units of pressure in the hydrological implementations (e.g. van Dam and Wahr, 1987; van Dam et al., 1994), the displacements can be obtained by integrating the effects of all the induced displacements from each infinitely small element within Ω:

$$\begin{bmatrix} N \\ E \\ U \end{bmatrix} = \iint_{\Omega} \begin{bmatrix} -G^v(\psi)\cos\alpha \\ -G^v(\psi)\sin\alpha \\ G^u(\psi) \end{bmatrix} \frac{P(\psi)}{g} \delta A, \tag{2.6}$$

where g denotes the gravitational acceleration and A is the surface area. The spherical coordinate system is defined as in Figure 2.3, the system is simplified as the z-axis can be rotated to the point A (Farrell, 1972). In this polar coordinate system, the point on the sphere can be presented from the angular distance and azimuth, (ψ, α). The surface integration element is

$$\delta A = a^2 \sin\psi d\alpha d\psi \tag{2.7}$$

By introducing spherical coordinate system, the displacements can be determined using the following integrals:

$$\begin{bmatrix} N \\ E \\ U \end{bmatrix} = \frac{a^2}{g} \iint \begin{bmatrix} -G(\psi)P(\psi,\alpha)\sin\psi\cos\alpha \\ -G(\psi)P(\psi,\alpha)\sin\psi\sin\alpha \\ G(\psi)P(\psi,\alpha)\sin\psi \end{bmatrix} d\alpha d\psi. \tag{2.8}$$

Suppose there is a homogenous load over the globe, $P(\psi,\alpha) \equiv P$, and we perform the integral in Eq. (2.8):

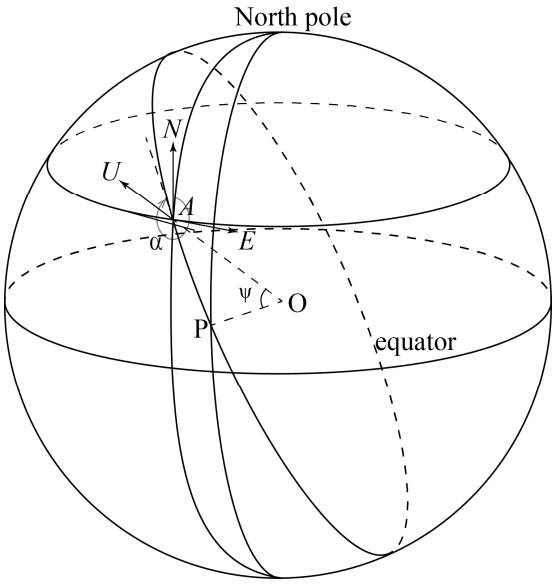

Figure 2.2: 3-D displacement induced by a point load placed at P .

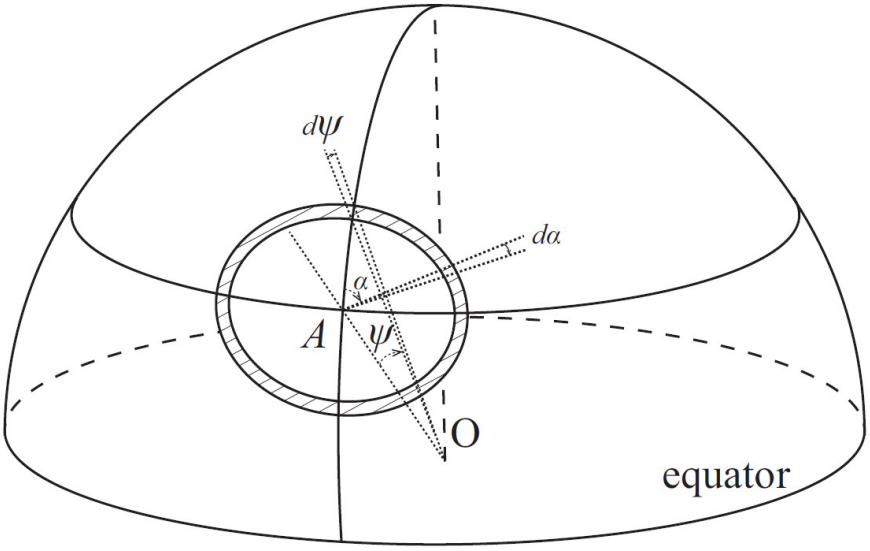

Figure 2.3: Displacements induced at P from mass load in spherical coordinates.

$$\begin{aligned}\begin{bmatrix} N \\ E \\ U \end{bmatrix} &= \frac{a^2 P}{g} \iint \begin{bmatrix} -G(\psi)\sin\psi\cos\alpha \\ -G(\psi)\sin\psi\sin\alpha \\ G(\psi)\sin\psi \end{bmatrix} d\alpha d\psi \\ &= \frac{2\pi a^2 P}{g} \int \begin{bmatrix} 0 \\ 0 \\ G(\psi)\sin\psi \end{bmatrix} d\psi \end{aligned} \tag{2.9}$$

The horizontal displacements are zero due to the fact that the induced displacements cancel each other when two equal masses positioned on each side of the observation position at the same distance, the amplitude of the horizontal displacements are the same but in opposite directions.

Surface mass loading of the Earth is often provided on latitude and longitude grid such as the mass of water in forms of soil moisture, ice/snow depth etc. provided by the Global Land Data Assimilation System (GLDAS) (Rodell et al., 2004), by WaterGAP Global Hydrology Model (WaterGAP, WGHM is also commonly used in other articles) version 2.2 (Döll et al., 2003; Müller Schmied et al., 2014) or atmospheric pressure provided by European Center for Medium Range Weather Forecasts (ECMWF).

The spatial grid datasets have a natural advantage in the regional study as the boundary of the study region is normally clear. Spherical harmonics are a set of the orthogonal functions on sphere, representing the surface of the whole globe. For the regional application, an ultra-high degree of Stokes coefficient is required in order to present regional details. High degree Stokes coefficients also largely increase the size of the parameterization. In the inversion study, increasing the size of the unknown matrix might lead to rank deficient. This draw back the usage of the Stokes coefficient in the regional application.

To calculate the displacement $X = \begin{bmatrix} N & E & U \end{bmatrix}^T$ from a latitude-longitude grid within a region Ω, we insert spherical surface element:

$$dA = a^2 \sin\theta d\theta d\lambda, \tag{2.10}$$

into the Eq. (2.6). The surface displacement induced by the mass variation represented on a latitude and longitude grid:

$$X = a^2 \iint \begin{bmatrix} -G^v(\psi)\cos(\alpha) \\ -G^v(\psi)\sin(\alpha) \\ G^u(\psi) \end{bmatrix} \frac{P(\psi)}{g} \sin\theta d\theta d\lambda, \tag{2.11}$$

The required spatial resolution for obtaining the displacements induced from the surface mass loads will be discussed in Section 2.2.2.

2.2.1 Small angular distance exceptions

Loads at small angular distances from the point of where we want to calculate the loading have three influences on the calculation of Green's function. First, in terms of the Green's function determination, the Green's function does not converge fast enough for the close distance case, i.e. $\psi < 0.01^{\circ}$ (Francis and Dehant, 1987): Due to $P_n(1) = 1$, the $\sum_{n=0}^{\infty} P_n(\cos\psi) = \infty$. Secondly small angular distance also leads to a singularity as the distance term, ψ, is in the denominator. Thirdly, the sharp change of Green's function and the effect for close distance calculation as Green's function is proportional to $1/\psi$. In this section, we focus on the singularity problem of vertical and horizontal displacements when $\psi \to 0$.

Reformulate Green's function for small distance

Green's functions provide the displacement factor between the loading mass and the induced displacements. For calculating the displacements from a very near-field load, a precise modelling of the loading mass is required. Green's function changes quickly at very short distances. So loads here will have a bigger effect than loads at a much greater distance for the equivalent amount of load. To account for this change in Green's functions, and to improve the numerical approximation, we must divide the normal grid unit into much smaller units. Thus, a grid unit close to the

observations is usually smaller than a unit further away (e.g. van Dam et al., 2001). (Further discussion about the spatial resolution requirement is presented in Section 2.2.2). On the other hand, proper modelling of the Green's function itself is required for the close distances as well.

Green's function is normalized by $F(\psi)$, where the vertical and horizontal normalizing factor are both $F(\psi) = 10^{12} a\psi$. Based on the Boussinesq solution (Boussinesq, 1885), normalized Green's function $G(\psi) \times F(\psi) \to C$ when $\psi \to 0$ (Francis and Dehant, 1987), the C is a constant. For the near load, the normalized Green's function, $G(\psi) \times F(\psi)$, can be fitted using third order polynomials, $G(\psi) \times F(\psi) = a + b\psi + c\psi^2$. Higher order polynomials were tested but not found to be significant for the regression. The vertical and horizontal Green's function within 1°, corresponding to ~100 km, can be rewritten as:

$$\begin{aligned} G^u(\psi) \times F(\psi) &= -42.217 + 215.403\psi - 180.279\psi^2 - 189.064\psi^3 \\ G^v(\psi) \times F(\psi) &= -12.850 - 1.004\psi + 434.676\psi^2 - 1410.183\psi^3. \end{aligned} \quad (2.12)$$

These polynomials can be used to obtain Green's function for $\psi < 0.0001^\circ$ as well as for the easier integration of the local effect with less calculation effort.

Re-normalizing Green's function (Agnew, 2012) provides another solution for the close distance exception, In this case, the normalization factor $F(\psi)$ used in (Farrell, 1972) is replaced by

$$F'(\psi) = 2a^2 \sin\left(\frac{\psi}{2}\right) \quad (2.13)$$

for both vertical and horizontal displacements. As the displacements induced from the surface element are calculated as

$$a^2 \int_{\psi - d\psi/2}^{\psi + d\psi/2} G(x) \sin x dx \quad (2.14)$$

Then insert Eq. (2.13) into above, the displacement integral is

$$a^2\int_{\psi-d\psi/2}^{\psi+d\psi/2} G(x)\sin x dx = \int_{\psi-d\psi/2}^{\psi+d\psi/2} \bar{G}'(x)\cos\frac{x}{2}dx$$
$$= 4\bar{G}'(\psi)\cos\frac{d\psi}{2}\sin\frac{\psi}{4} \tag{2.15}$$

where $\bar{G}'$ denotes the renormalized Green's function.

Singularity in Green's function for small distance

When the distance between the mass load and the point where we want to know the surface displacement due to the load approaches zero, then the Green's function goes to infinity due to the singularity.

In a spherical coordinate system, the loading mass dm which is usually expressed in units of pressure (i.e. mbar). We can convert mass to pressure using

$$dm = Pg^{-1}\times 2\pi a^2\sin\psi d\psi, \tag{2.16}$$

where the P is the pressure, g denotes the gravitational acceleration and the factor $a^2\sin\psi d\psi$ represents the surface area of the ring with radius of ψ and width of $d\psi$.

For small ψ , the pressure changes can be treated as constant. Then the horizontal displacements are zero, according Eq. (2.9). The vertical displacement u can be re-formulated as:

$$\begin{aligned} u &= \int_0^{\psi_0} G^u dm \\ &= \frac{P}{g}\int_0^{\psi_0}\frac{\bar{G}^u}{a\psi 10^{12}}2\pi a^2\sin\psi d\psi \\ &\approx \frac{2\pi aP}{g10^{12}}\int_0^{\psi_0}\bar{G}^u d\psi \end{aligned} \tag{2.17}$$

where the $\bar{G}$ is normalized Green's function, $\bar{G} = G(\psi)\times F(\psi)$.

2.2.2 Unit size requirements along the distance

It is reasonable to divide a region into small segments or integration elements, which

can be smaller grid units for the displacement calculation. We consider the integration element as point mass located in the middle of the grid unit. Here we plot the vertical and horizontal Green's function within 5 degrees of distance in black in Figure 2.4.

In Figure 2.4, we show two sets of examples for discretization. The blue line uses the $1^\circ \times 1^\circ$ latitude and longitude size of integration element and the red line indicates the $0.1^\circ \times 0.1^\circ$ size. The difference between the stair-step graphs and the black vertical Green's function line are discretization error, $\varepsilon(G_d\psi)$. By reducing the size of the integration element, $\varepsilon(G_d\psi)$ drops accordingly.

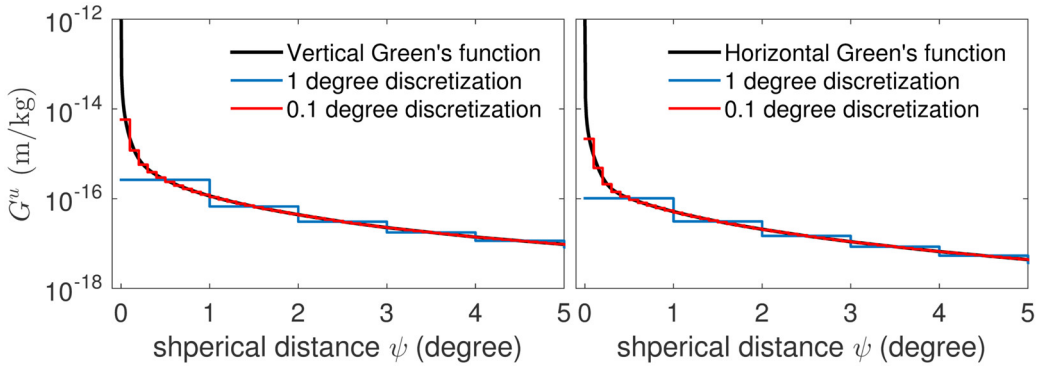

Figure 2.4: Vertical and horizontal normalized Green's function for the close distance in Right and Left Panels, respectively.

The discretization error can be theoretically removed when an infinitely small grid is employed for the calculation. But it is not worth the trouble due to limited computation power. Thus, the question arises how to avoid wasting too much computational power and provide accurate loading displacements? Due to the fact that Green's function is proportional to $1/\psi$, the curve is steep for ψ close to zero and flattens over larger ψ. The common solution is to introduce step functions (adaptive sampling) according to ψ. The sampling rate $d\psi$ is smaller when ψ is small, larger $d\psi$ for larger ψ (see example in Figure 2.4). In this way, the calculation efficiency and accuracy can be balanced.

In principle, the boundaries of the region can be picked randomly. Here we divide the globe into three regions: $\Omega_{\psi\le 0.5^\circ}$, $\Omega_{0.5^\circ<\psi\le 5^\circ}$ and $\Omega_{\psi>5^\circ}$. In order to estimate the discretization error, a closed-loop simulation is performed based on the monthly gravity field from GRACE CSR Rel05[1] from Jan. 2003 to April 2013. This dataset includes 124 months of observations excluding six months without datasets.

The time variable gravity field in terms of the spherical harmonic $(\bar{C}_{lm}, \bar{S}_{lm})$ is synthesized to the mass variation on the Earth surface in terms of the water equivalent height $\Delta m(\theta,\lambda)$ at the spatial resolutions from $(d\theta, d\lambda) = 0.001^\circ$ to $(d\theta, d\lambda) = 10^\circ$. Then it is divided into $\Omega_{\psi\le 0.5^\circ}$, $\Omega_{0.5^\circ<\psi\le 5^\circ}$ and $\Omega_{\psi>5^\circ}$. The surface displacements induced from these three regions are calculated for the corresponding spatial resolutions. The deviation with respect to a case where the entire globe is divided down to the highest resolution are considered as the error from the discretization (see Figure 2.5).

From the simulation (the results are shown in Figure 2.5) the $\Omega_{\psi\le 0.5^\circ}$ have a strong fluctuation for $0.007^\circ \le \psi \le 0.2^\circ$, the standard deviation reaches almost 0.2 mm for $(d\theta, d\lambda) = 0.11^\circ$. For the $(d\theta, d\lambda) = 0.01^\circ$, the standard deviation of the residuals, $\varepsilon^U(\Omega)_{d\theta,d\lambda=0.01^\circ}$ is smaller than 0.05 mm for vertical component and $\varepsilon^{NE}(\Omega)_{d\theta,d\lambda} < 0.003$ mm which is about two orders of magnitude lower than the GPS observation error as the error budget of GPS coordinate is on the order of 0.7, 0.7 and 2.2 mm for weekly north, east and up samples, respectively (Ray et al., 2011). Thus, the spatial resolutions of the mass load are chosen as 0.01°, 0.1° and 1° for $\Omega_{\psi\le 0.5^\circ}$, $\Omega_{0.5^\circ<\psi\le 5^\circ}$ and $\Omega_{\psi>5^\circ}$, respectively.

[1] A standard approach of preparing GRACE gravity field is applied. The degree-1coefficients are replaced by coefficient from Swenson et al (2008), C20 from SLR observations (Cheng and Tapley, 2005) and de-striping filter from Swenson and Wahr (2006) is applied. No Gaussian smoothing filter is applied here to preserving the local signal.

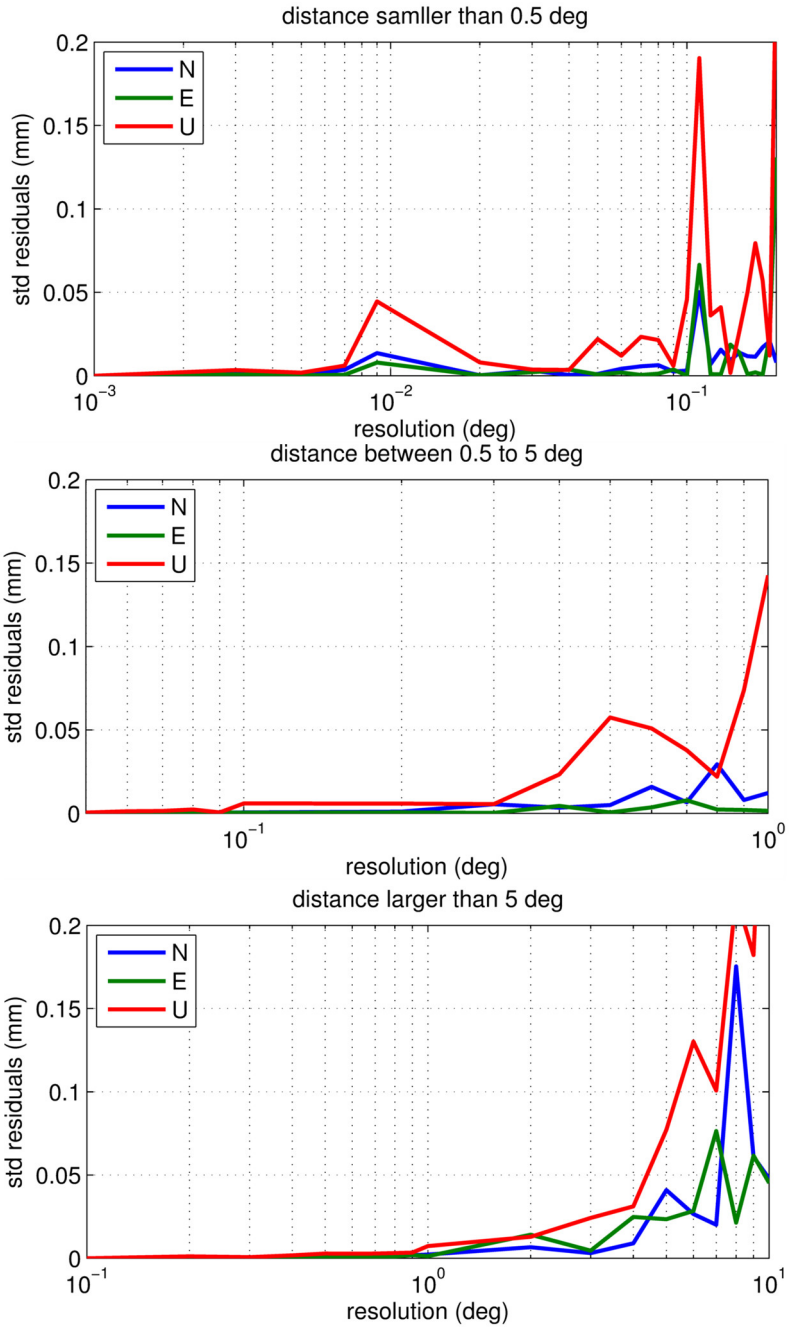

Figure 2.5: Discretization errors of the global displacement which divided into three regions. Top left: standard deviation of the $\varepsilon(G_d\psi)$ *for* $\Omega_{\psi\leq 0.5^\circ}$ *different spatial resolution, the blue, green and red lines for North, East and Up direction, respectively. Top right and bottom: represent the* $\varepsilon(G_d\psi)$ *for* $\Omega_{0.5^\circ<\psi\leq 5^\circ}$ *and* $\Omega_{\psi>5^\circ}$, *respectively.*

In order to show the effects of the different discretization methods, we calculate the displacements at GPS station BUCU $(26.13^\circ\text{E}, 44.46^\circ\text{N})$, using an adaptive grid (Table 2.1). The displacements at the BUCU GPS station, located in the east of the

Danube basin, are obtained from different spatial resolution grids. The single month global water storage load comes from GLDAS. August 2003 is chosen, as in summer time, the load is at a minimum and causes the larges uplift. From this calculation, we see that the displacements are effected by the discretization method. By improving the spatial resolution of the grid, from 1 degree to 0.1 degree, the east and up displacements approach the result from the adaptive grid. For the vertical displacements, the displacements calculated in the degree grid are the same as the result derived from the adaptive grid calculation in the third digits, while the horizontal displacement only meets second digits.

Table 2.1: Displacements at BUCU forward modelled from GLDAS CWS for different spatial resolution

Displacements (mm)	North	East	Up
$1^o \times 1^o$	-0.91	0.32	6.13
$0.1^o \times 0.1^o$	-0.85	0.39	6.36
Adaptive grid	-0.89	0.42	6.36

2.2.3 Displacements induced by global mass variations: spherical harmonic approach

The gravitational potential of the Earth, V, satisfies the Laplace equation:

$$\Delta V = 0, \tag{2.18}$$

where Δ is the Laplace operator. The solution of Eq.(2.18) in spherical coordinates leads to the spherical harmonics series (Heiskanen and Moritz, 1967; Moritz, 1980):

$$V(\lambda,\theta,r) = \frac{GM}{a}\sum_{l=0}^{l_{\max}}\left(\frac{a}{r}\right)^{l+1}\sum_{m=0}^{m=l}(C_{lm}\cos m\lambda + S_{lm}\sin m\lambda)\overline{P}_{lm}(\cos\theta)\ , \tag{2.19}$$

with $V(\lambda,\theta,r)$ represents the gravitational potential at the location (λ,θ,r) in polar coordinates: longitude, co-latitude and distance to the geocenter; GM stands for the

gravitational parameter; l and m are the degree and order of the spherical harmonics coefficients, respectively; $\overline{C}_{lm}$ and $\overline{S}_{lm}$ are the normalized Stoke coefficients for the cosine and sine terms.

Recent gravity satellite missions, CHAllenging Minisatellite Payload (CHAMP) and GRACE, provide, time variable gravity fields up to degree 120 (Mayer-Gürr et al., 2014) after subtracting the long-term mean gravity field. The surface density anomaly is often used to present mass changes or mass anomaly in spherical harmonic expansions (Kusche and Schrama, 2005; Sneeuw, 2006):

$$\sigma(\lambda,\theta) = a\rho_w \sum_{l,m} (C_{lm}^{\sigma} \cos m\lambda + S_{lm}^{\sigma} \sin m\lambda)\overline{P}_{lm}(\cos\theta) \tag{2.20}$$

where ρ_w denotes the density of water, is assumed as $\rho_w = 1000$ kg/m^3. Stokes load coefficients C_{lm}^{σ} and S_{lm}^{σ} are fully normalized spherical harmonic coefficients mapping the mass variations on the Earth surface. From Wahr et al. (1998), Stokes load coefficients are obtained from

$$\begin{Bmatrix} C_{lm}^{\sigma} \\ S_{lm}^{\sigma} \end{Bmatrix} = \frac{\rho_e}{3\rho_w} \frac{2l+1}{1+k_n} \begin{Bmatrix} C_{lm} \\ S_{lm} \end{Bmatrix}, \tag{2.21}$$

where ρ_e denotes the average density of the Earth, $\rho_e \approx 5517$ kg/m^3. k_n are the load Love numbers similar as l in Eq. (2.2). Adopting the loading theory from (Farrell, 1972) in combination with Eq. (2.5), and according to (Kusche and Schrama, 2005), the displacements are:

$$\begin{bmatrix} X^N \\ X^E \\ X^U \end{bmatrix} = \begin{bmatrix} -\frac{3a\rho_w}{\rho_e} \sum_{l=1}^{\infty} \frac{l_l}{2l+1} \sum_{m=0}^{l} (C_{lm}^{\sigma} \cos m\lambda + S_{lm}^{\sigma} \sin m\lambda) \frac{\partial}{\partial\theta} \overline{P}_{lm}(\cos\theta) \\ -\frac{3a\rho_w}{\rho_e \sin\theta} \sum_{l=1}^{\infty} \frac{l_l}{2l+1} \sum_{m=0}^{l} m(C_{lm}^{\sigma} \cos m\lambda - S_{lm}^{\sigma} \sin m\lambda) \overline{P}_{lm}(\cos\theta) \\ \frac{3a\rho_w}{\rho_e} \sum_{l=0}^{\infty} \frac{h_l}{2l+1} \sum_{m=0}^{l} (C_{lm}^{\sigma} \cos m\lambda + S_{lm}^{\sigma} \sin m\lambda) \overline{P}_{lm}(\cos\theta) \end{bmatrix} \tag{2.22}$$

2.3. Inverse approach: displacements to loading mass

Expanding the Eq. (2.6) for *m* discrete mass loads and *N* GPS stations, then the following system of linear equations can be formed as follows for the 3-D displacements:

$$y = Ax + \varepsilon \tag{2.23}$$

where the masses of the x discrete mass loads. y denotes the 3-D displacements and A represents Green's functions including the azimuth term. ε denotes the inconsistencies of the observables which are GPS time series in this case, but are not limited to GNSS technology. For the well distributed and redundant observations (the number of the observation is more than the number of the unknowns), classical weighted least-squares (WLS) adjustment can be implemented to solve the linear system by

$$\left\| W(Ax - y) \right\|^2 \to \min \tag{2.24}$$

in which W is the weight matrix, obtained by inverting the variance-covariance matrix of the GPS displacements, as $W = Q_y^{-1}$. $\left\|...\right\|^2$ denotes the sum of weighted residual. The estimated mass load is

$$\hat{x} = (A^T WA)^{-1} A^T Wy. \tag{2.25}$$

The matrix $A^T WA$ is known as the normal matrix N. After applying of the error propagation law, the covariance matrix of the $\hat{x}$ and $\hat{y}$, which are denoted respectively as $Q_{\hat{x}}$ and $Q_{\hat{y}}$, is obtained as:

$$\begin{aligned} Q_{\hat{x}} &= (A^T WA)^{-1} A^T WQ_y WA(A^T WA)^{-1} \\ Q_{\hat{y}} &= P_A Q_y P_A^T \ , \end{aligned} \tag{2.26}$$

where $P_A = A(A^T WA)^{-1} A^T W,$ more properties about this projector can be found in

Teunissen (2000, p. 55).

2.3.1 Rank-deficient and ill-posed problems

In inverting the linear system of equations, if the results can be properly obtained from the Least Squares (LS) or Weighted Least Squares (WLS) methods, then the linear system is called well-posed system. Two basic inverse problems arise when inverting surface from limited observations: the *rank-deficient* and the *ill-posed problems*. 1. *Rank-deficient problem*: For the linear system which can generally formed by $y = Ax + \varepsilon$, the rank-deficient problem arises when the design matrix of the linear system has a rank smaller than the number of the unknowns n, rank$(A) < n.$ This is typically caused if one or more rows and columns of A are linear combinations of some or all remaining rows and columns (Hansen, 1998, p. 9). 2. The *ill-posed problem* is another concern in inversion theory. For many reasons, e.g. the irregular distribution of the data (GPS network in this study) or gaps in the datasets, the linear problems are ill-posed if the eigenvalues of the normal matrix, N, gradually decay to zero, while the condition number is large (Sneeuw, 2000; Hansen, 2010). This is due to the nearly linear combinations in the design matrix. Detailed examples regarding the well-posed, ill-posed and rank-deficient problems can be found in Petrov and Sizikov (2005).

Excluding the well-posed problem, rank-deficient and ill-posed problems both require including condition matrix or regularization, in order to avoid the ambiguity which comes from the infinite or unstable solutions, respectively.

2.3.2 Regularization

For the linear system $y = Ax + \varepsilon,$ regularization is further applied additional constraints on the normal matrix. The different types of additional information that may be introduced into the regularization can be generally classified into two approaches:

mathematic regularization and regularization by prior information.

The singular value decomposition

Singular value decomposition (SVD) is powerful tool for analyzing inversion problems (Hansen, 2010, p. 28). Any matrix, $A \in \mathbb{R}^{m\times n}$ with $m \geq n$, can be reformed as:

$$A=U\sum V^T \tag{2.27}$$

where the diagonal matrix $\Sigma = diag(\sigma_1, \sigma_2, \ldots, \sigma_n)$ and $\sigma_1 \geq \sigma_2 \geq \ldots \geq \sigma_n \geq 0$. The *condition number* which was originally defined as (Cheney and Kincaid, 2012, p. 321)

$$\kappa(A) = \|A\|\left\|A^{-1}\right\|, \tag{2.28}$$

can be reformulated as

$$\kappa(A) = \frac{\sigma_1}{\sigma_n}. \tag{2.29}$$

The *condition number* indicates the sensitivity of the linear system to the level of the noise. If $\kappa(A) = 10^k$, then the solutions of the linear equations are expected to lose at least k -th digit of precision (Cheney and Kincaid, 2012, p. 321).

Tikhonov regularization and L-curve regularization

The most commonly used regularization method is Tikhonov regularization (Hansen, 2010, p. 60), which is named after Andrey Tikhonov for his ground-breaking work (Tikhonov and Arsenin, 1977). Tikhonov regularization introduces a priori information about the noise level to and invert the matrix with the desired smoothness. It is defined by solving the inversion by minimizing:

$$\|W(Ax-y)\|^2 + \lambda\|x\|^2 \rightarrow \min, \tag{2.30}$$

where the regularization parameter, λ, influences the strength of smoothness for the result.

The trade-off between adding too much artificial smoothing and the too little regularization is the perturbation bound which can be determined from the L-curve (details explained in (Hansen, 1998, p. 83, 2010, p. 71)). The L-curve is represented by

$$\left(\log(\|Ax_\lambda - y\|), \log(\|x_\lambda\|)\right). \tag{2.31}$$

where x_λ denotes the solution for the corresponding regularization parameter. Alternatively λ can be determined by the simulation in order to compensate other unmodelled error sources.

In this thesis, the regularization parameter λ is determined from closed-loop simulations in North America and Europe. The flowchart in Figure 2.6 demonstrates the simulation and how the λ is obtained. The GPS sites and the analysis area is illustrated in Figure 3.5 and Figure 3.10 for North America and Europe region, respectively. This simulation is performed in following process:

1. Closed-loop simulation starts from forward modelling the displacements from the GLDAS monthly model between Jan. 1998 and Dec. 2011 at the GPS sites. The forward modelled displacements are interpolated at the monthly GPS time series epochs (monthly averaged from GPS weekly time series) in order to keep the same availability at each GPS site.

2. The simulated GPS error is consist of a combination of white, flicker and random walk noise, the amplitude and more details are presented in Section 5.2.5. The vertical uncertainties are not conserved is that study, thus we enlarged the original vertical uncertainties from GPS time series which base on the comparison between the original GPS time series and forward modelled displacement from the reference resources. Then the error time series are added into the simulated GPS time series.

3. Basin mean CWS variations are inverted with whole series of different λ. We

compare the inverted basin mean CWS with the original monthly basin mean CWS variations from GLDAS. The square sum of the residuals for each basin are plotted in Figure 2.7 for North America and Figure 2.8 for Europe, respectively.

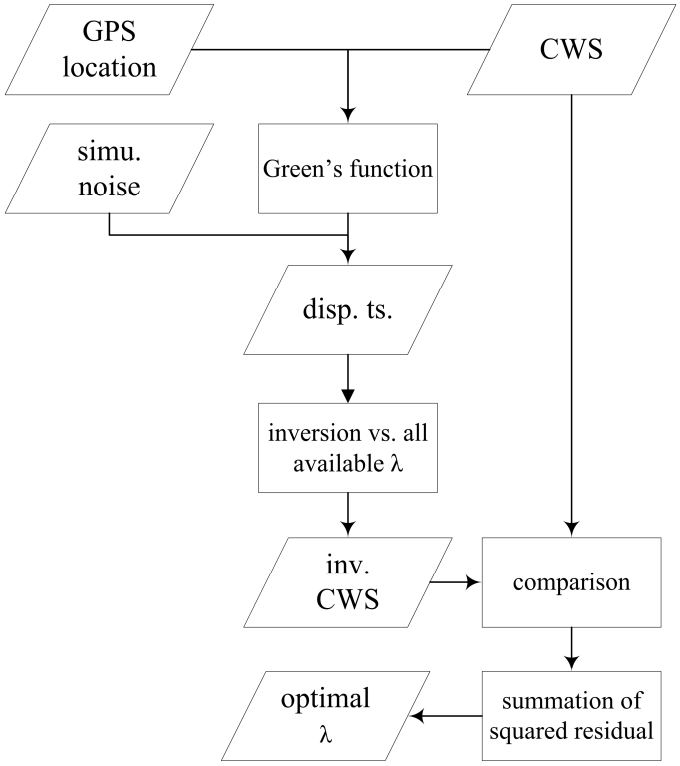

Figure 2.6: Flowchart for obtaining optimal λ from closed-loop simulation.

Firstly, larger regularization parameters generally result in a lower level of the residual, but when regularization parameters continue to increase, the residuals also increase. We choose the cut-off at $\lambda = 0.05$, as most of the basins are close to their minimums and not too much regularization is introduced.

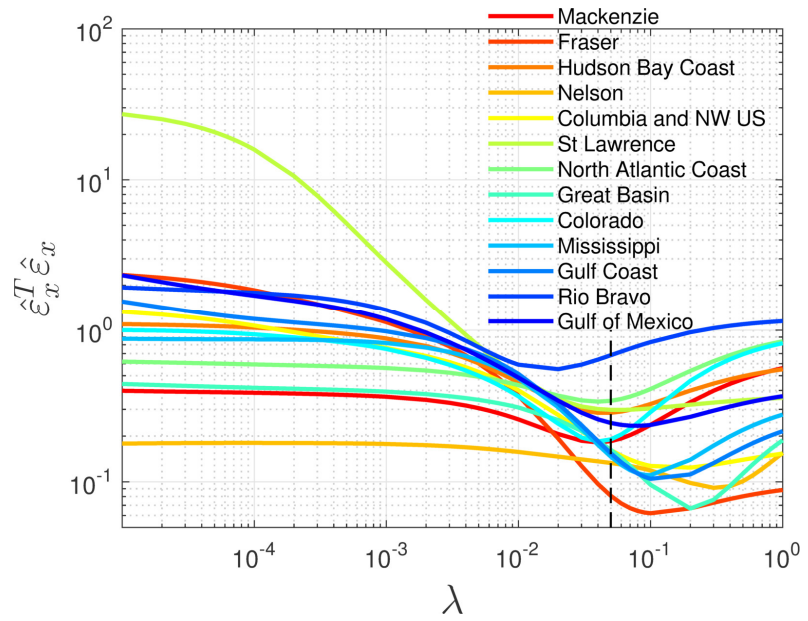

Figure 2.7: Chosen optimized regularization parameter (dash line) in North America inversion region.

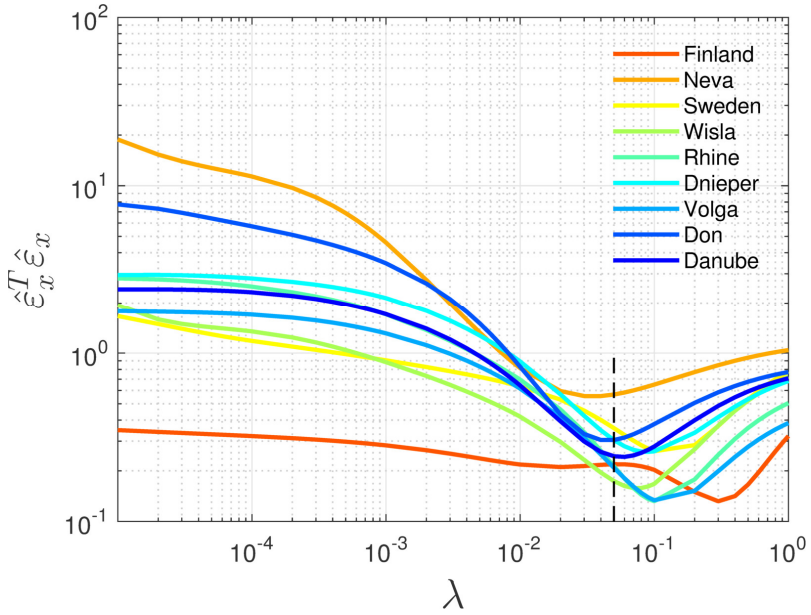

Figure 2.8: Chosen optimized regularization parameter (dash line) in Europe inversion region.

2.3.3 Relative contribution

The observations in a linear system determine the inversion results, but different

observables have different contributions to the least squares solutions. After introducing the unresolved observation into the linear system e.g. $y = Ax + \varepsilon$, then the system can be represented as:

$$\begin{bmatrix} y \\ y_a \end{bmatrix} = \begin{bmatrix} A & A_1 \\ A_2 & A_3 \end{bmatrix} \begin{bmatrix} x \\ x_a \end{bmatrix} + \begin{bmatrix} \varepsilon \\ \varepsilon_a \end{bmatrix} \tag{2.32}$$

where the y_a, x_a and ε_a are the unresolved terms. A_1, A_2, A_3 and the original A forms the combined design matrix A_c. Here after reformulating Eq. (2.32) as the new linear system:

$$y_c = A_c x_c + \varepsilon_c. \tag{2.33}$$

The relative contribution r and r_a, which indicate the share of the original and extra observables from Eq. (2.32), can be obtained from:

$$R = N_c^{-1} N \tag{2.34}$$

$$R_a = N_c^{-1} N_a \tag{2.35}$$

where N_c is the normal matrix for the combined system:

$$N_c = A_c^T W_c A_c \tag{2.36}$$

Contributions of the two sets of the observations for all unknowns are

$$r = \frac{\mathrm{tr}(R)}{m} \tag{2.37}$$

$$r_a = \frac{\mathrm{tr}(R_a)}{m}. \tag{2.38}$$

Chapter 3. Inferring Continental Water Storage from GPS 3-D time series

In this chapter, we focus on regional inversions case studies with GPS observations. The corresponding inversion methodology is described in Chapter 2. There are three inversion methods introduced in this chapter: the single basin inversion, multiple basin joint inversion and regularized inversion. Each method is appropriate for a specific application.

The **single basin inversion** is suitable for spatially extensive basins (e.g. the Amazon River basin) where the displacements within the basin are expected to be much larger than those in the surrounding regions. The **multiple basin joint inversion** is used to determine the CWS at the center of an extensive basin or set of basins within a larger spatial extent. This method can be used if the number of observations and the data quality is sufficient. **Joint inversion with regularization** is a more stable inversion method which can be implemented to infer mass changes in all the major basins within a region using the GPS time series.

3.1. Inversion applications in Amazon River basin

The single basin inversion scheme is the simplest inversion to invoke. In this case, the CWS within one basin is inferred from the displacements observed nearby.

The Amazon River basin is the largest hydrological basin in terms of annual mass variations on the Earth (Lutgens et al., 1995). The water mass loading induced displacements are observed in GPS time series that are highly correlated with GRACE (Blewitt et al., 2001; Davis et al., 2004). But to date, there has been no regional GPS inversion study performed in this region, possibly due to the sparse network around

this region and the short time span of the stations in that region.

The Amazon River Basin, mapped in dark grey in Figure 3.1, is surrounded by five GPS stations indicated by the red dots in the figure. In contrast to the station distribution used in Wahr et al. (2013), the GPS sites around Amazon River basin are relatively distant from the load, e.g. the site BOGT is 1.04^{o} (~100 km) away from Amazon River basin and farthest station, BRAZ is located 4.5^{o} (~450 km) from basin border. Direct inversions of these data without considering the Spatial Truncation Error (STE, discussed in Section 4.1) leads to a CWS amplitude more than twice the GRACE observed CWS change for stations 20 km apart (Wahr et al., 2013). Thus, accounting for the STE is essential for the Amazon case study. The displacements induced by the far field the mass changes, i.e. loads outside of the area where we are inverting for changes in water storage, is obtained from monthly GLDAS CWS variations and the corresponding Green's functions. Then these displacements are subtracted from the GPS observations.

The GPS observations, with outliers removed, from the Amazon River Basin are shown by the black lines in Figure 3.1. The vertical displacements before 2006 were treat as outliers and removed in the BOGT time series as the GPS observations were extremely noisy during those period. The time series of the horizontal displacements from AREQ between 2002 and 2004 and from 2007 to 2008 are removed due to the same reason.

After removing the outliers in the GPS observations, we invert the three-dimensional time series to determine water storage in the Amazon River basin. The inversion is done in processing stages:

1. Choosing the GPS site surrounding Amazon basin, see Figure 3.2, and removal of the linear trends in GPS observations to avoid any tectonics. The

trends are estimated for the entire time span for each site and each directional component. The GPS time series are averaged from weekly to monthly.

2. Atmospheric loading and non-tidal ocean loadings are removed from the GPS time series based on the atmospheric barometric pressure variations provided by National Center for Environmental Prediction (NCEP)/National Center for Atmospheric Research (NCAR) (Kalnay et al., 1996) and the Ocean Bottom Pressure (OBP) product from Circulation and Climate of the Ocean (ECCO) (Fukumori, 2002; Kim et al., 2007), respectively. More details can be found in Section 5.1.3. The Greatbach approach (Greatbatch, 1994) is adopted for removing the trends of the atmospheric and non-tidal ocean loadings in order to be consistent with GPS time series.

3. We re-estimate the GPS uncertainties for CWS loading applications. The horizontal uncertainties are replaced by the standard deviation of the discrepancy between simulated displacements and GPS observations. Error amplitudes of the vertical GPS time series are increased by a factor of five. The reason of introducing this factor is explained in the discussion of the error amplitudes in Section 5.2.5.

4. We estimate the CWS load displacements due to the mass changes outside of the Amazon River basin. These are estimated using the continental water storage derived from GLDAS model. These signals from the GPS observations are removed.

5. The design matrix A in Eq. (2.23) is obtained by convolving the Green's functions $G(\psi)$ for all the integral elements within the Amazon basin. ψ is the spherical distance between the GPS sites and each integral element. The unknown x in Eq. (2.23) is the mean CWS within Amazon basin. Simulated displacements at the GPS sites forms observation matrix y. Then the

CWS variations are inferred from the GPS observations according to Eq. (2.25).

3.1.1 Simulation

Before inverting the GPS observations, we first performed a closed simulation of the inversion. Without introducing any error into the forward modelled GPS time series, the residuals of the closed simulation study are at the level of numerical truncation error (relative error at the level of 10^{-16}). This algorithm is robust in error-free simulation.

We then repeat the simulation including the error information. The displacements that we attribute to the simulated GPS time series are obtained by forward modelling displacements of the mass variations within the Amazon River basin using water storage from the GLDAS model from Jan. 2000 to Dec. 2010. We obtain mass load variations using the soil moisture and snow/ice mass. The CWS in Greenland is excluded from the water storage model due to the unrealistic glacier dynamics there (Jiang et al., 2013). The GLDAS estimates of CWS are provided at a monthly resolution and at 1 degree by 1 degree spatial sampling over the continents. Before using the GLDAS data, Greatbatch correction (1994) is applied, allowing us to remove the trends for each grid cell. Then, we simulate the GPS error as white, flicker, and random walk noise (Williams, 2003). The amplitude of these three error models are based on the re-estimated weekly noise amplitudes in units of mm as described in Section 5.2.5:

$$\begin{aligned}(\sigma_{f=0},\sigma_{f=-1},\sigma_{f=-2})_N &= (0.5,1.5,0.5)\\ (\sigma_{f=0},\sigma_{f=-1},\sigma_{f=-2})_E &= (0.5,1.5,0.5)\\ (\sigma_{f=0},\sigma_{f=-1},\sigma_{f=-2})_U &= (1.5,2.5,1.5)\ .\end{aligned} \tag{3.1}$$

The simulated displacements at the GPS sites in the Amazon River basin are illus-

trated as the blue lines in Figure 3.2. The uncertainties on the simulated displacements are presented as the shaded regions in the figure. These simulated displacements are introduced in the inversion scheme described above and the corresponding CWS time series are presented in Figure 3.4. The statistical differences between the loading displacements signal and the simulated time series are presented in Table 3.1.

Table 3.1: Statistical comparison between simulated GPS and forward modelled displacements

GPS	correlation			WRMSR(%)			RMS signal (mm)			RMS simu. (mm)		
	N	*E*	*U*	*N*	*E*	*U*	*N*	*E*	*U*	*N*	*E*	*U*
UNSA	0.52	0.11	0.18	5.00	0.38	6.75	0.3	0.1	0.8	1.1	1.2	2.6
KOUR	0.39	0.22	0.45	1.62	1.29	5.74	0.4	0.2	0.9	1.1	1.2	2.7
BRAZ	0.31	0.38	0.34	5.14	9.78	6.79	0.2	0.3	0.9	1.1	1.0	2.1
BOGT	0.05	0.33	0.18	2.19	1.89	0.49	0.3	0.2	0.7	1.2	1.2	2.6
AREQ	0.37	0.32	0.33	1.20	3.36	15.95	0.4	0.3	1.5	1.2	1.0	2.7

We can glean a number of results from the table above. Firstly, the loading displacement signal is small, compared to the GPS noise, as the RMS of the simulated time series is two to three times larger than the RMS of the difference of the signal in vertical. The ratio is even worse for the horizontal components. Secondly, a small Weighted Root Mean Square (WRMS) (definition in Section 5.2.1) can be found after subtracting the original loading displacement from the simulated time series. The largest WRMS appears for the AREQ vertical signal as this station is located closest to the center of the basin. WRMS Reduction (WRMSR, definition in Section 5.2.1) for all the other time series are smaller than 10%. Thirdly, relatively small correlations between the simulated time series and the loading displacements are found. All these features are due to the strong noise introduced into the simulation. Thus, if we could inversion CWS from the simulated time series and be able to present better

statistical result than Table 3.1, then it can be defined as a successful inversion algorithm.

Figure 3.1: Amazon basin map (dark grey) with surrounding five GPS stations (red dots).

The inverted CWS from the simulation generally follows the original GLDAS CWS. The WRMS of the obtained CWS after subtracting GLDAS reduces to 8.4 cm of Equivalent Water Height (EWH) from 11.5 cm EWH, thus the WRMSR is 26.7%, see Table 3.2. In the ideal case, WRMSR reaches 100% when this simulation is error free. The simulated errors in the GPS time series are the reason for decreasing WRMSR. In this simulation, the inverted CWS is aligned with the original GLDAS CWS. We calculated the cross correlation and we find no phase delay between the inverted CWS and original CWS. The correlation between the inverted CWS and the original signal are up to 0.69. Comparing to Table 3.1, significant improvements are found. The correlation is almost doubled and the WRMSR are significantly higher than the best WRMS between the simulated GPS time series (based on GLDAS) and loading displacements.

The results from the simulated displacements, thus, provide the qualitative evidence that this sparse GPS network around Amazon River basin can be used for determining CWS variations.

Table 3.2: Statistical comparisons between the CWS obtained from simulated GPS and from reference sources.

	Correlation	WRMSR (%)	RMS (cm)
GRACE	0.55	-10.5	14.1
GLDAS	0.69	26.7	7.8
WaterGAP	0.61	18.4	9.7
GPS	-	-	11.9

3.1.2 GPS-inferred results

Using GPS observations in the inversion, we obtain the results in Figure 3.4. The CWS changes in terms of equivalent water height (EWH) from the GPS 3-D coordinates are shown in black, and the CWS from GRACE (blue), GLDAS (red) and WaterGAP (green) over Amazon. WaterGAP is similar to GLDAS except that surface water, canopy water, and ground water, are included in the model. The grey shaded areas indicate the range of uncertainty on the estimated CWS. The inverted CWS matches the CWS obtained from the reference sources. The correlations between the CWS from GPS and from references are all above 0.7 and show positive WRMSR, see Table 3.4.

The comparisons between the CWS from GPS and GRACE show good agreements, with a correlation up to 0.75 and WRMSR of 31.6%, which is significantly better than the results in the simulated case. We also estimated the annual terms in the obtained CWS time series and the residuals between comparisons, in order to determine whether the main signal content is captured in the GPS inversion.

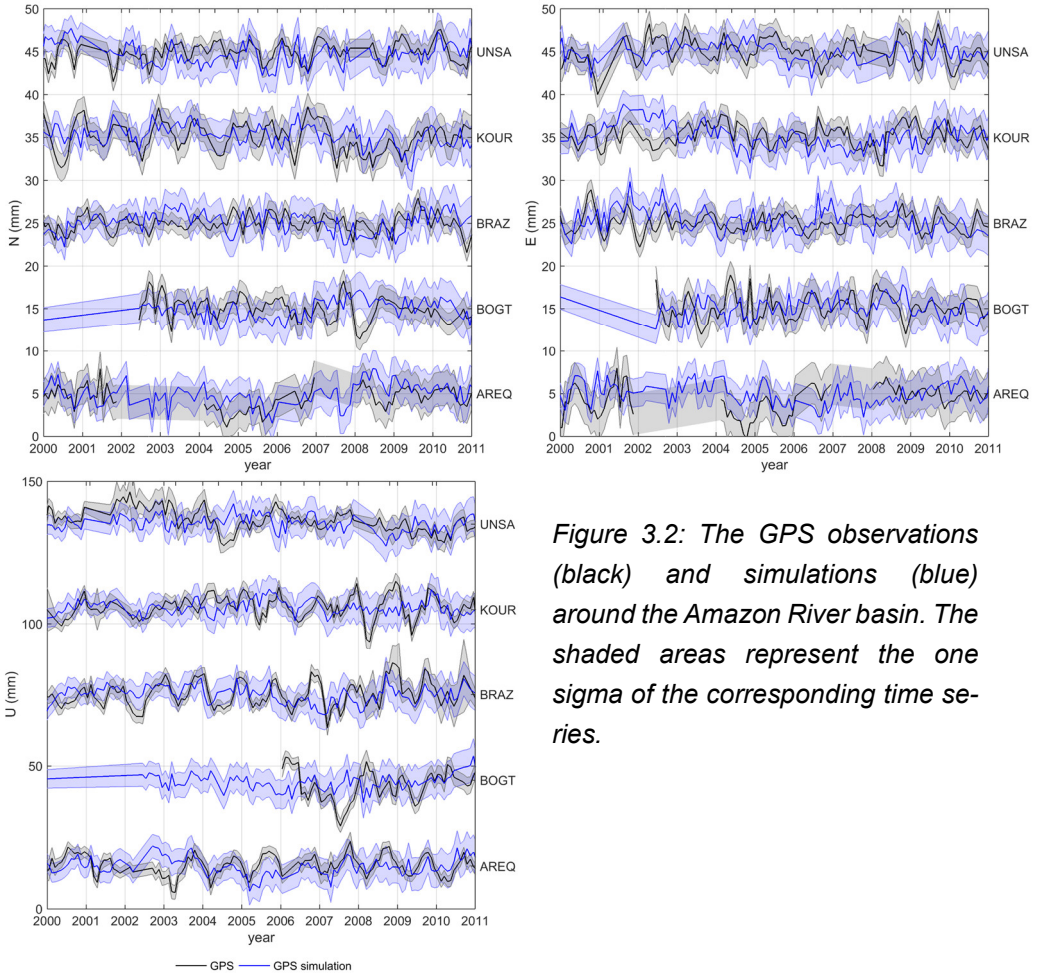

Figure 3.2: The GPS observations (black) and simulations (blue) around the Amazon River basin. The shaded areas represent the one sigma of the corresponding time series.

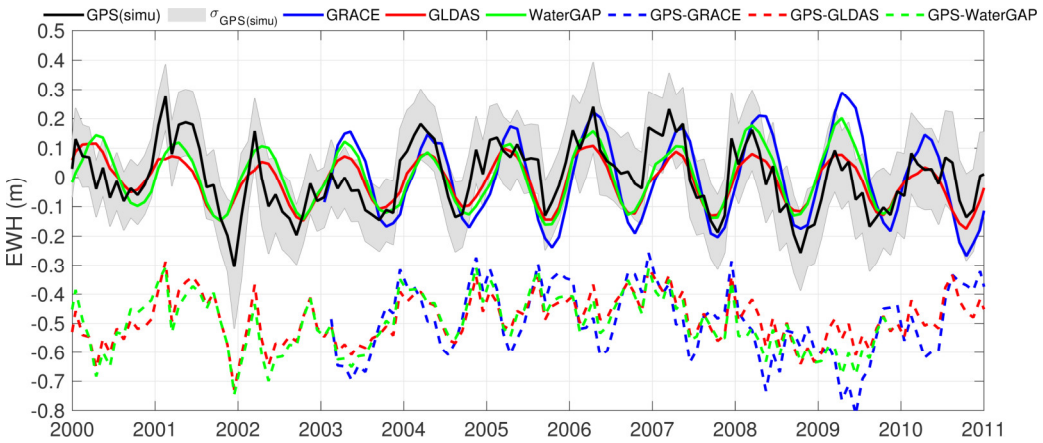

Figure 3.3: Inversion using the simulated GPS time series from GLDAS (black), with CWS obtained from GRACE (blue), GLDAS (red) and WaterGAP (green). The shaded regions represent the one sigma error on the inverted CWS. The differences are shifted with -0.5m EWH for better visualization (dash lines).

Table 3.3: Statistical comparisons between the CWS obtained from GPS time series and from reference sources.

	Correlation	WRMSR (%)	RMS (cm)
GRACE	0.75	31.6	14.1
GLDAS	0.52	14.7	7.8
WaterGAP	0.67	24.9	9.7
GPS	-	-	15.5

The RMS of the modeled CWS from the simulated GPS observations is almost double of the CWS amplitude from hydrological models (GLDAS and WaterGAP) and it shows a similar amplitude to GRACE. This indicates that the hydrological models in Amazon basin under-estimate the water storage. The high correlation between all the CWS time series indicates a proper phase of the inferred CWS.

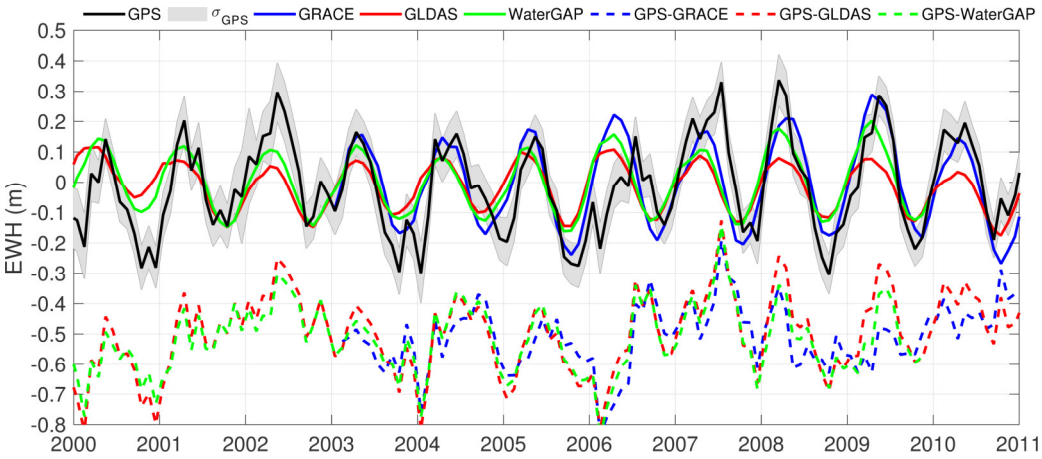

Figure 3.4: CWS obtained from GPS time series (black) in Amazon.

3.2. Inferring CWS in North America

Unlike the sparse GPS distribution around Amazon River basin, a much denser GPS network exists in North America (see Figure 3.5). Recently, the applications of GPS observations in this region were extended to the hydrology field, such as monitoring groundwater (Amos et al., 2014) and estimating water storage (Argus et al., 2014;

Fu et al., 2015).

In this section, we focus on estimating the CWS of the St. Lawrence River basin. Unlike the Amazon River basin where no major basins are located to its east or west direction, the St. Lawrence River basin is surrounded by other river basins in North America. An area outside of the St. Lawrence is co-estimated in the inversion. Inclusion of the surrounding basins helps to reduce the far-field effect error (details in Section 4.1).

3.2.1 Inferring CWS for the St. Lawrence basin

The St. Lawrence River basin (blue in Figure 3.5) includes all the five Great Lakes in North America and makes it the largest fresh water basin in terms of volume in the world. In order to estimate the CWS within this basin, we co-estimate all the basins within a certain distance of this basin. The single basin inversion approach is not suitable for this basin, as St. Lawrence basin is surround by many major basins. The amplitude of the direct inverted CWS is far larger than that obtained from our reference source (GRACE, GLDAS and WaterGAP). This fact arises because of the STE from the surrounding basins. Subtracting displacements from hydrological models cannot reduce STE to an acceptable level. In the next section, we present the inversion method for estimating all the river basins from all the GPS time series with the support of the regularization. In this section regularization is not employed for estimating St. Lawrence River basin CWS from the GPS time series.

Although the suggested geographic coverage for the inversion as discussed in Section 4.1 is 20 degrees from the center of the basin, the coverage applied in this basin extends to 30 degrees as we find that this improves the stability of the inversions and reduces the STE. There are 38 river basins and 138 GPS sites (the corresponding stations and their locations are listed in Appendix A) within this coverage, see

Figure 3.5. But on average, only ~70 GPS have the observation time series simultaneously (see Figure 3.6).

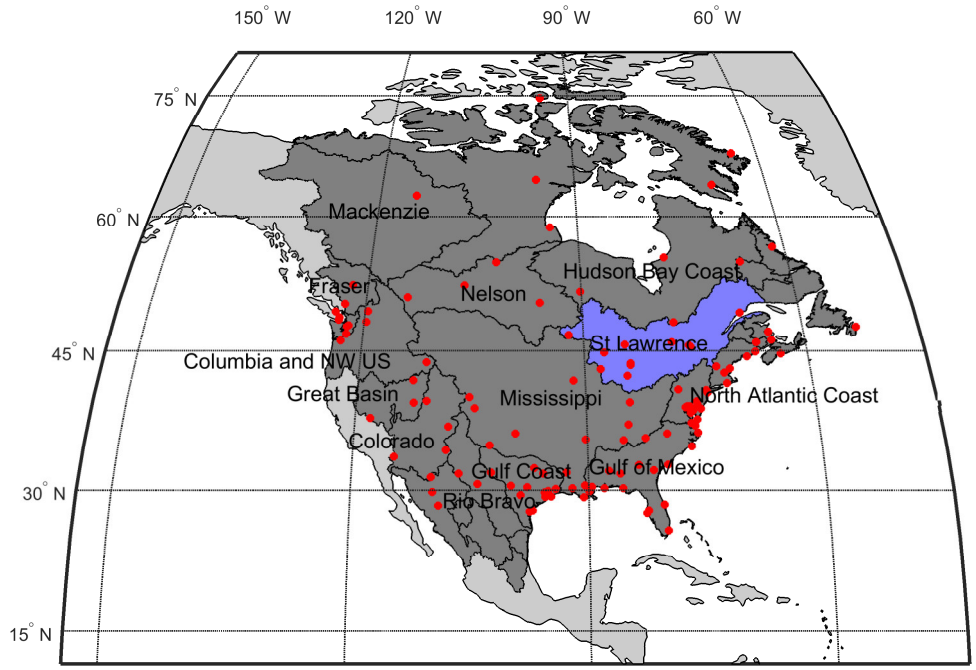

Figure 3.5: The analysis area for North America includes major river basins in dark grey and GPS sites in red dots.

We estimate the CWS in St. Lawrence River basin with Eq. (2.24) without regularization. The uncertainties in the GPS time series are re-estimated as described in Section 5.2.5. The inferred CWS variations are presented in Figure 3.7. They show a better agreement with the CWS from WaterGAP as compared to our other CWS standards. No significant phase delay can be found from the comparisons between GPS and reference sources. The correlation between GPS inferred results and our reference sources reaches up to 0.76 (WaterGAP).

Statistical comparisons of the GPS estimated CWS with our reference sources (GRACE, GLDAS and WaterGAP) are presented in Table 3.4. GPS inferred CWS have the largest RMS as compared to the CWS from our reference sources. RMS of the CWS from WaterGAP is close to our inferred results. The under estimated GRACE monthly solution likely comes from two sources: first, GRACE is not sensing

the small-scale mass changes and second it is effected by the leakage for the regional basin studies. The GLDAS CWS consists of soil moisture (partly groundwater) and snow/ice water. Components such as the remaining groundwater, canopy, and surface water, however, are missing in this model. These missing components of water storage represent the main differences as the peak to peak water level of the Great Lakes can be up to 0.5 m to 1 m, depending on the specific lake. If this surface water is spread out over the whole basin, peak to peak difference is up to 0.1 m. In St. Lawrence basin, surface water is obligate to include in the CWS study. The differences between the GLDAS and WaterGAP in Table 3.4 confirm that soil moisture and snow/ice are not sufficient to represent the seasonal CWS variation amplitude.

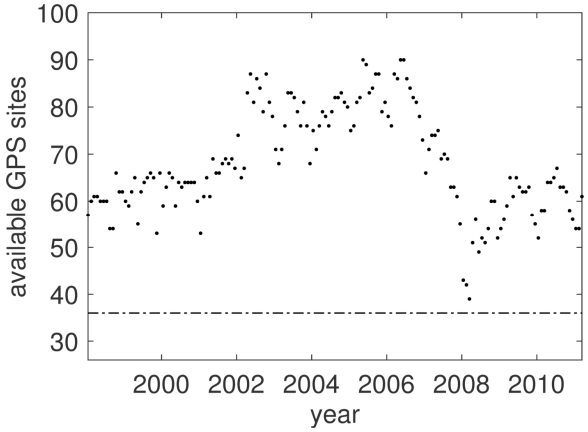

Figure 3.6: Available GPS sites during the entire time span for the inversion. The dash line shows the number of basins which are inferred from GPS time series.

Strong correlations are found in all the comparisons, which would indicate that the phase of the annual signal is properly determined from the inversion. This can also be visually observed in Figure 3.7. Thus, these statistical results proof that CWS can be directly inferred from GPS time series without regularization, in condition of a proper coverage selected.

After 2007, the number of available GPS sites that could be used in the inversion drop from ~90 to ~50, the amplitude of the inferred CWS start to be overestimated

comparing with the CWS from reference sources, especially after May 2008.

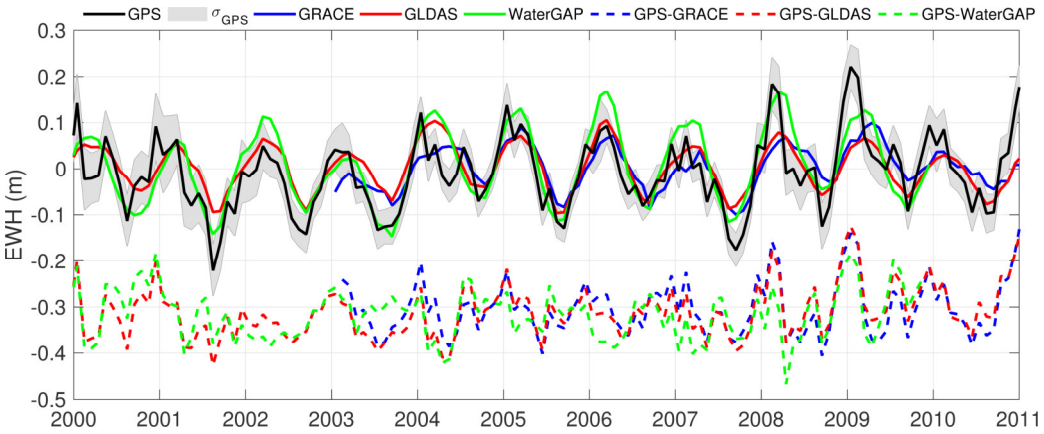

Figure 3.7: CWS obtained from GPS (black), GRACE (blue), GLDAS (red) and WaterGAP (green), differences are shifted with -0.3m EWH.

Table 3.4: Statistical results comparing the CWS from GPS and from reference sources

	Correlation	WRMSR (%)	RMS (cm EWH)	WRMSD (cm EWH)
GRACE	0.72	28.9	4.6	5.6
GLDAS	0.71	28.6	5.0	4.8
WaterGAP	0.76	27.5	8.0	1.9
GPS	-	-	8.0	-

3.2.2 Co-estimating the river basins in North America with regularization

From the simulation of the Amazon River basin in Section 3.1.1, we obtain the signal-to-noise ratio (SNR), the ratio between the power of signal and noise that is below 0.4. The horizontal SNR are worse than the vertical components. The loading signals in North America are lower than they are in Amazon River basin. Thus, the SNR in North America is smaller than in Amazon. Meanwhile, when we present the condition number of the inversion system in North America in Figure 3.8. From the condition number, the normal matrix in North America is not ill-posed, but the condition number

are still too high due to the low SNR value. Thus, regularization is required in the co-estimation of the CWS in North America.

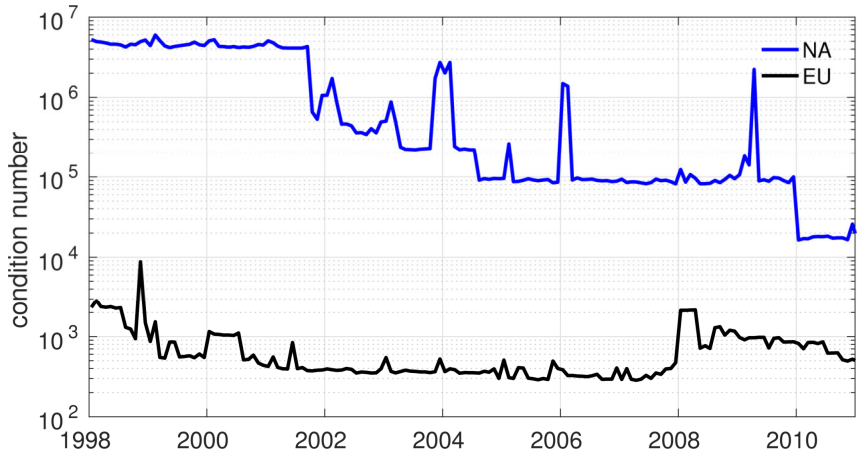

Figure 3.8: Condition numbers of the inversion for both North America and Europe

Co-estimating the CWS change in the river basins using regularization follows the inversion approach described in Section 2.3.2 and adopts the GPS uncertainties re-estimation described in the section above. Based on the simulation using the forward simulated GPS time series in Section 2.3.2, the regularization parameter, $\lambda = 0.05$, is chosen which reduces the remaining error without too much signal attenuation in the solutions.

The coverage of the basins in Figure 3.9, are shown in Figure 3.5. The inversion results for small basins which have less than 15 000 km^2 are not represented in Figure 3.9, as the GRACE solution within the small basins are not suitable for use in the validations.

From Figure 3.9, majorities of inferred CWS time series agree with the reference sources (GRACE, GLDAS, and WaterGAP), except the Mackenzie basin (2002-2005, 2009-2011) and the Nelson basin (2009-2011). Both basins are located at the west border of the analysis area and both lack of GPS stations inside. We suggest not using the inferred CWS from those basins located around boarder due to the

influence of the STE, even after subtracting the forward modelled displacements induced by mass from outside the region.

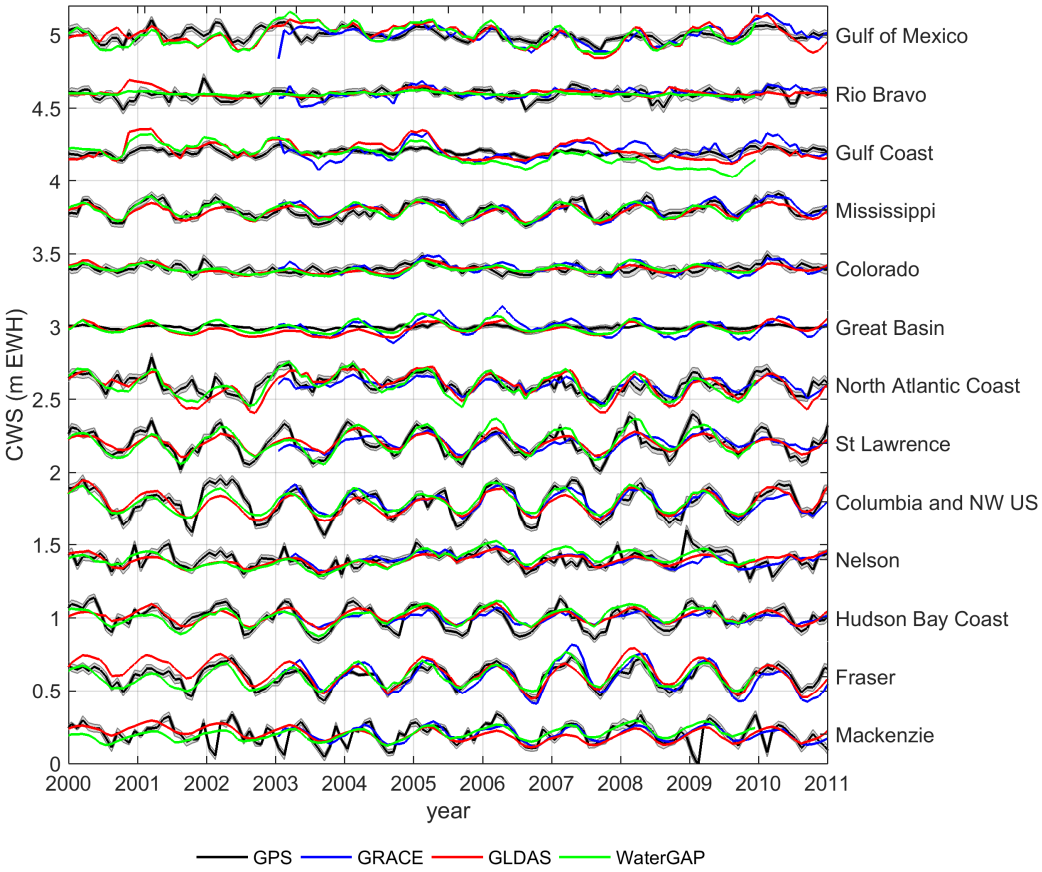

Figure 3.9: Inferred CWS in North America from the GPS 3-D time series. The basin names are on the right side. CWS obtained from GRACE, GLDAS and WaterGAP are plotted in blue, red, and green solid lines, respectively. The shaded areas indicate the uncertainties of the inferred CWS.

After introducing the regularization, the inferred CWS of St. Lawrence River basin become smoother, as compared with the CWS in Figure 3.7. The influence of the GPS error is reduced. The peaks between the 2008 and 2009 are still visible in the inversion results, which is consistent with the inversion without the regularization. This result suggests that the peaks are mass changes not seen by GRACE mission but observed in in the GPS time series, as GPS is more sensitive to the near-field mass changes.

The statistical results of the comparison between CWS inferred from GPS time series and from reference sources are presented in Table 3.5. Inverted CWS of the majority basins (9 out of 13) show relative high correlation, larger than 0.5 to the reference resource. Majority basins (8 out of 13) show positive Weight RMS Reduction (WRMSR). For the big basins in North America, such as the Mississippi Basin, the inferred CWS from GPS time series show a very nice agreement with GRACE, GLDAS, and WaterGAP, the WRMSR is up to 42.5%. These results confirm GPS has the ability to be an independent observation tool for monitoring the water storage variations at the large scale.

Table 3.5: Satistical summary of the results in North America. GR, GL and WG are GRACE, GLDAS and WaterGAP, respectively. The last column WRMS is in unit of cm and presents the WRMS of the CWS inferred from GPS time series

basin	corr.			WRMSR (%)			WRMS (cm)			WRMSD (cm)			WRMS
	NEU	U	NE	NEU	U	NE	NEU	U	NE	NEU	U	NE	GPS
Gulf of Mexico	0.56	0.69	0.71	-23.5	-17.8	-21.0	3.96	4.21	4.15	4.89	4.96	5.02	6.79
Rio Brovo	0.33	0.19	0.34	-31.0	-17.4	7.3	2.83	2.99	2.94	3.70	3.51	2.73	2.35
Gulf Coast	0.48	0.60	0.62	-117.4	-121.9	-179.0	2.30	2.30	2.15	5.00	5.10	6.00	6.05
Mississppi	0.82	0.84	0.80	36.5	42.5	34.2	4.67	4.49	4.17	2.97	2.58	2.75	4.19
Colorado	0.38	0.42	0.29	-31.6	-2.8	-15.7	2.98	2.86	2.73	3.92	2.94	3.16	2.57
Great Basin	0.32	0.32	0.20	-206.6	-110.8	-113.5	1.66	1.64	1.67	5.07	3.46	3.56	3.59
North Atlantic Coast	0.74	0.73	0.78	30.8	-2.7	10.9	5.55	5.66	5.61	3.85	5.81	4.99	8.31
St Lawrence	0.73	0.82	0.84	29.5	39.7	43.7	8.11	8.01	8.16	5.72	4.83	4.60	4.96
Columbia and NW US	0.88	0.82	0.81	52.4	42.2	41.1	8.17	8.28	8.34	3.89	4.78	4.91	7.06
Nelson	0.59	0.58	0.58	17.6	16.6	9.7	5.31	5.15	5.18	4.37	4.29	4.68	3.61
Hudson Bay Coast	0.84	0.82	0.78	31.1	37.4	37.0	7.82	7.60	7.80	5.39	4.76	4.91	4.32
Fraser	0.86	0.82	0.86	32.0	23.6	47.8	7.36	7.18	7.33	5.00	5.48	3.82	8.67
Mackenzie	0.66	0.54	0.54	24.8	15.2	15.9	7.03	6.96	7.01	5.29	5.90	5.89	4.32

3.3. Inferring CWS in Europe

Many permanent GPS stations are located all over Europe. Especially in Western Europe, the dense permanent GPS station network which used in the calculation of the ITRF provide us another opportunity to apply the multi-basin inversion scheme. The Danube river basin is the second largest river basin in Europe, it includes the

territories of 19 countries and is home to 83 million people. We cover the region up to 20 degree of spherical distance to the Danube River basin which includes 59 major river basins and 133 GPS stations (see Figure 3.10 and listed in Appendix B).

3.3.1 Inferring CWS of Danube River basin

We invert the CWS of Danube River basin using all the GPS 3-D displacements within this region without the regularization, i.e. the same approach used in the last section. The results of the Danube River basin are presented in Figure 3.12. The inverted CWS have been compared with the CWS obtained from GRACE, GLDAS and WaterGAP.

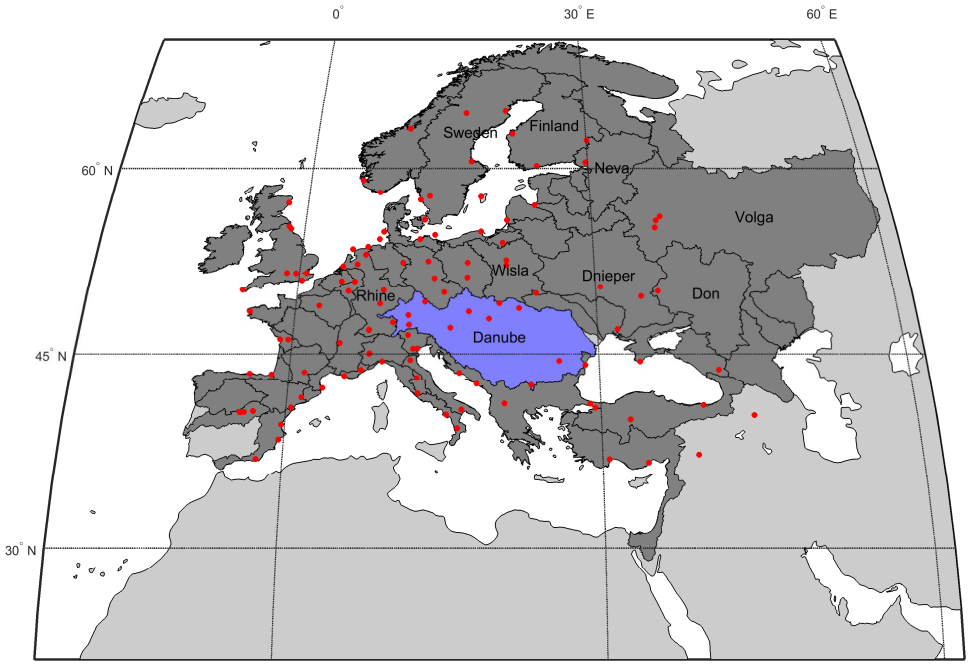

Figure 3.10: Analysis area for the inversion in Europe. 58 river basins (dark grey) and Danube (blue) are included in the inversion (within 20 degrees of distance to the Danube basin). The red dots are the GPS sites.

Although all the dark grey basins in Figure 3.10 are estimated in the inversion, we first discuss the estimated CWS of the Danube River basin itself. We design this approach to minimize the STE for the center basin, see details in Section 4.1. Due to STE effect and the low SNR, the inferred result for the co-estimated basin cannot

be used directly, the time series are dominated by noise. The inferred center basins are appropriate due to the well distributed GPS stations.

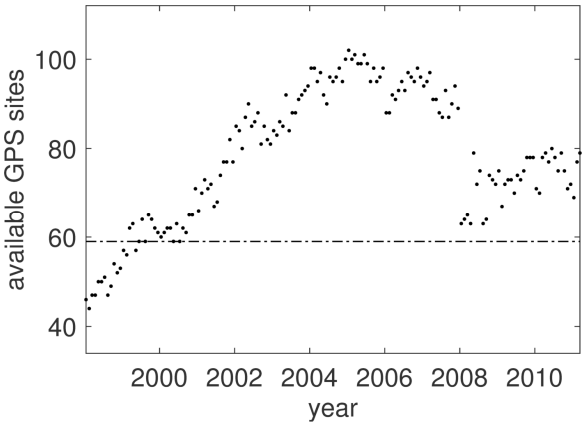

Figure 3.11: Available GPS sites over the time span considered for the inversion. The dashed line shows the number of basins which are referred from GPS time series.

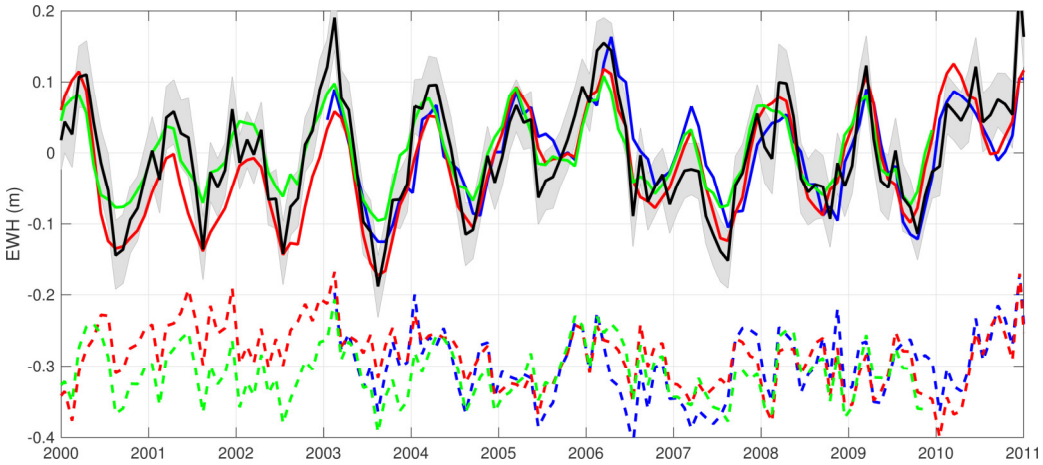

Figure 3.12: CWS of Danube River basin in meters of EWH inferring from GPS time series from GLDAS (black), with CWS obtained from GRACE (blue), GLDAS (red) and WaterGAP (green). The shade range represents the one sigma on the inverted CWS. The differences are shifted with -0.3m EWH for better visualization (dash lines)

Due to the gaps in the GPS time series, the number of available GPS observations for the time period being investigated is presented in Figure 3.11. Before 2002 and after 2008, the number of GPS stations drops dramatically, even below 59 stations before 1999. For the case when the available GPS sites falls below the number of

the basins, direct inversion of the vertical observations would result in rank deficiencies. In the remaining period, the system of equations can be inverted with the GPS 3-D displacements, the inferred CWS is not stable as the number of observations are not sufficient. Even for the optimal period between 2002 and 2008, only about 60-75% of all the GPS stations collect data simultaneously.

Table 3.6: Statistical results comparing the CWS from GPS with that from reference sources in Danube river basin.

	Correlation	WRMSR (%)	RMS (cm EWH)	WRMSD (cm EWH)
GRACE	0.79	38.76	7.55	4.63
GLDAS	0.82	38.11	7.43	4.60
WaterGAP	0.87	46.20	7.53	4.05
GPS	-	-	7.56	-

The inferred CWS of Danube river basin as well as CWS from the reference sources are presented in Figure 3.12. The corresponding statistical results are given in Table 3.6. It shows the inverted CWS from GPS 3-D time series are highly correlated with the CWS from references sources, up to 0.87 for WaterGAP. The CWS from the references sources are found within the one sigma range to the inferred CWS. All the results provide evidence that the inverted CWS variations have a strong agreement with the reference sources, especially with WaterGAP.

3.3.2 Co-estimating the river basins within Europe with regularization

In order to co-estimate the CWS from all the basins in Europe, we invert the GPS time series with the approach described in Section 2.3.2 and applied in Section 3.2.2. The inferred results for basins larger than 150 000 km^2 are plotted in Figure 3.13. The corresponding statistical results are tabulated in Table 3.7.

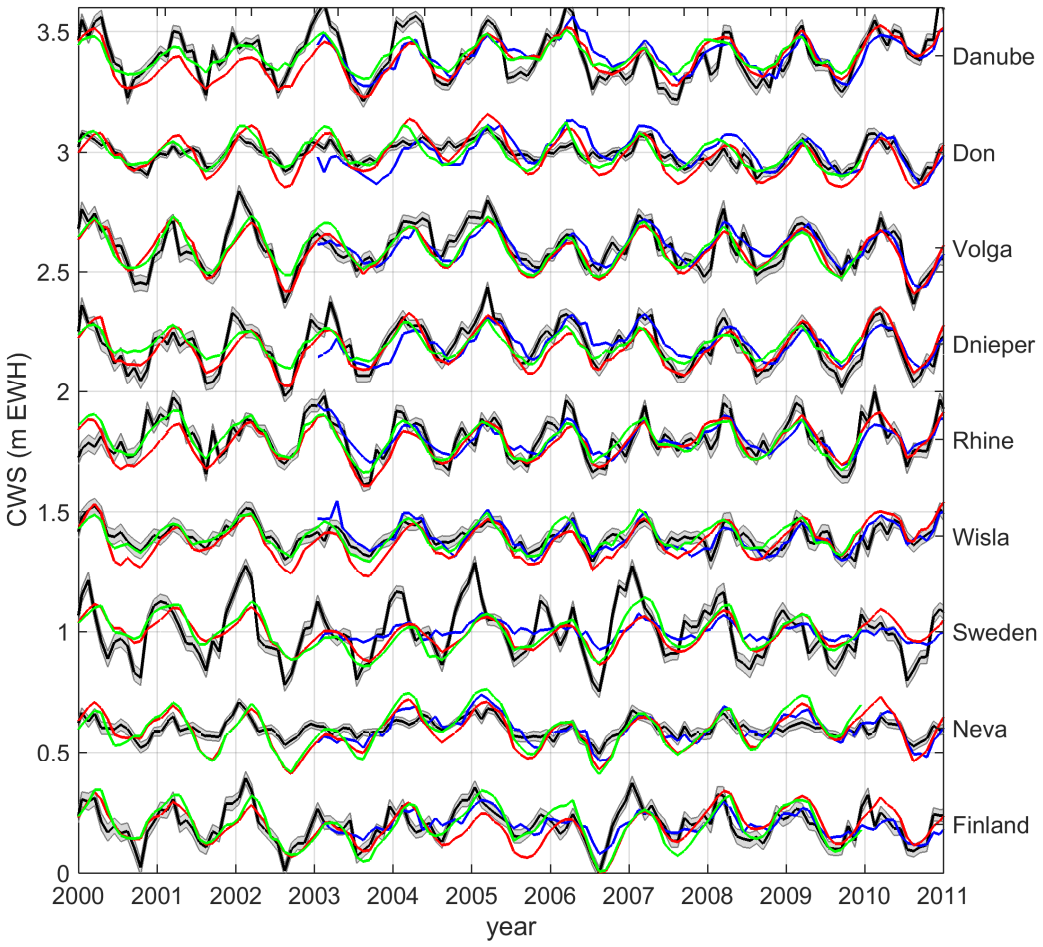

Figure 3.13: Inferred CWS in the Europe from the GPS 3-D time series. The basin names are on the right side. CWS obtained from GRACE, GLDAS and WaterGAP are plotted in blue, red, and green, respectively. The shaded area indicates the uncertainties in the estimated CWS.

The inversion results in Table 3.7 presents better agreement with the reference resources in terms of correlation and WRMSR, than it is in North America. Basins which locate close to the center of the analysis area performs better in terms of correlations with the reference resources, this is similar to what is presented in Section 3.2. This explains why Rhine, Danube, Wisla and Dnieper River basins performs better statistical results.

It is obvious from Figure 3.13 that the inversion for Sweden fails. The inferred CWS is about twice the amplitude from the reference sources. This is expected as this region is close to the northern border (See Table 3.7). In contrast to Sweden, the

Neva river basin CWS is under estimated. For basins not located close to the center of inversion area, a pre-assessment of the inferred results before the inversion is mandatory.

Table 3.7: Statistical results from the inversion over Europe. GR, GL and WG are GRACE, GLDAS and WaterGAP, respectively. The last column WRMS is in unit of cm and presents the WRMS of the CWS inferred from GPS time series

basin	corr.			WRMSR (%)			WRMS (cm)			WRMSD (cm)			WRMS
	GR	GL	WG	GR	GL	WG	GR	GL	WG	GR	GL	WG	GPS
Danube	0.61	0.81	0.73	-10.3	0.9	14.3	4.88	4.76	4.55	5.39	4.72	3.90	7.68
Don	0.80	0.82	0.78	39.5	40.1	35.9	8.26	9.07	8.84	4.99	5.43	5.67	7.83
Volga	0.76	0.84	0.84	34.3	45.4	38.6	8.86	9.11	9.05	5.83	4.98	5.55	7.65
Dnieper	0.80	0.77	0.82	37.5	32.4	42.8	8.55	8.38	8.35	5.35	5.67	4.78	7.05
Rhine	0.77	0.75	0.76	23.0	-1.2	28.6	4.71	4.96	5.06	3.63	5.02	3.61	7.25
Wisla	0.63	0.58	0.62	15.4	18.2	20.8	10.93	11.38	11.57	9.25	9.31	9.16	5.88
Sweden	0.80	0.68	0.68	-0.9	-50.4	-66.4	3.62	3.75	3.74	3.66	5.64	6.22	7.47
Neva	0.69	0.56	0.61	22.6	16.0	19.0	8.29	9.07	9.19	6.41	7.62	7.44	6.04
Finland	0.69	0.63	0.70	28.0	15.3	19.2	6.92	7.40	7.41	4.99	6.27	5.99	7.17

3.4. Contribution of horizontal displacements

Building on the inversion approaches used in previous studies (Argus et al., 2014; Fu et al., 2015), the inversion scheme applied in our study includes the horizontal GPS displacements. Although the horizontal displacements at the GPS sites are only one fifth to one third of the vertical displacements, the GPS observations in the horizontal directions have better precisions than the vertical displacements. In this section, we focus on the contributions of the horizontal observations in the inversion scheme, to address the following question: Do the horizontal displacements contribute to the inferred CWS or does it just bring more errors into the results?

To answer this question, we discuss the horizontal displacements in the multiple inversion scheme. For the single basin inversion case, Wahr et al. (2013) found that the scaled GPS horizontals can be used in the lake level inversion and reasonably agreement with vertical displacements.

3.4.1 Horizontal displacements in Multi-basin inversion scheme

The influences of one set of observations to the inverted result is commonly discussed using the relative contribution, r, as described in Section 2.3.3. We obtain the relative contributions of vertical and horizontal displacements for the Danube River basin from Eq. (2.38). The variance of the horizontal GPS time series is replaced by the re-estimated GPS error variance and for vertical time series, the variance is enlarged by five times, see more details in Section 5.2.5. The weight matrix is inverted from the variance matrix. The co-variance information is not available from the provided GPS time series and excluded in this study. The contributions along the time are plotted in Figure 3.14.

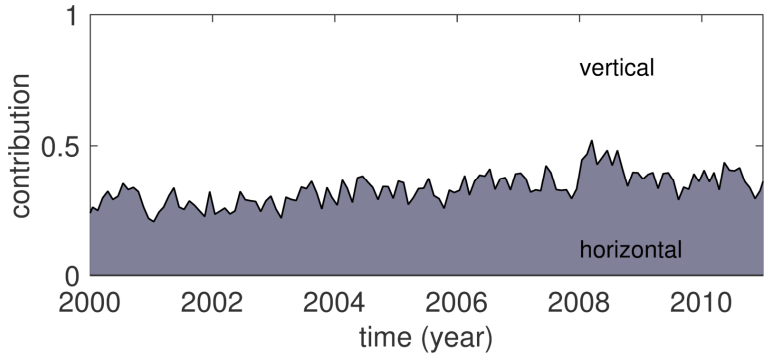

Figure 3.14: Relative contribution of the horizontal displacements to Danube river basin in the Europe inversion scheme.

From Figure 3.14, it is obvious that the horizontal displacements significantly contribute to the inferred CWS of Danube River basin. The mean contribution over the whole period is 0.32. The rest comes from the verticals. But the contributions for the other basins within Europe are location dependent. No pattern is found after comparing with the basin properties such as basin sizes, distances to the Danube River basin and distances to the GPS stations. From the Green's functions in Eq. (2.5), the obtained design matrices in Eq. (2.23) depend both on the GPS distributions and the basin distributions. In this inversion approach, no regularization is introduced. This method is designed to obtain the CWS for the center basin among all the basins

in the analysis area. The inferred CWS of the center basin can be used in the hydrological applications and the inferred results show agreements with GRACE and hydrological models. The CWS of the other basins are excluded, due to the poor quality of the GPS data.

3.4.2 Contribution from horizontal displacements in the inversion scheme: closed-loop simulation

We obtain the relative contribution of horizontal displacements for the Danube River basin in the inversion approach including the regularizations. Regularizations in the inversion approach are designed to reduce the error and make the solution smoother. But when a too strong regularization is applied, the inferred results would be too smooth and are mainly defined by the regularization.

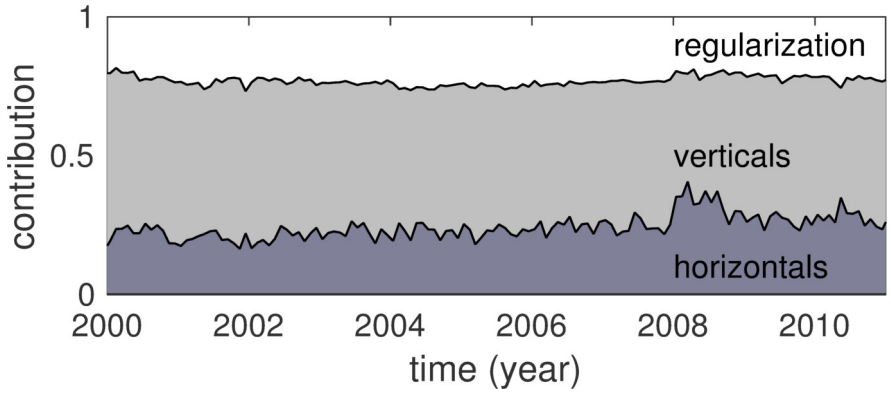

Figure 3.15: Relative contributions of the verticals, horizontal displacements and the regularization for the Danube river basin for our Europe inversion scheme.

From Figure 3.15, the relative contributions of horizontal and vertical displacements, as well as the regularization are presented. The average contributions are 0.24, 0.54 and 0.23 for horizontal displacements, verticals and regularizations, respectively. The summation of the three contributions exceeds one, due to round error. As expected, the inversion approach is dominated by the vertical displacements, due to the stronger response of the load in the vertical direction.

3.4.3 Test the contribution of the horizontal displacement in simulation

From the relative contribution of the horizontal displacements, we can conclude that horizontal displacements significantly contribute to the inversion results. In order to test if extra information is introduced from horizontal displacements, we also perform extra vertical only and horizontal only inversion with the same regularization strength ($\lambda = 0.05$) in a closed-loop simulation. This simulation follows the steps presented in Section 2.3.2, except that we compare the inverted CWS with GLDAS for the selected basins. The inversion results are plotted in Figure 3.17 for Europe and Figure 3.16 for North America, respectively.

Table 3.8: Statistical result of the closed-loop simulation in North America. NEU, U and NE stand for CWS inferred from 3D, vertical only and horizontal only dispalcements. The last column WRMS is in units of cm and presents the WRMS of the CWS obtained from GLDAS

basin	corr.			WRMSR (%)			WRMS (cm)			WRMSD (cm)			WRMS
	NEU	U	NE	NEU	U	NE	NEU	U	NE	NEU	U	NE	GLDAS
Gulf of Mexico	0.91	0.92	0.52	37.1	45.7	-7.6	4.79	5.20	5.56	3.02	2.82	5.98	6.79
Rio Brovo	0.21	0.25	-0.01	-46.1	-34.5	-15.0	1.97	2.15	4.67	2.87	2.89	5.37	2.35
Gulf Coast	0.74	0.71	0.38	-10.3	0.7	-32.1	3.98	4.62	4.75	4.39	4.59	6.28	6.05
Mississppi	0.92	0.90	0.85	57.5	55.6	42.2	5.55	5.52	6.36	2.36	2.45	3.68	4.19
Colorado	0.60	0.59	0.17	19.0	24.5	-12.0	3.00	3.54	4.51	2.43	2.67	5.05	2.57
Great Basin	0.65	0.62	0.36	-64.9	-81.9	-11.0	1.80	1.73	3.54	2.97	3.15	3.93	3.59
North Atlantic Coast	0.87	0.87	0.51	23.1	29.0	-20.1	5.58	5.97	5.77	4.29	4.24	6.93	8.31
St Lawrence	0.95	0.94	0.74	67.9	64.4	30.7	5.77	5.96	7.03	1.85	2.12	4.87	4.96
Columbia and NW US	0.90	0.92	0.54	50.0	57.9	2.3	6.01	6.50	6.34	3.00	2.74	6.19	7.06
Nelson	0.75	0.73	0.40	36.0	33.6	12.5	4.42	4.67	5.65	2.82	3.10	4.95	3.61
Hudson Bay Coast	0.84	0.83	0.68	40.6	34.7	24.3	4.26	4.12	5.87	2.53	2.69	4.44	4.32
Fraser	0.75	0.77	0.50	-116.5	-132.0	-67.8	3.18	2.98	4.46	6.88	6.92	7.49	8.67
Mackenzie	0.74	0.72	0.41	23.2	21.7	-4.2	4.05	4.33	4.46	3.11	3.39	4.65	4.32

It is clear, that the inferred CWS from horizontal only displacements are worse than CWS obtained from 3D or vertical only displacements in terms of accuracy. No significant difference between inverted CWS from 3D displacements and from vertical

only displacements, from both Figure 3.17 and Figure 3.16. The corresponding statistical results are tabulated in Table 3.8 and Table 3.9 for simulations in North America and Europe, respectively. The statistical results present the differences between the simulation input, GLDAS CWS variations and the inferred CWS from the displacements at GPS site.

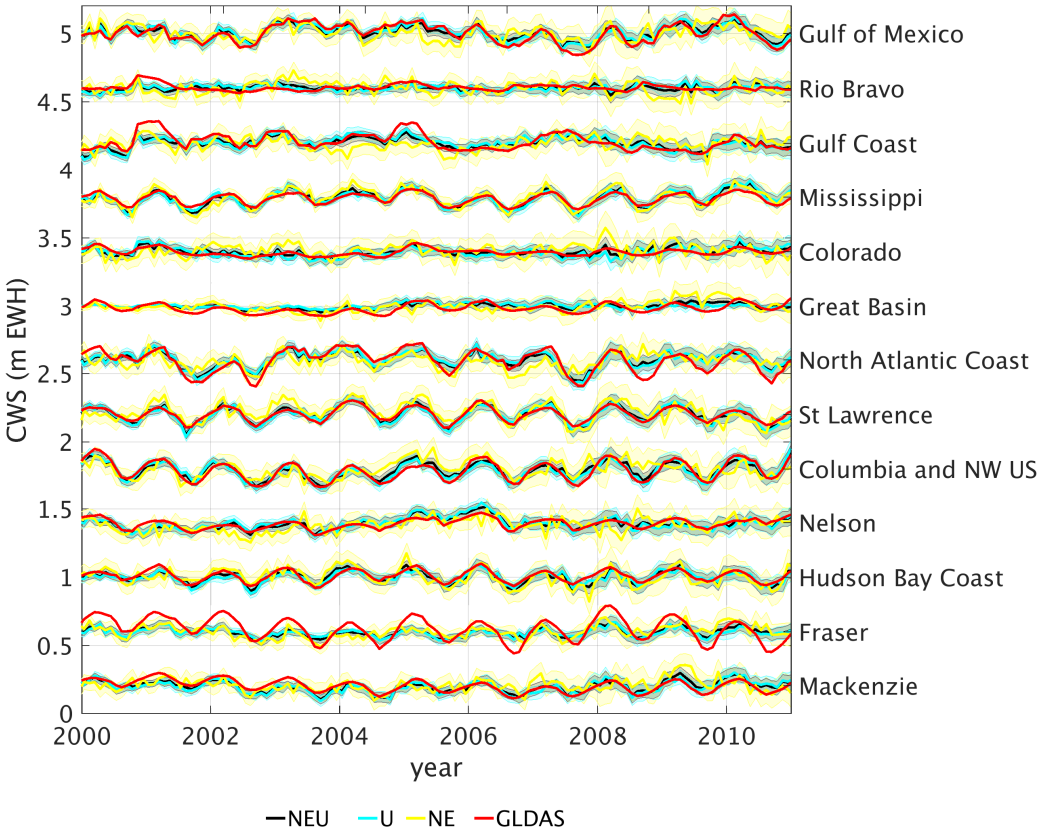

Figure 3.16: Closed-loop simulation for the 3D, vertical only and horizontal only inversion in North America. CWS inferred from simulated 3D, vertical only and horizontal only are in black, cyan and yellow, respectively. The displacements are simulated from GLDAS (red).

Significant improvement after introducing the simulated horizontal displacements are founded comparing with the vertical only inversion results, as eight basins preforms better correlation, seven shows larger WRMSR and ten have lower WRMSD, all out of total 13 basins in North America. Majorities show improvements after introducing horizontal displacements. Similar results are found in Europe, and even more basins

shows improvements, as seven, eight and seven out of nine shows better correlation, WRMSR and WRMSD, respectively.

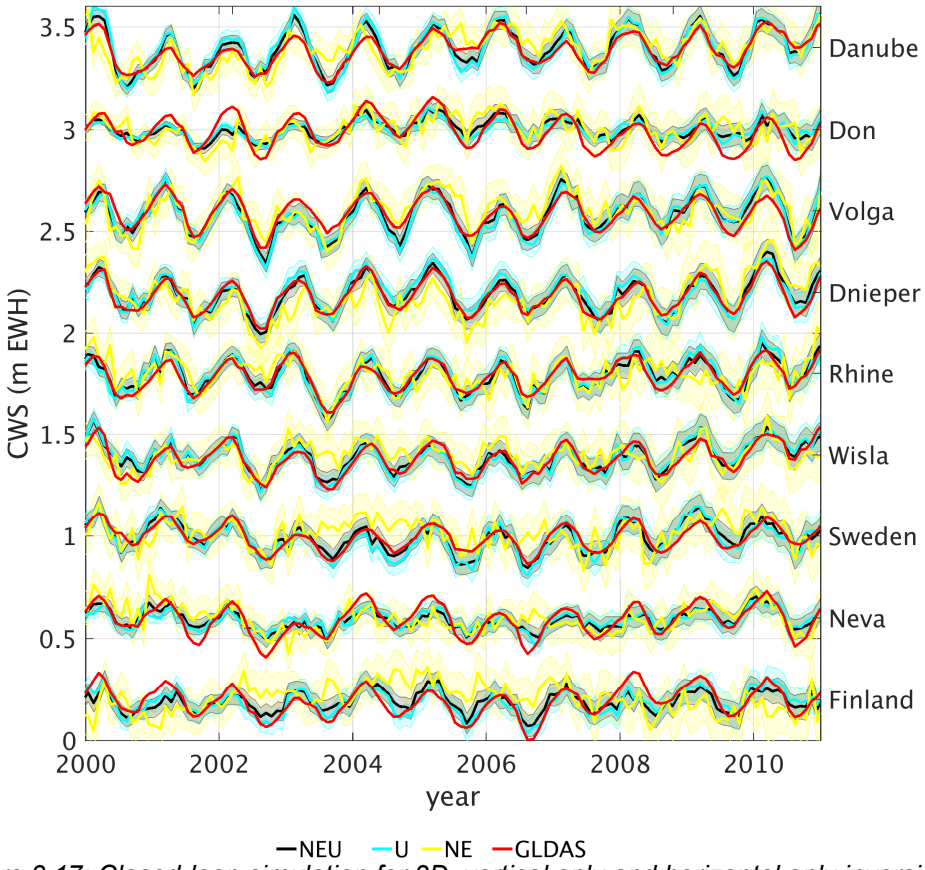

Figure 3.17: Closed-loop simulation for 3D, vertical only and horizontal only inversion in Europe.

Table 3.9: Statistical result for closed-loop simulation in Europe. NEU, U and NE are the CWS inferred from 3D, vertical only and horizontal only dispalcements. The last column WRMS is in unit of cm and presents the WRMS of the CWS obtained from GLDAS.

basin	corr.			WRMSR (%)			WRMS (cm)			WRMSD (cm)			WRMS
	NEU	U	NE	NEU	U	NE	NEU	U	NE	NEU	U	NE	GLDAS
Danube	0.80	0.83	0.47	-6.6	-16.0	-10.3	4.48	4.01	6.57	4.78	4.65	7.25	7.68
Don	0.89	0.87	0.72	55.4	51.0	29.0	9.55	9.90	9.18	4.26	4.85	6.52	7.83
Volga	0.95	0.92	0.72	67.7	59.6	33.1	8.31	8.23	10.63	2.69	3.32	7.11	7.65
Dnieper	0.92	0.92	0.62	60.7	58.4	17.8	7.80	8.21	7.39	3.07	3.41	6.07	7.05
Rhine	0.90	0.87	0.66	51.3	48.0	5.6	7.01	7.46	6.42	3.41	3.88	6.06	7.25
Wisla	0.87	0.86	0.39	51.8	49.9	-4.7	6.96	7.60	7.18	3.35	3.81	7.52	5.88
Sweden	0.86	0.83	0.57	9.1	-3.5	-1.0	4.65	4.38	6.68	4.23	4.53	6.75	7.47
Neva	0.85	0.84	0.45	28.4	21.4	-1.7	4.69	4.60	6.23	3.35	3.62	6.34	6.04
Finland	0.75	0.83	-0.09	6.5	36.2	-47.5	5.07	6.12	7.33	4.74	3.90	10.82	7.17

Due to the low SNR in the horizontal time series, the horizontal only inversion does not perform as well as the vertical only or 3D inversion scheme. But the contribution from the horizontal time series cannot be ignored. From this closed-loop simulation, we conclude that the horizontal displacements are able to bring extra information into the 3D information scheme. In the next section, we test this again from the GPS time series to see if extra information is introduced in the 3D inversion.

3.4.4 Contribution from horizontal displacements in the inversion scheme: GPS time series

We repeat the comparison in the last section with the GPS time series and the results in both regions presented in Figure 3.18 for North America and Figure 3.19 for Europe. The differences between the inferred CWS from 3D, vertical only and horizontal only displacements are larger than simulation presented in the last section. The differences between the 3D and vertical only displacements are relatively small, suggesting that major signals are contributed from vertical time series. The inverted CWS as well as the CWS obtained from reference source plotted in Figure 3.18 and Figure 3.19. The corresponding statistical comparison of the correlation and WRMSR are presented from Table 3.10 to Table 3.13.

Improvements are found for majority of the basin in both North America and Europe, when horizontal time series is employed in the inversion. For total 13 basins, 8, 10 and 10 basins show larger correlation comparing with CWS from GRACE, GLDAS and WaterGAP, respectively. Meanwhile, nine basins show larger WRMSR, when compared with the reference sources. Thus, extra information is introduced into the inversion by the horizontal time series in North America.

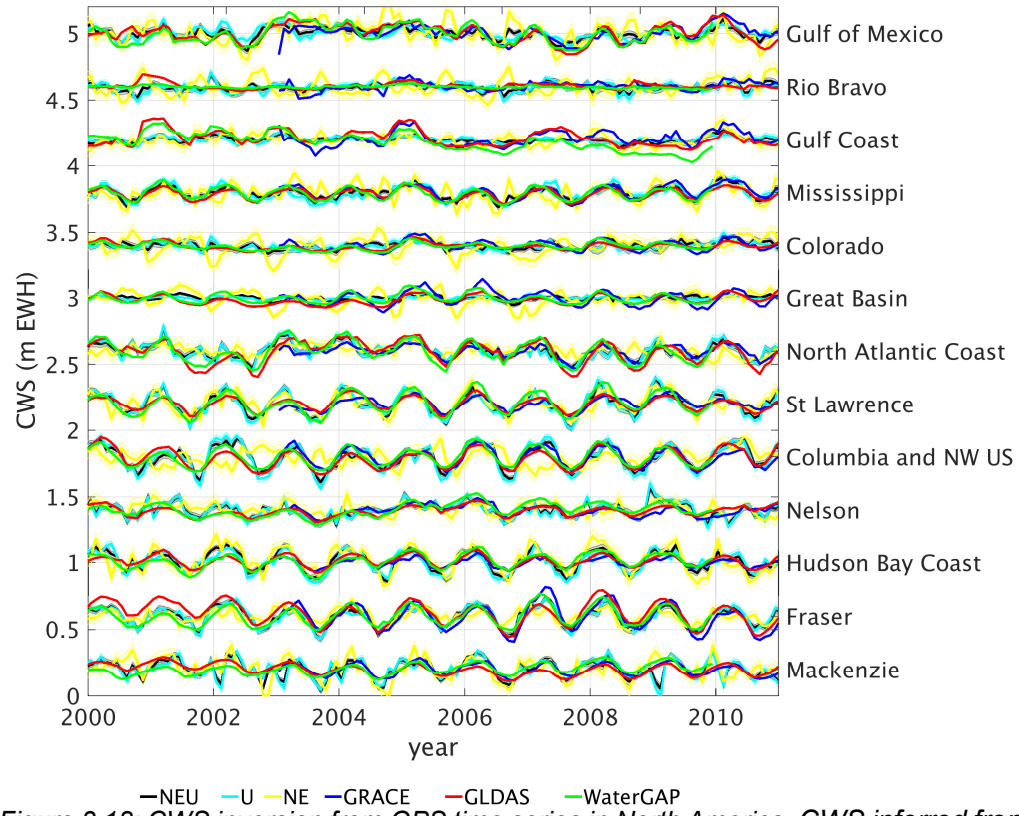

Figure 3.18: CWS inversion from GPS time series in North America. CWS inferred from simulated 3D, vertical only and horizontal only are in black, cyan and yellow, respectively. CWS from GLDAS (red) is used as reference source. Shade area represents the corresponding one sigma standard deviation.

Table 3.10: Correlation between inferred CWS and reference sources in North America

basin	GRACE			GLDAS			WaterGAP		
	NEU	U	NE	NEU	U	NE	NEU	U	NE
Gulf of Mexico	0.56	0.66	0.18	0.69	0.56	0.44	0.71	0.64	0.41
Rio Brovo	0.33	0.26	0.03	0.19	0.10	0.08	0.34	0.27	0.03
Gulf Coast	0.48	0.39	0.39	0.60	0.54	0.37	0.62	0.54	0.35
Mississppi	0.82	0.76	0.46	0.84	0.78	0.44	0.80	0.74	0.37
Colorado	0.38	0.41	0.04	0.42	0.50	-0.06	0.29	0.38	-0.14
Great Basin	0.32	0.61	0.01	0.32	0.63	-0.01	0.20	0.64	-0.14
North Atlantic Coast	0.74	0.72	0.36	0.73	0.71	0.48	0.78	0.77	0.47
St Lawrence	0.73	0.68	0.73	0.82	0.80	0.70	0.84	0.81	0.75
Columbia and NW US	0.88	0.90	0.20	0.82	0.83	0.14	0.81	0.84	-0.02
Nelson	0.59	0.54	0.46	0.58	0.53	0.39	0.58	0.55	0.43
Hudson Bay Coast	0.84	0.80	0.76	0.82	0.80	0.69	0.78	0.75	0.67
Fraser	0.86	0.87	0.60	0.82	0.81	0.58	0.86	0.84	0.65
Mackenzie	0.66	0.58	0.62	0.54	0.44	0.57	0.54	0.46	0.49

The improvements in the inversion in Europe are not as significant as in North America after introducing horizontal time series into the inversion. About half of the basins shows an improvement in the correlation (six for GRACE, three for GLDAS and four for WaterGAP out of nine basins) and WRMSR (five for GRACE, four for both GLDAS and WaterGAP). The reason of the differences can be explained by the condition number, shown in Figure 3.8. The condition number in North America is at the level of 10^3 which is about the same magnitude of the regularization parameter, but the condition number in Europe are mostly above the magnitude of 10^5, except after the year of 2010 when condition number falls to order of 10^4. The higher the condition number, the stronger of the effect of the noise in the linear inversion system, and in our inversion scheme the regularization contributes more.

Table 3.11: WRMSR of the inferred CWS from GPS comparing to CWS from reference sources in North America

basin	GRACE			GLDAS			WaterGAP		
	NEU	U	NE	NEU	U	NE	NEU	U	NE
Gulf of Mexico	-22.04	-17.96	-10.68	-15.75	-38.64	2.96	-18.97	-35.13	-1.53
Rio Brovo	-27.18	-17.90	-14.69	-13.52	-11.89	-4.26	7.84	5.11	-0.43
Gulf Coast	-134.98	-155.47	-28.04	-138.15	-138.03	-37.26	-186.38	-166.07	-64.86
Mississppi	35.49	33.80	6.40	42.50	36.83	7.80	33.68	33.62	1.54
Colorado	-28.62	-28.57	-17.06	0.36	6.71	-9.00	-10.72	-4.86	-11.79
Great Basin	-199.79	-238.00	-37.53	-104.75	-127.80	-16.25	-103.56	-107.24	-22.53
North Atlantic Coast	32.19	30.95	-18.07	-1.44	9.35	-80.00	12.13	22.39	-84.65
St Lawrence	31.36	27.69	32.12	39.89	36.55	29.38	43.26	38.95	29.16
Columbia and NW US	54.36	52.80	-29.15	43.43	42.88	-40.24	42.00	42.28	-50.11
Nelson	19.87	17.37	2.85	18.40	15.92	-4.68	6.76	5.04	-15.69
Hudson Bay Coast	30.40	28.65	23.08	35.95	33.32	25.14	35.11	31.66	25.64
Fraser	32.61	33.51	-50.99	29.75	28.75	-44.31	48.07	44.53	-7.68
Mackenzie	27.84	21.87	23.06	16.58	10.13	18.18	19.45	14.73	14.90

Table 3.12: Correlation between inferred CWS and reference sources in Europe

basin	GRACE			GLDAS			WaterGAP		
	NEU	U	NE	NEU	U	NE	NEU	U	NE
Danube	0.61	0.72	0.23	0.81	0.84	0.39	0.73	0.78	0.30
Don	0.80	0.82	0.28	0.82	0.88	0.26	0.78	0.85	0.16
Volga	0.76	0.72	0.45	0.84	0.81	0.38	0.84	0.81	0.29
Dnieper	0.80	0.75	0.66	0.77	0.73	0.63	0.82	0.79	0.63
Rhine	0.77	0.73	0.39	0.75	0.76	0.40	0.76	0.80	0.29
Wisla	0.63	0.56	0.55	0.58	0.53	0.48	0.62	0.55	0.56
Sweden	0.80	0.77	0.56	0.68	0.78	0.35	0.68	0.77	0.38
Neva	0.69	0.71	0.52	0.56	0.65	0.39	0.61	0.67	0.48
Finland	0.69	0.68	0.35	0.63	0.65	0.22	0.70	0.68	0.35

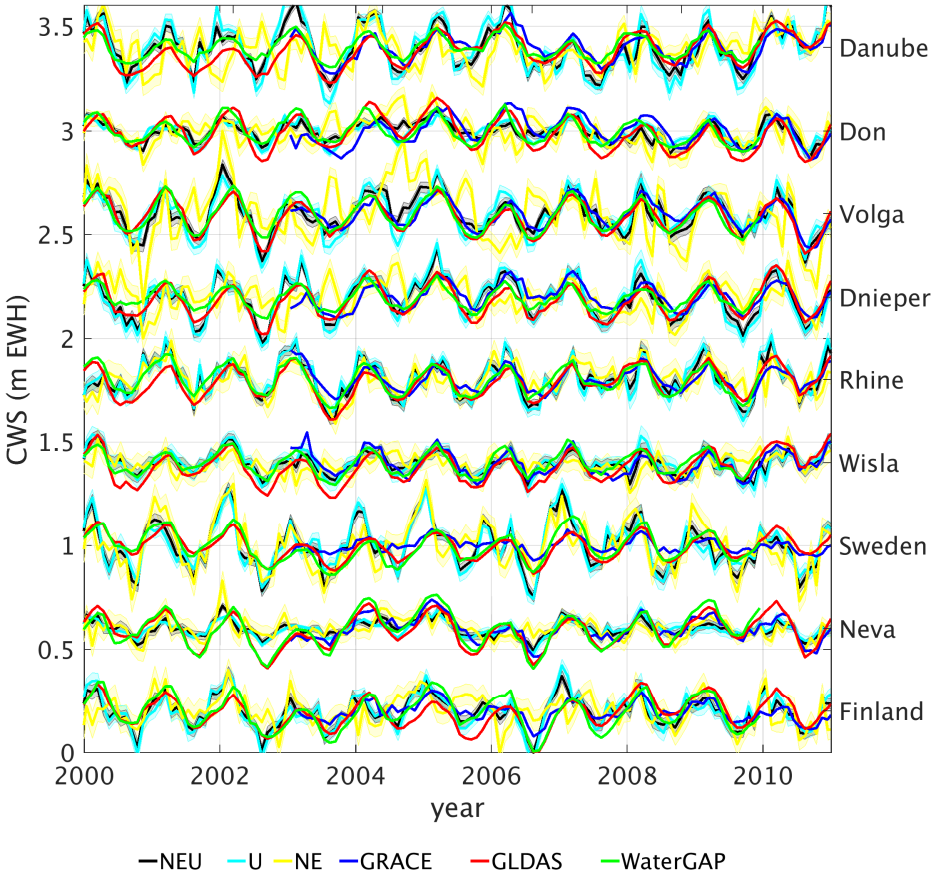

Figure 3.19: CWS inferred from GPS time series in Europe. CWS inferred from simulated 3D, vertical only and horizontal only are in black, cyan and yellow, respectively. CWS from GLDAS (red) is used as reference source. Shade area represents the corresponding one sigma standard deviation.

Table 3.13: WRMSR of the inferred CWS from GPS comparing to CWS from reference sources in Europe

basin	GRACE			GLDAS			WaterGAP		
	NEU	U	NE	NEU	U	NE	NEU	U	NE
Danube	-10.71	2.77	-19.03	-0.87	5.83	-17.51	14.45	23.35	-9.82
Don	40.24	42.99	1.86	40.79	51.03	-2.07	37.04	48.08	-7.15
Volga	34.84	30.19	3.57	45.44	40.26	-11.33	39.55	34.42	-2.29
Dnieper	37.46	32.20	24.22	33.95	29.27	15.10	44.23	39.96	19.12
Rhine	22.10	24.63	-25.40	0.13	10.93	-49.73	30.29	39.21	-33.58
Wisla	15.05	12.74	12.69	17.17	14.39	10.52	19.91	15.22	14.70
Sweden	1.10	-3.51	-12.39	-46.69	-40.01	-49.93	-62.34	-57.71	-60.18
Neva	22.25	28.96	10.97	15.15	13.72	7.54	18.94	8.22	11.99
Finland	27.85	26.03	2.24	13.75	20.56	-26.09	18.10	21.10	-24.41

3.5. Conclusions

In this chapter, we used 3-D GPS to invert for water storage over the Amazon River basin, North America, and Europe. Due to the different GPS station density in the two regions, two different approaches to the inversion were applied: single basin inversion and multiple basin joint inversion. For the regions where there are very few GPS sites and strong mass loads, such as the Amazon, CWS can be obtained using our single basin inversion scheme. For the basins which do not have a significantly larger load than the surrounding regions and a large coverage of GPS sites available, the multiple basin inversion is suggested.

From the GPS time series simulation, we found that the uncertainties in the GPS observations need to be re-estimated for the inversion. In this thesis work, we re-estimate the horizontal uncertainties from the discrepancies between the GPS observations and the hydrological models. As the hydrological models are consistent with one another and with GRACE, this re-estimation can provide reasonable uncertainties in the GPS time series for the mass load studies. Vertical uncertainties are the original uncertainties scaled up by a factor of five of the original uncertainties. After re-estimating the GPS uncertainties, the inferred CWS uncertainties become reasonable.

The CWS inferred from the GPS three-dimensional time series consistently agree with the CWS from GRACE and the hydrological models in all three regions. The correlation between the inferred CWS and from the reference sources reaches 0.87 with the WRMS being reduced by up to 46.2%. All the statistical comparison results between the inferred CWS and from reference sources confirm that the GPS can be used to infer the CWS changes.

Horizontal displacements of GPS observables contribute significantly to the inversion scheme. In the multiple basin inversion scheme without regularization, the horizontal displacements have relative contributions of about one third for the center basin. The main contributor to the multiple basin inversion scheme is the vertical signals, as the loading response for the verticals are stronger than the horizontal displacements.

In order to test if the GPS horizontal displacements driven by the loading signal improved the inversion, we performed closed-loop simulations and found significant improvement on the estimated CWS. We extend the comparison with the GPS time series, majority of the basins show improvements after we include the horizontal coordinate time series in North America. No significant improvements are found in Europe, due to the high condition number of the direct inversion scheme (without regularization). After introducing the regularization parameter, signals in the horizontal time series as well as the noise are suppressed.

Chapter 4. Unresolved signals in regional inversion study

Before trying to invert the GPS observations for estimates of water storage, a clear understanding of the error sources within the linear system is required. This and the following chapters are devoted to systematic error assessments of the inversion. This chapter discusses the unresolved signals in the analysis area: the far-field and near-field effects. In the regional study, the mass variations outside of the research interest is commonly excluded. This exclusion leads to what we call the far-field effect that is discussed in the following section. In contrast to the far-field effect, near-field effects are the omission of the spatial details in the regional modelling and calculation.

4.1. Spatial truncation error: far-field effect

The vertical surface displacements recorded at any GPS site represent the integral of mass loading over the whole globe. In the regional studies by (Amos et al., 2014; Argus et al., 2014; Borsa et al., 2014; Fu et al., 2015), the authors assume that the surface displacements are driven only by mass changes in the near field of the GPS stations. Certainly, most of the surface displacement come from loads in the near field but not all. The difference between the surface displacements driven by the global mass variations and those caused by regional mass changes is what we here call the STE.

STE is caused by omitting the far-field load. Schrama (2005) discussed the far-field effect and near-field contribution. Small differences were found for the near-field effect within 10°, 20° and 40° for a constant load layer. However, the conclusions derived for the constant load may differ from the displacement time series from the

geographical distribution of the true load.

Similar issues have been discussed for the atmospheric pressure variations on gravity. Spratt (1982) found the local pressure variations cannot precisely correct gravity for global atmospheric mass variations. Merriam (1992) found that a zone between 50 km and 1000 km from the gravity station contributes a couple of μGal as the same amplitude from the remainder of the globe. It is important to highlight that the gravity changes decay faster than the vertical displacement with distance from the observation (Farrell, 1972). A more recent study (Boy et al., 2003) shows ocean tidal gravity variations are mostly dependent on tidal height variations within a radius of 50 spherical degrees of a gravity station using the highly precise observations from super-conducting gravimeters.

The remove-compute-restore technique is widely used for regional geoid determination. The low wavelength geoid is removed from the regional calculation scheme, later restored, with the obtained high wavelength geoid signal to cover the regional details and avoids the need to implement Stokes' integral to an ultra-high order (Sjöberg, 2005). This technique can also be introduced into the regional loading displacements study for the high spatial continental water storage determination. Currently the inversion in this thesis focuses on the basin mean variations, which are mainly the low wavelength signal, and thus it will not be employed for this stage.

Unlike the regional CWS inversion studies, the global mass redistribution studies from inverting displacement observations (e.g. Kusche and Schrama, 2005; Kusche et al., 2007; Wu et al., 2010, 2012) are not affected by STE as the far-field effect is included in the global modelling usually through the global Stokes coefficients. Due to the uneven distribution of the stations (GNSS, VLBI, SLR etc.), regional inversions can benefit from the dense network in some regions (e.g. Europe, North America, and Japan) to infer regional mass changes (e.g. Borsa et al., 2014). Then STE should be used as an estimate of one of the errors in the inversion.

In this section, a series of simulations are performed to estimate the amplitude of STE in CWS inversions. CWS is obtained from the hydrological models. The vertical surface displacements are obtained using input from soil moisture and snow (equivalent water thickness) from the GLDAS model. Then the surface displacements are recalculated using mass data within increasing angular distances of the sites. When the inversion area extends up to 20° of the distance from the observation site, STE falls below the GPS noise level, i.e. it can be ignored. The nature of reducing the STE in regional inversions includes removing the STE using a given hydrological model. Our simulations show that after subtracting the far-field effect using a hydrological model, the STE is significantly reduced.

4.1.1 Homogeneous load case study

Suppose we have a spherical Earth without oceans that is covered by a homogeneous load P. From Eq.(2.9), the horizontal displacements are zero. The vertical displacement, $u(\psi)$ which is induced by the mass load within the spherical distance ψ, is obtained from Eq.(2.8). Then the ratio, $r(\psi)$, of the displacement driven by the regional mass U_ψ and the displacement from the global mass field, U_g is:

$$r(\psi) = \frac{U_\psi}{U_g} = \frac{\int_0^\psi G(x)\sin x dx}{\int_0^\pi G(x)\sin x dx} \ . \tag{4.1}$$

The ratio with respect to as a function of increasing the area of the mass included in the displacement calculation (angular radius) is shown in Figure 4.1. The ratio is zero when $\psi = 0^\circ$, then it increases to a maximum at around 40 degrees then decays to a minimum at around 105 degrees. The fluctuation is caused by the sign change of Green's function with increasing angle, see Figure 2.1.

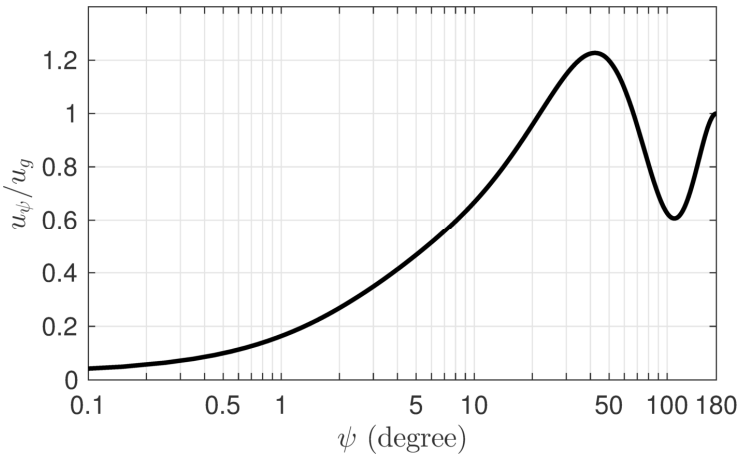

Figure 4.1: The displacement ratio for homogeneous load over the Earth.

4.1.2 STE for the whole globe

We obtain CWS variations using the soil moisture and snow/ice mass from the GLDAS from Jan. 1999 to Dec. 2008. The CWS in Greenland is excluded due to the unrealistic glacier dynamics there (Jiang et al., 2013). GLDAS data are provided at a monthly resolution and at 1 degree by 1 degree spatial sampling over the continents. Before using the GLDAS data, Greatbatch approach (1994) is adopted, thus the trends are removed for each grid cell. Due the trend in GPS coordinate time series are dominated by the tectonics and the post glacial rebound, the corresponding linear trends are removed in GPS time series. For the consistency reason, the linear trends within the hydrological models, currently GLDAS in use, are removed.

Water storage variations dominate the annual signals in GPS vertical coordinate time series (Blewitt et al., 2001; van Dam et al., 2001). The soil moisture and snow/ice equivalent water thickness from GLDAS model have been compared with mass estimates derived from the GRACE time variable gravity field and GPS data, agreements between GLDAS CWS and observations have been demonstrated (Landerer and Swenson, 2012; Jiang et al., 2013 among others). These studies demonstrate that GLDAS represents a reasonable estimate of the periodic CWS variation. Thus, GLDAS can be used to simulate real changes in water storage to analyze STE.

Mass-loading Green's functions (Farrell, 1972) estimate the displacements at a point due to a load at another location and are derived on a spherically symmetrical, non-rotating, elastic and isotropic Earth. Although regional differences in the Earth's lithosphere can cause differences in the predicted displacements (Wang et al., 2013), so far no evidence really demonstrates that a regional Earth structure difference is the main cause of the disagreement between predictions and observations of surface displacement. Green's functions derived for regional crust (Seitz and Krügel, 2009) produce differences up to 2 mm in predicted surface displacements. However, the difference between Green's functions from the spherically symmetric Earth model and half-space approximations are not significant at the global scale (Gegout, 2013).

The 3-D displacements, $X = [X^N X^E X^U]^T$, at a point on the Earth's surface (θ_p, λ_p) due to mass variations, Δm_i, distributed over the globe can be discretized from Eq.(2.6) as

$$\mathbf{X}_g(\theta_p, \lambda_p) = \sum_{i=1}^{N_g} \Delta m_i(\theta_i, \lambda_i) \begin{bmatrix} -G_i^y(\psi_i)\cos(\alpha) \\ -G_i^y(\psi_i)\sin(\alpha) \\ G_i^u(\psi_i) \end{bmatrix}, \tag{4.2}$$

where N_g is the total number of load units of the decomposed mass load acting over the Earth's surface. θ_i and λ_i represent the latitude and longitude of the given point on the Earth where the loading effect is being determined. ψ_i is the angular distance between (θ_p, λ_p) and (θ_i, λ_i). The spatial grid of (θ_i, λ_i) is defined by resampling the GLDAS grid into rings as it is shown in Figure 2.3. The rings $\psi < 1^\circ$ are divided into 0.01° degree step size and for the rings locate further away are divided with 0.1° degree step size. Each ring is subdivided into 100 azimuth units for $\psi < 10^\circ$ and 360 azimuth units for $\psi > 10^\circ$.

To estimate the displacement due to mass changes within a specific region, i.e. for $\psi < \psi_0$, the limits of the summation in Eq. (4.2) would extend only over N_{ψ_0}, the

total number of load units for $\psi < \psi_0$. Thus,

$$\mathbf{X}_{\psi_0}(\theta_p, \lambda_p) = \sum_{i=1}^{N_{\psi 0}} \Delta m_i(\theta_i, \lambda_i) \begin{bmatrix} G_i^v(\psi_i)\cos(\alpha) \\ G_i^v(\psi_i)\sin(\alpha) \\ G_i^u(\psi_i) \end{bmatrix}. \tag{4.3}$$

Then STE is defined as the difference between the displacements from global and regional mass variations:

$$STE_\psi = \mathbf{X_g} - \mathbf{X_\psi} \ . \tag{4.4}$$

4.1.3 Results and Discussions

Three groups of simulation studies are performed in this section. In the first part, the STE effects at the center of two major river basins demonstrate the STE effect with increasing load extent. Then surface displacements are determined based on a global analysis. In the last part of this section, the error of using the hydrological model to remove the far-field effects is discussed.

STE at the center of the Danube and Amazon River basins

The simulation is carried out at the center of the Danube and Amazon River basins from GLDAS monthly CWS. We estimate the Root-Mean Square (RMS) of ε_ψ and plot the results in Figure 4.2. When $\psi = 0°$, $\mathrm{RMS}(\varepsilon_\psi) = \mathrm{RMS}(\mathbf{X_g})$ and when $\psi = 180°$ which means a global loading covering, $\mathrm{RMS}(\varepsilon_\psi)=0$. In Figure 4.2, for ψ greater than 10 degrees, $\mathrm{RMS}(\varepsilon_\psi^U)$ of both Amazon and Danube River basins fall in sub-mm level, meanwhile, the horizontal STE decreases more slowly than that for the vertical component. The horizontal ε_ψ^{NE} of Danube Basin reaches its first minimum at $\sim 40°$ degrees and for ε_ψ^{NE} of Amazon Basin around $20°$. For Amazon Basin, the ε_ψ^N stay above 0.1 mm even up to $130°$. The horizontal motion is more sensitive to the far-field mass load.

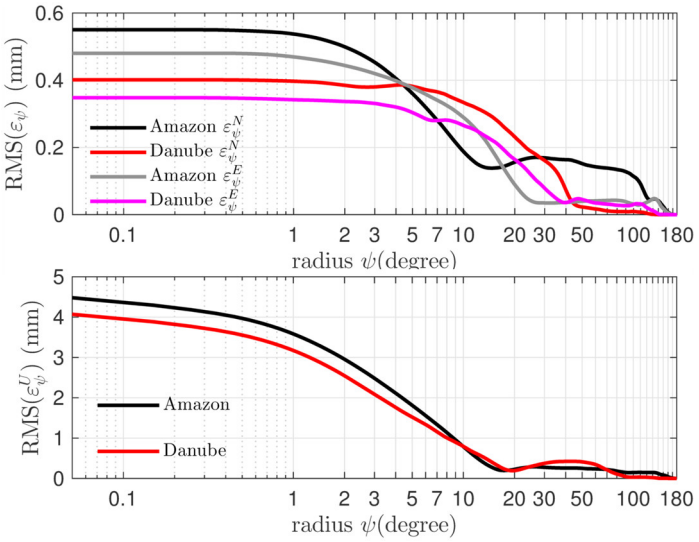

Figure 4.2: STE for the Amazon and Danube River Basins. Top Panel: horizontal $\mathrm{RMS}(\varepsilon_\psi)$ *at the center of the Amazon and Danube River basins as a function of the angular distance from the site,* ψ*, from which data are included in the calculation of the displacements. Bottom Pane: vertical* $\mathrm{RMS}(\varepsilon_\psi^U)$ *at the center of Amazon and Danube River basins.*

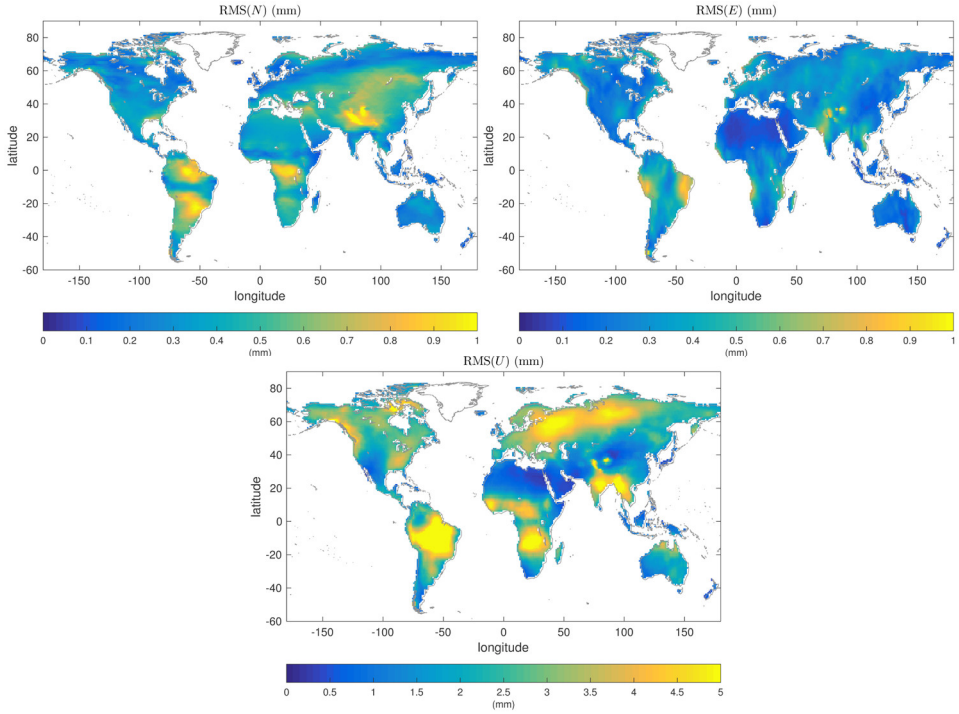

Figure 4.3: RMS of CWS induced displacements using 10 years of GLDAS data. Top Left Panel: North component; Top Right Panel: East component; Bottom Panel: Up component.

The results from the Amazon and the Danube River basins indicate that the regional

contribution to the displacement at any point (angular distance, ψ, from the site) varies from site to site. For a better understanding of how much data is required to obtain reliable estimates of surface displacements comparable to those obtained using a global dataset for all points on the surface of the continents, we performed a simulation study for the STE effect for continental sites on a $1^\circ \times 1^\circ$ degree grid.

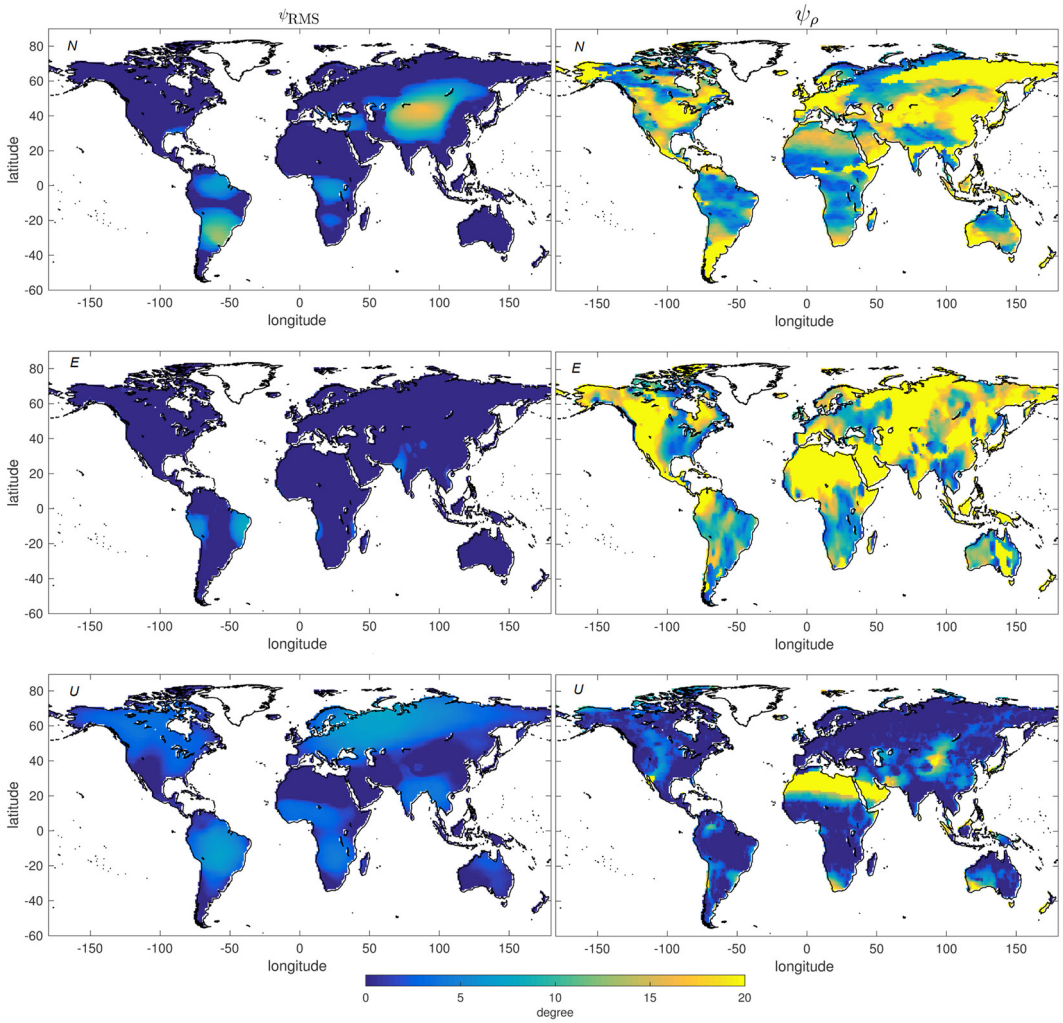

Figure 4.4: Coverage requirement derived from the RMS and correlation threshold.

Coverage requirement for regional CWS study

The error budgets of GPS coordinates are on the order of 0.7 0.7 and 2.2 mm for weekly north, east and up samples, respectively (Ray et al., 2011). If $\varepsilon_\psi < \begin{bmatrix} 0.7 & 0.7 & 2.2 \end{bmatrix}^T$ mm, then beyond this limit of ψ, the STE can be neglected. In

the discussion below, we define the values of acceptable RMS(ε_ψ) $\leq$ $\left[0.7 \quad 0.7 \quad 2.2\right]^T / \sqrt{2} \approx \left[0.5 \quad 0.5 \quad 1.5\right]^T$ mm and the correlation between the regional and global vertical surface displacements, $\rho(U_{g(\theta,\lambda)}, U_{\psi(\theta,\lambda)}) \geq 0.9$. In order to determine the required coverage radius ψ, ε_ψ is estimated at each grid unit $(1^\circ \times 1^\circ)$ for each ψ from 0° to 180° with a 0.1° step size. Then the corresponding $\psi(\theta,\lambda)$ from RMS($\varepsilon_{\psi(\theta,\lambda)}$) $= 1.5$ mm and $\rho(U_{g(\theta,\lambda)}, U_{\psi(\theta,\lambda)}) = 0.9$ are solved using a spline interpolation, see Figure 4.4. The RMS amplitude of the displacements induced from CWS, RMS($\mathbf{X}_g$) is plotted in Figure 4.3.

Two main factors are found which strongly influences the load coverage requirement, ψ. The first is the distance of the given site to the ocean. For sites near coastlines, the CWS load is located to one side of the site (there are no CWS mass changes over the oceans). CWS is smaller for the same ψ, as compared to a point in the middle of a continent with the surrounding load of the same amplitude. The vertical displacement at coastal sites is smaller. Thus, a larger percentage of the displacements are driven by mass changes further away than for sites located inland.

The second factor is the amplitude of the nearby regional CWS variations. For locations with small CWS signals, e.g. the Danube (the RMS of CWS is ~ 10 cm of Equivalent Water Height for the entire time span from GLDAS), the displacement induced by loads in the near field is small as compared to a site in the Amazon River Basin. Thus, for the same displacement amplitude, a larger area for the input mass change is required. The larger the regional signal, the less data is required to approach the global signal. Contrarily, for desert regions such as the Sahara in North Africa and the Arabian Peninsula, the RMS of the CWS variations are less than 5 cm of Equivalent Water Height (EWH) for the entire time span from GLDAS. Load induced displacements in these locations are driven by distant mass changes.

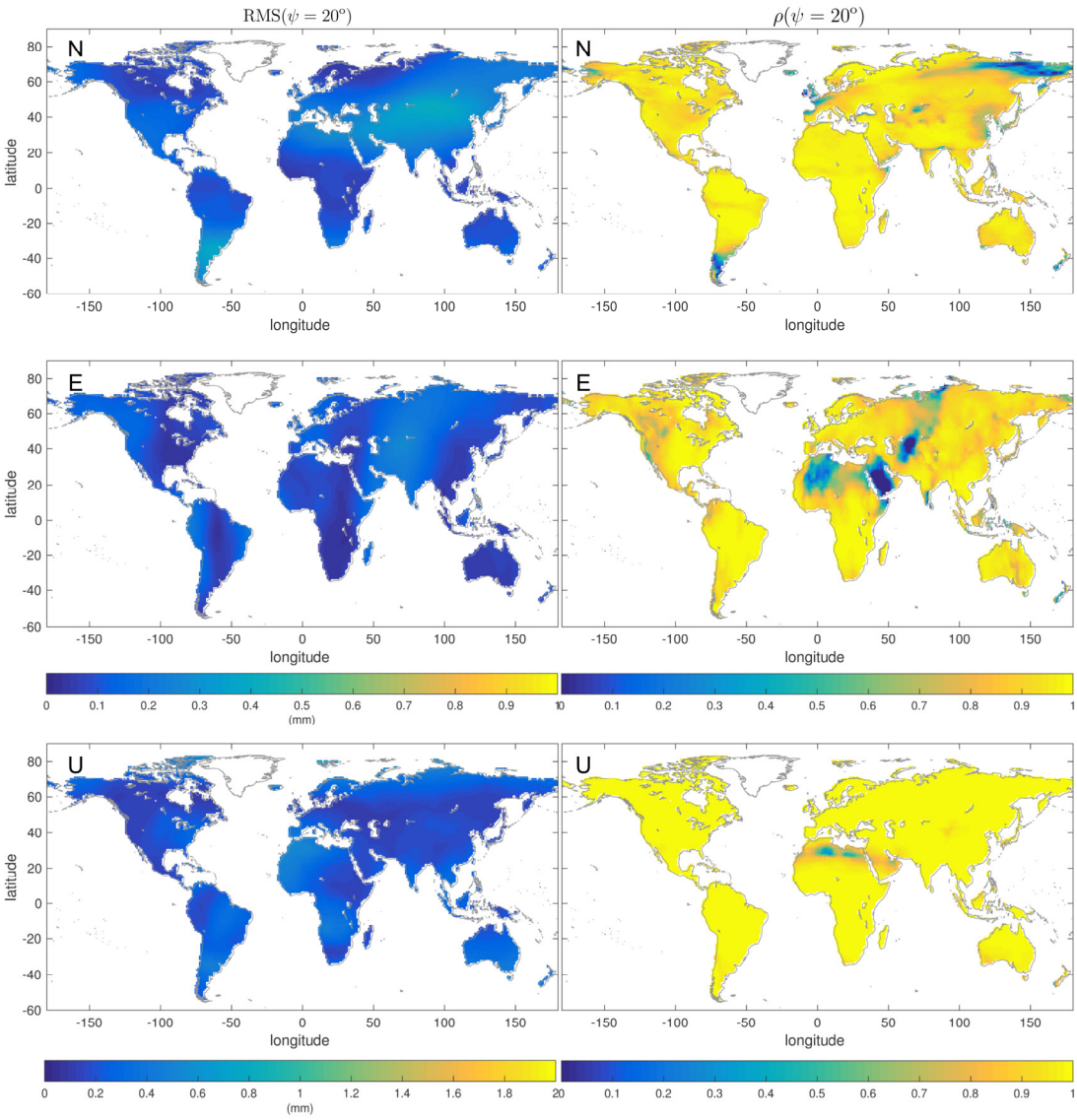

Figure 4.5: The STE for $\psi = 20°$. Right Panels: RMS of the STE for North (Top), East (Middle) and Up (Bottom) components in mm. Left Panels: Correlation between the regional CWS induced motion $(\psi \leq 20°)$ and globally induced motion for North (Top), East (Middle) and Up (Bottom) components.

In Figure 4.3, the top panel shows RMS($\mathbf{X_g}$) from ten years of GLDAS data. Only about 60% of the points in this figure have a RMS($\mathbf{X_g}$) $\geq$ 2 mm, i.e. RMS($\mathbf{X}_g^U$) above the GPS noise threshold. The coverage requirement of the RMS threshold, $\psi_{\text{RMS}(\varepsilon)\leq 1.5 \text{ mm}}$ is mapped in Figure 4.4 (right panels). The area over which we have a load that gives the minimum correlation threshold, $\psi_{\rho(\mathbf{X_g},\mathbf{X_\psi})}$ is plotted in Figure 4.4 (left panels). In the middle of the Amazon, using mass change over an area of only

seven degrees of angular distance from the center, the displacements can be reliably determined (below the GPS vertical error) rather than using data from the entire globe. For most other locations, a sufficiently precise estimate of the global CWS loading effects can be calculated using CWS data within 10° degrees of the site. The correlations require higher coverage for the desert/dry and coastal region, due to the small loading.

Three conclusions can be drawn from Figure 4.4. Firstly, 60% of the continental regions have a RMS of the vertical displacement above the minimum noise level of 2 mm. Though the RMS threshold is fulfilled, global information on the mass load is suggested for the regional CWS study. Second, for most of the continental regions, load data within 20° of a station is sufficient for a regional CWS study except in the deserts and coasts. Third, the minimum requirement of area from which we require loading information shows that the displacements are a localized signal and have an amplitude considerably larger than the noise level in the GPS data.

Choosing the $\psi = 20^\circ$ over the globe, the RMS($\varepsilon_{\psi=20^\circ}$) and $\rho(\mathbf{X}_g, \mathbf{X}_{\psi=20^\circ})$ are calculated for the corresponding grids, see Figure 4.5. The RMS of STE from the far field (further than 20°) reaches up to 0.5 mm. The maxima appears mainly along the coastal regions and the center of Eurasia. The correlation falls below 0.9 in the desert, coastal and island regions.

4.1.4 Far-field effect eliminated from external hydrological model/dataset

Rather than ignoring the mass in the far-field, another solution could be to use a hydrological model to remove displacements from mass variations distant from the site. Since there are no precise global CWS observations at a high spatial resolution and the accuracy information of the hydrological model is unavailable, in this study, we assume that the residual of the CWS between two individual hydrological models

is noise.

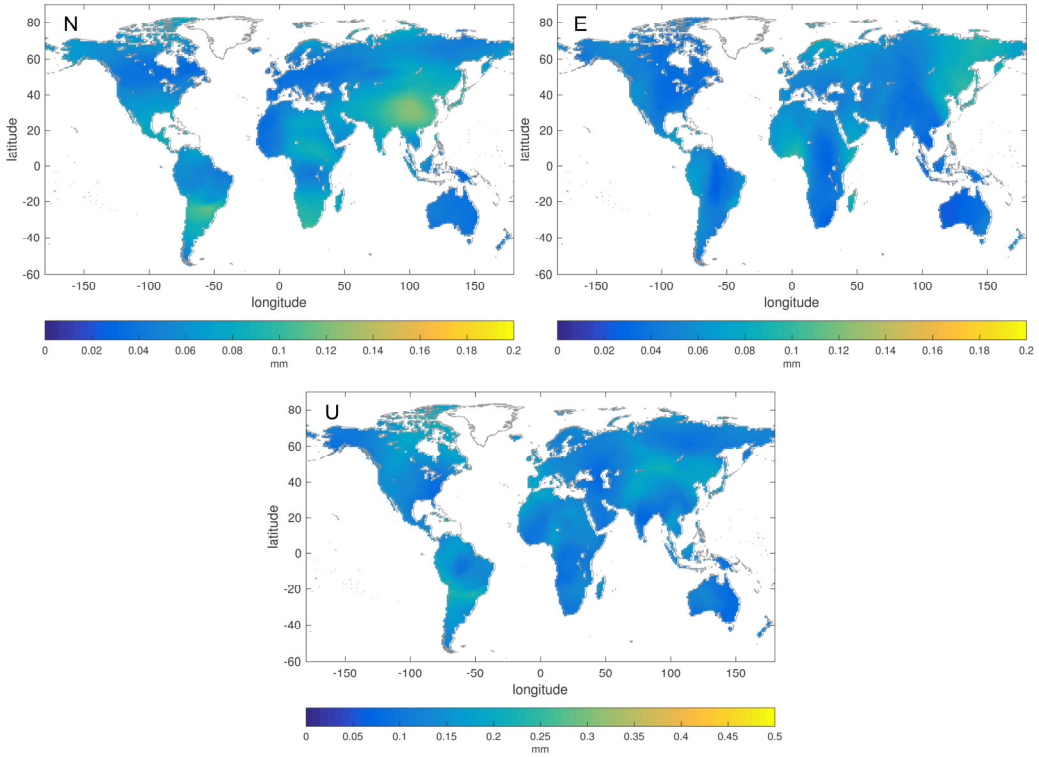

Figure 4.6: RMS($\zeta_{\psi=20^\circ}$) *between GLDAS and WaterGAP in north (up left), east (up right) and up (bottom) directions, in units of mm.*

A second CWS is obtained from WaterGAP version 2.2 (Döll et al., 2003). Then, the calculation in the last sub-section is repeated by replacing the GLDAS with the residuals between GLDAS and WaterGAP, $\zeta = H_{\text{GLDAS}} - H_{\text{WaterGAP}}$, where H is the equivalent water height from each of the hydrological models. The RMS of the far-field effect for $\psi = 20^\circ$, RMS($\zeta_{\psi=20^\circ}$), is shown in Figure 4.6. By subtracting the surface displacement driven by the mass in a hydrological model, the amplitude of RMS($\zeta_{\psi=20^\circ}$) is only half of the RMS($\varepsilon_{\psi=20^\circ}$) in Figure 4.5. For removing the effect of distant masses in GLDAS from the WaterGAP model, the error for coastline sites is greatly reduced. Applying the correction for the far-field masses is suggested for any regional CWS inversion study. Although this approach will introduce an error due to the uncertainty of the used hydrological model. Compared to the amplitude of STE,

the error introduced by mis-modelling (assume the difference between GLDAS and WaterGAP are the mis-modelling error) of the far-field load is smaller.

4.1.5 Conclusions

Omitting the far-field mass variations in the inversion of GPS data for regional CWS leads to what we have termed a spatial truncation error (STE). The displacements at any place are driven by the mass variations over the globe. The spatial truncation error, which represents the differences between displacements calculated using a global or regional mass can, in general, be mitigated by using data within 20° degrees of the station.

Within the 20° degrees around the site, the continental water storage (CWS) induced vertical surface displacement is a proper approximation of global CWS induced displacements. The RMS of the STE is only 0.5 mm for the coastal regions and for the desert/dry regions where the CWS amplitude is also small. Using data from a larger area is suggested even for regional studies in dry regions, as displacements induced from the far-field are significant compared to the loading signal in the dry region. The spatial requirement of the data coverage for the regional study is affected by the mass redistribution in the surrounding area.

For the regional water storage study, removing the far field effect (larger than 20° degrees of arc) from a proper hydrological model is suggested. In the simulation, by subtracting hydrological model, the far-field effect can be removed, while the mis-modelling error introduced to the displacement time series is only half of the amplitude of the removed STE.

4.2. Parameterization error: near-field effect

Regional continental water storage is commonly modelled as mass variation on the

spatial grid (Argus et al., 2014; Fu et al., 2015) or analysed at the basin scale (Swenson and Wahr, 2002; Swenson et al., 2003; Hirschi, Seneviratne, et al., 2006; Hirschi, Viterbo, et al., 2006; Hirschi et al., 2007). Due to limited observations of the displacements (GPS sites), the spatial resolution of the regional inversion is limited as well, no matter what the spatial grid or the basin scale. In the thesis, the mass changes are modelled as mean basin variations. The differences between the displacements induced from real mass distribution and the mean basin variations are the unresolved near field errors.

Two aspects of this problem are discussed in the following sub-sections. In the first sub-section we estimate the parameterization error from the modelling with a series of closed simulations based on ten years of WaterGAP (sum of the canopy, snow/ice, soil moisture, surface water and groundwater storage) (Döll et al., 2012) from Jan. 1999 to Dec. 2008. An inversion for regional CWS is usually modelled as a basin average, over a grid, or using local base functions. The basic unit of the hydrology is the drainage basin (Lutgens et al., 1995), which is the most common analysis unit in term of the hydrological effect including the continental water storage (e.g. Rodell and Famiglietti, 1999). Excluding the mass variations within the basin leads to an error of the near field. In the second sub-section, we discuss the near-field effects for the globe as well as the spatial resolution influence in the mass loading displacements.

4.2.1 Basin mean variations

Due to the limited availability of data, the spatial resolution of the inversion is limited. As the inversion study here is at the basin scale, the near-field effect of the unresolved signal (NFE) is the discrepancy between basin mean versus the actual spatially distributed mass changes. The NFE, $\varepsilon_{\bar{m}}$, between the displacement induced from the Global CWS variations and the basin average is defined as

$$\varepsilon_{\bar{m}} = \mathbf{X}_m - \mathbf{X}_{\bar{m}} \tag{4.5}$$

where $\bar{m} = E(\Delta m_i),\ i \in \Omega$, denotes the mean mass variation within the basin Ω.

The logic of the simulations is shown in the flowchart in Figure 4.7. The mass loading displacements are calculated from the mean mass variations and the original CWS within the basin. The surface displacements are obtained from the mass variations and then compared with the displacements induced from basin mean. The near-field effect is first investigated in selected basins (Amazon, Danube and St. Lawrence River basin) then extended to all river basins.

The results for the Danube River Basin are presented in Figure 4.8. The maxima of horizontal displacements, $\mathbf{X}_{\bar{m}}^{N}$ and $\mathbf{X}_{\bar{m}}^{E}$, are located at the side of the river basin while the vertical displacements $\mathbf{X}_{\bar{m}}^{U}$, the maximum appears in the center of the basin. The horizontal displacements located at the "median line" of the basin are zero, due to the fact that the load on one side of the basin cancels the load on the other side of the basin if the mass is evenly distributed on the both sides. The vertical displacements, however, result from mass contributions from the both sides that accumulate as the load pushes the crust downward at its center. The effects are presented in Eq. (2.9) without considering the basin shape.

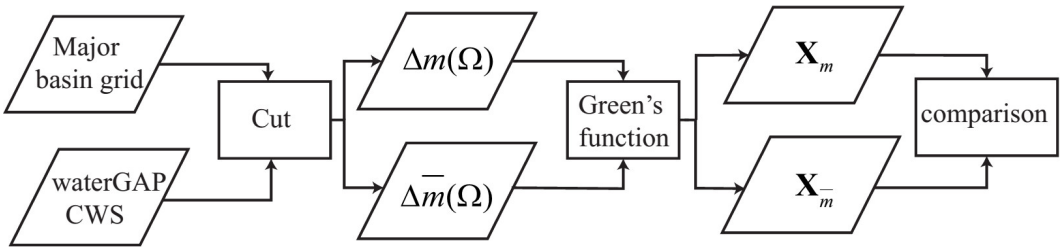

Figure 4.7: Simulation flowchart for analyzing parameterization error of modelling basin average excluding the spatial information within the basin.

From the residuals $\varepsilon_{\bar{m}}$, it is obvious that the near-field signal/high spatial resolution signal is missing in $\mathbf{X}_{\bar{m}}$. The $\mathrm{RMS}(\varepsilon_{\bar{m}})$ in the right column of Figure 4.8, due to the

unresolved high spatial resolution signal, the near-field effect represents a significant error for all three components. Moreover, the influence is larger for the horizontal displacements, as no significant RMS Reduction (RMSR) can be found for all the basins in Table 4.1, compared to the mean RMS of the induced displacements $\overline{\mathrm{RMS}}(X_m)$. Vertical components are less effected, the $\overline{\mathrm{RMS}}(\varepsilon_{\bar{m}})$ reduced to half of the $\overline{\mathrm{RMS}}(X_m)$.

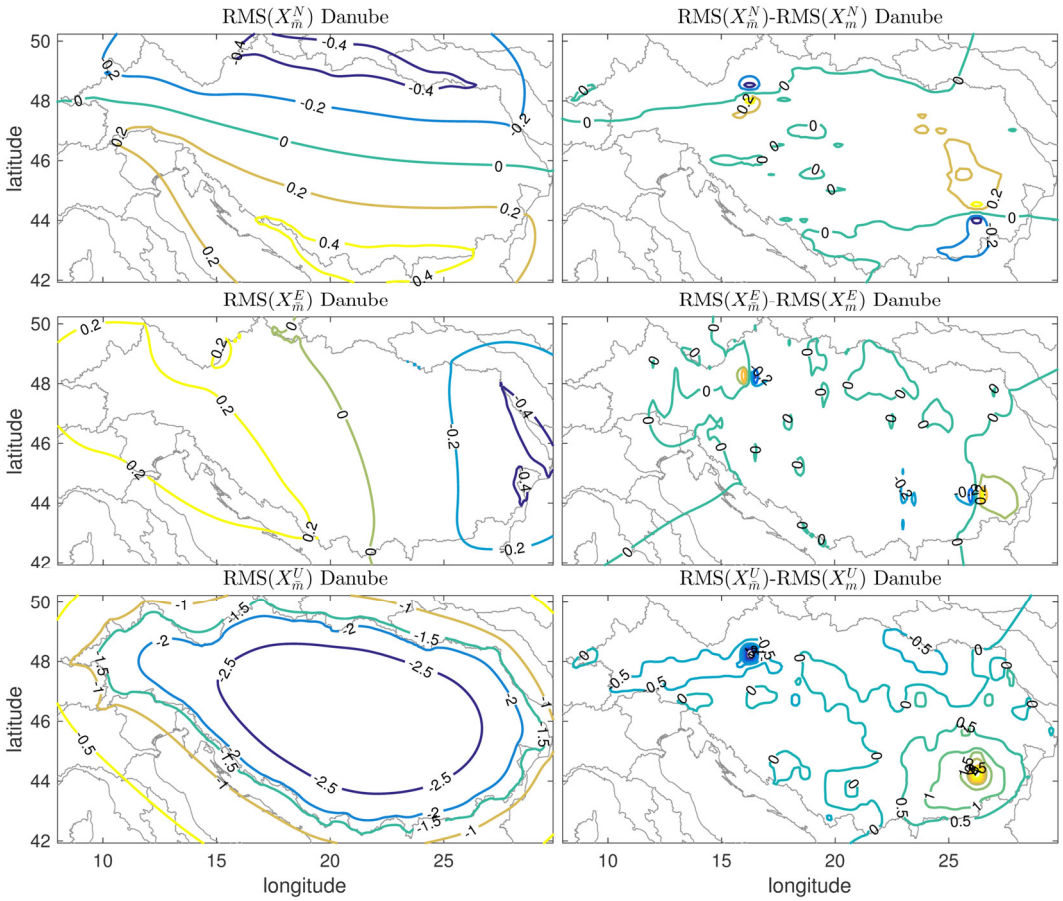

Figure 4.8: Near-field effect in Danube Basin. RMS of the displacements (North in Top Left, East in Middle Left and Up in Bottom Left) induced from the mean CWS derived from 10 years of WaterGAP data. Right Panels present the RMS of the differences between the displacement derived from mean CWS, $X_{\bar{m}}$, and from spatial distributed CWS, X_m. The unit is in mm.

4.2.2 Close field effect over the globe

The NFE of the single basin case was discussed in the former section, but NFE is

also accumulating for the whole globe. To understand this, a case study is performed in Figure 4.9, by comparing the displacements derived from the WaterGAP and basin averaged WaterGAP CWS data. Extending this investigation from one basin to the globe cannot be avoided for quantifying the error of the basin mean model.

Table 4.1: Statistics of NFE. Unit: mm

Basin	$\mathrm{Max}(X_{\bar{m}})$			$\overline{\mathrm{RMS}}(\varepsilon_{\bar{m}})$			$\overline{\mathrm{RMS}}(X_m)$		
	N	*E*	*U*	*N*	*E*	*U*	*N*	*E*	*U*
Amazon	3.46	3.20	21.54	0.47	0.31	2.60	0.30	0.29	4.32
Danube	0.63	0.78	4.86	0.06	0.07	0.38	0.11	0.09	1.31
St. Lawrence	3.61	3.71	35.50	0.18	0.20	1.05	0.17	0.14	2.21

As expected, the vertical components do not show a strong deviation except in regions with large loading signal regions such as Amazon or the Himalaya Mountain regions. Correlation differences are mostly located at the coast, which is understood as being due to the fact that the load signals are small here. The $\mathrm{RMS}(\varepsilon_{\bar{m}})$ exactly represents the details within the basin, which can be seen clearly from Amazon Basin and others. The correlations of the horizontal displacements fall below 0.5 mostly in the median line of all the basins, as shown in Figure 4.8.

4.2.3 Influence of the spatial scale on the response of load

Improving the regional mass variation model can surely reduce the NFE, but at the same time, the increase of the spatial resolution dramatically increases the number of unknowns in the inversion system. The balance between the spatial resolution and NFE is discussed in this section.

The spatial resolution in spatial domain is represented as the grid size, while in spectra domain then the spatial resolution depends on degrees of the Stokes coefficients. Here we extend the spatial resolution study in the spectra's domain for only vertical displacements in (Yan et al., 2016) to all the three dimensional displacement components.

The Stokes coefficients[2] (C_{lm}, S_{lm}) of CWS obtained from GLDAS are provided through GGFC Special Bureau for Hydrology. Then the displacements parameters are obtained based on Eq. (2.22) and Eq. (2.21):

$$\begin{bmatrix} (C_{lm}^N, S_{lm}^N) \\ (C_{lm}^E, S_{lm}^E) \\ (C_{lm}^U, S_{lm}^U) \end{bmatrix} = \begin{bmatrix} \frac{-al_l}{1+k_l}(C_{lm}, S_{lm}) \\ \frac{-al_l}{\sin\theta(1+k_l)}(C_{lm}, -S_{lm}) \\ \frac{ah_l}{1+k_l}(C_{lm}, S_{lm}) \end{bmatrix} \tag{4.6}$$

In order to analyse the influence of different spatial resolutions on the displacements, the degree RMS of displacements Stokes coefficients are obtained from:

$$\mathrm{RMS}_l = \sqrt{\frac{\sum_{m=0}^{m=l}\left[\left(C_{lm}^d\right)^2 + \left(S_{lm}^d\right)^2\right]}{2l+1}} \tag{4.7}$$

where $C_{lm}^d \in \{C_{lm}^N, C_{lm}^E, C_{lm}^U\}$ and $S_{lm}^d \in \{S_{lm}^N, S_{lm}^E, S_{lm}^U\}$. The factor used to transfer displacement Stokes coefficients from the fully normalized Stokes coefficients is given in Eq. (4.6).

The stacked RMS_l obtained from the monthly GLDAS (from Jan. 2002 to Dec. 2014) and GRACE data (from Jan. 2003 to April 2013, details are presented in Section 2.2.2) are illustrated in Figure 4.10. The amplitude of the degree RMS gradually decreases and follows a power law (not the Kaula curve as it is not for the displacement Stokes coefficient). GRACE degree RMS deceases for the low degrees and increases again for the higher degrees, due to the error in GRACE time variable gravity field. The $\sin\theta$ in Eq. (4.6) and the differences between the normalized Legendre polynomial $\bar{P}_{lm}$ and the first derivative $\partial\bar{P}_{lm}(\cos\theta)/\partial\theta$ are excluded in the spectra discussion.

[2] Monthly fully normalized Stoke's coefficient is obtained from the soil moisture and snow equivalent water from GLDAS NOAH model. Time span: Jan. 2002 to Dec. 2014. Maximum degree/order: 100 (Chen, 2015)

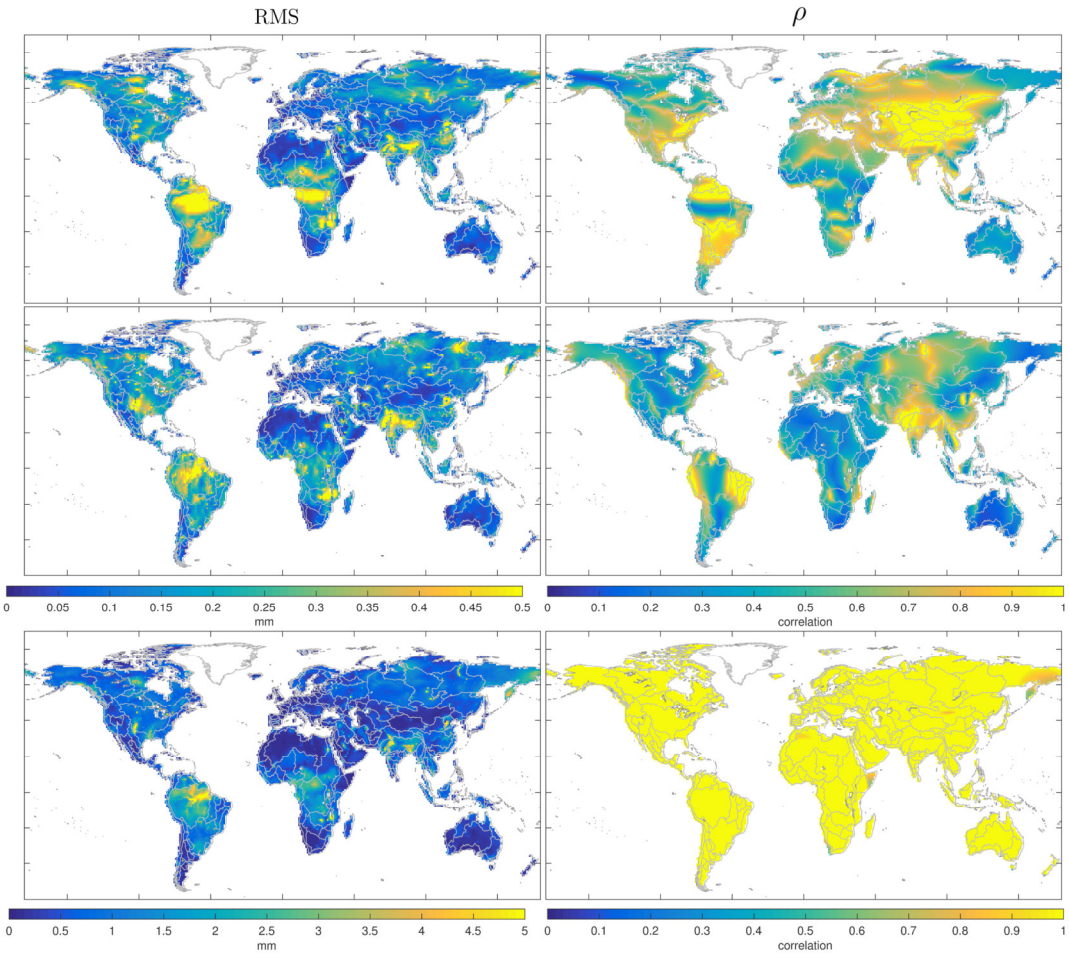

Figure 4.9: Near-field effect for unresolved mass variations within major basins. Right Panels: RMS of NFE for North (Top), East (Middle) and Up (Bottom) components in mm; Left Panels: Correlation between the basin mean CWS induced motion and globally induced motion for North (Top), East (Middle) and Up (Bottom) components.

From Figure 4.10, it is clear that after degree 20 (corresponding to ~1000 km spatial resolution), no significant contribution to the accumulated degree RMS can be detected for GLDAS CWS derived displacements. This result is true for all the three components. Horizontal displacement Stokes coefficients, in practice, can fully represent the loading behaviour in the spectral domain due to the missing components discussed above. We recognize that this a weak point of this analysis of the spatial resolution discussion. This conclusion can also be found in Table 4.2, as the signal of the horizontal displacements are dominated by the low degrees.

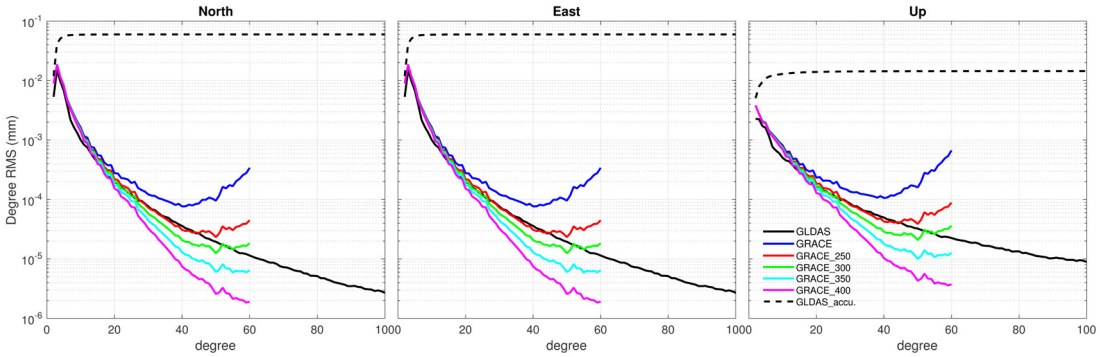

Figure 4.10: Global degree RMS spectra of the 3-D displacements (North, East and up components in the left, middle and right panels, respectively) from GLDAS (black) and GRACE gravity field (blue) with different Gaussian smoothing radius (250km, 300km, 350km and 400km in red, green, cyan and magenta, respectively). Dashed black lines represent the accumulated degree RMS obtained from GLDAS.

Table 4.2: Accumulated degree RMS in percent of the total displacements Stokes coefficient degree RMS from the GLDAS continental water storage variations.

Degree	Accumulated degree RMS (%)			Spatial resolution (km)
	N	E	U	
2	93.2	93.2	75.5	
24	99.9	99.9	97.6	~750
36	100.0	100.0	98.9	~500
72	100.0	100.0	99.8	~150

The accumulated degree RMS for the up component in Table 4.2 shows that up to 36 degree (~500 km spatial resolution on ground) of the spherical harmonics can restore about 99% of the displacement amplitude. Most of the major river basins are at this spatial resolution, except for some very large river basins such as Mississippi River and Amazon basins. For those river basins whose radii are below the 500 km, most (~99%) of the vertical loading signal can be restored.

4.2.4 An empirical basin averaging function

After the spatial resolution discussion above, one solution for minimizing the NFE is

implemented here by introducing an averaging function for each basin. Basin averaging functions are commonly applied in the mass studies at the basin scale using the GRACE time variable gravity field implementation (Baur et al., 2009; Huang et al., 2012; Landerer and Swenson, 2012; Rietbroek, 2014 among others), to reduce the leakage signal.

As we discussed in the Section 4.1, the surrounding loading signals are restored by extending the study region and introducing additional basins into the inversion system. The averaging function then can be introduced to reduce the NFE. The basin average, $\bar{m}$, can be computed by convolving the averaging kernel $w(\theta,\lambda)$ with the mass variations, $m(\theta,\lambda)$:

$$\bar{m} = \frac{\int_{\Omega} w(\theta,\lambda)\cdot m(\theta,\lambda)d\Omega}{\int_{\Omega} w(\theta,\lambda)d\Omega} \tag{4.8}$$

where Ω denotes the basin. Unlike the averaging function used in (Huang et al., 2012 among others), the averaging kernel is not larger than the area of the basin.

The empirical averaging kernel $w(\theta,\lambda)$ is derived from the available mass transportation models/data according to the RMS of the mass variation within the basin:

$$w(\theta,\lambda) = \frac{\mathrm{RMS}_{m(\theta,\lambda)}}{\overline{\mathrm{RMS}}_{m(\theta,\lambda)}} \tag{4.9}$$

where $(\theta,\lambda)\in\Omega$ and $\overline{\mathrm{RMS}}_{m(\theta,\lambda)}$ denotes the mean RMS of the CWS within the basin. $\mathrm{RMS}_{m(\theta,\lambda)}$ of the whole globe is presented in Figure 4.11 which is obtained from WaterGAP. The corresponding $w(\theta,\lambda)$ is shown in Figure 4.12 with the constraint that the kernel cannot be larger than two to avoid the basin mean being dominated by a small region.

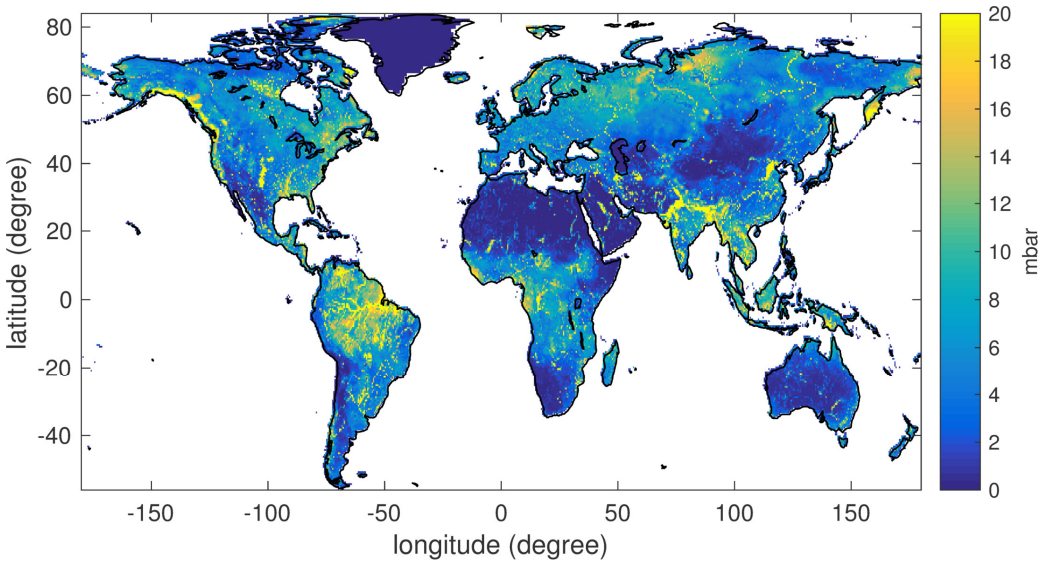

Figure 4.11: RMS of the globe CWS obtained from WaterGAP. Greenland region is excluded and the Greatbatch approach (Greatbatch, 1994) is implemented to remove the linear trend of the whole globe.

This empirical averaging kernel physically means that the location within the basin that does not show a strong mass variation is down weighted and locations with a strong mass variation is given more weighting. Due to the fact that the spatial distribution of the CWS is influenced by many environmental factors such as altitude, distance to the coast, temperature etc., the simple average over the basin cannot sufficiently represent the real distribution of the mass variations and this causes the discrepancies presented in Figure 4.9.

After applying the averaging kernel, the NFE (in terms of the RMS of the residuals and the correlations) are presented in Figure 4.13. Clear improvements for both the correlation and RMS around Amazon River basin and middle of Africa can be seen by comparing with NFE without the averaging kernel (Figure 4.9). After introducing the averaging kernel, the NFE is significantly reduced for all the components, see Table 4.3.

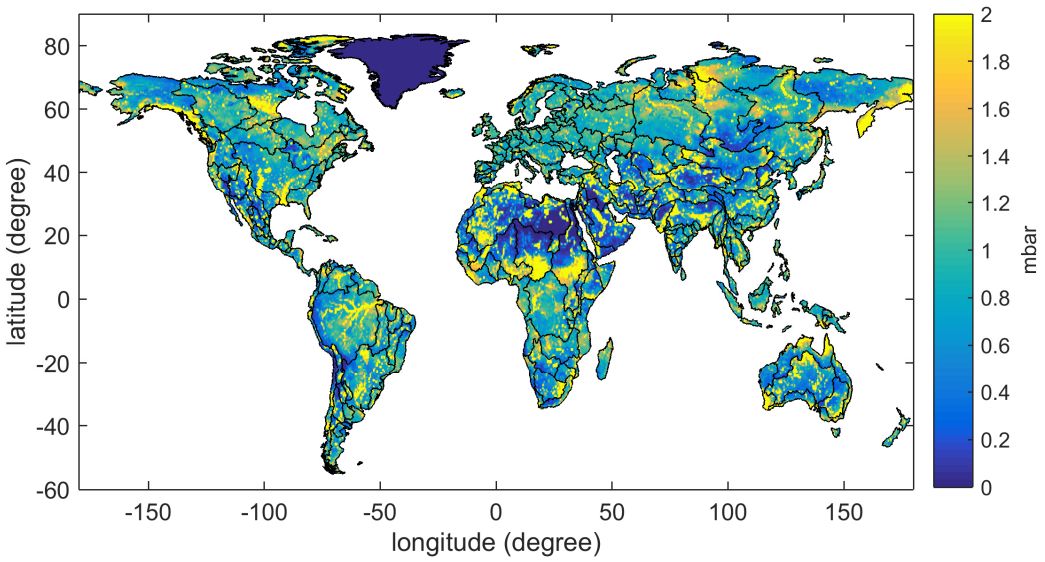

Figure 4.12: Basin averaging kernel for the global major river basins based on the RMS of the CWS.

Table 4.3: Statistics of the NFE and after applying averaging kernel with respect *to original displacements.*

comparison	components			Unit
	N	E	U	
$\overline{\mathrm{RMS}}(\varepsilon_{\bar{m}})$	0.164	0.156	0.855	mm
$\overline{\mathrm{RMS}}(\varepsilon_{\bar{m}\times w})$	0.141	0.136	0.715	mm
$\bar{\rho}(X_{\bar{m}}, X_m)$	0.881	0.792	0.936	-
$\bar{\rho}(X_{\bar{m}\times w}, X_m)$	0.911	0.843	0.943	-

The correlation for the vertical component in North Africa is reduced after employing the averaging kernel, due to the small displacement within this region. From this case study, it is obvious that, the horizontal displacements are more influenced by NFE as the error is more sensitive to displacements with a higher spatial resolution.

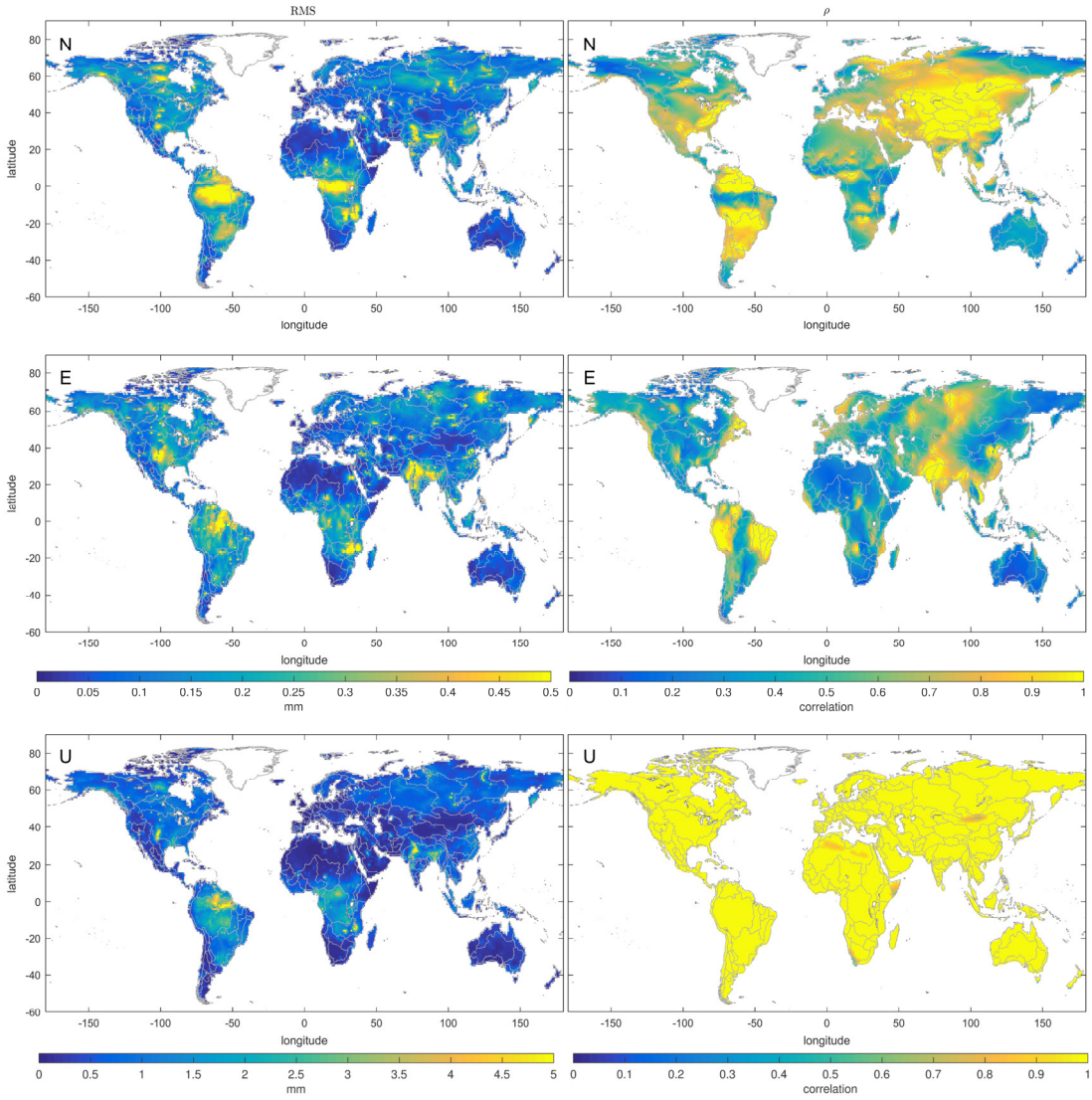

Figure 4.13: Near-field effect for unresolved mass variations within the major river basins after applying the averaging kernel. Right Panels: RMS of NFE for North (Top), East (Middle) and Up (Bottom) components in mm; Left Panels: correlation between the basin mean CWS induced motions and globally induced motions for North (Top), East (Middle) and Up (Bottom) components.

4.2.5 Conclusions

Solving for a basin mean variation in a regional inversion results in what we term the near-field effect in the displacements. The high spatial resolution of the mass variation signal is missing in the displacement time series. From the study in spectra domain, the displacement signals are dominated by the lower degree signal. However,

the horizontal displacements do not display the interior properties in the spectra domain. Omitting this near-field effect can cause significant error in the displacements (up to 0.5 mm and 5 mm for the horizontal and vertical displacements, respectively, for the region where massive mass variations are found).

For the vertical displacements study, major river basins that have a suitable spatial resolution (~500 km) can be resolved, as about 99 percent of the displacement amplitude is covered. The correlations of the vertical displacement derived from global mass variations and mean basin mass changes are close to 1, except for a few coastal regions.

One empirical averaging kernel obtained from the hydrological model is suggested from the case study, as NFE can be significantly reduced, see Table 4.3. This averaging kernel is calculated as the scale parameter around the basin that includes the high spatial resolution signal excluded by the mean basin variation.

Chapter 5. Discrepancies between GPS time series and modelled displacements

In this chapter, GPS observed displacements are compared with the continental water storage obtained from the hydrological models and GRACE time variable gravity field. The discrepancies between the GPS observation and reference sources are discussed in three parts: the behaviour of the discrepancies in the spatial and spectral domains, the possible cause of the discrepancies, and the re-estimated GPS observation quality based on the discrepancies.

5.1. Data descriptions

5.1.1 GPS time series

The 3-D GPS weekly time series from (2011), are reprocessed ITRF2008 residuals that preserve the non-linear crustal displacements, especially the seasonal variations. The seismic discontinuities within the time series have been removed (Collilieux et al., 2011).

GPS sites that have less than two years of weekly observations (less than 104 weeks) are excluded from the inter-comparison study to insure statistical significance. The GPS sites located on islands are also ignored as the displacements here are not dominated by the continental water storage variations. The GPS sites in Greenland and Antarctica are also excluded due to lack of data in the reference models or lack of quality. In summary, 344 GPS stations (red and green) out of 891 permanent GPS (all triangles) sites remain for inter-comparison and are shown in Figure 5.1.

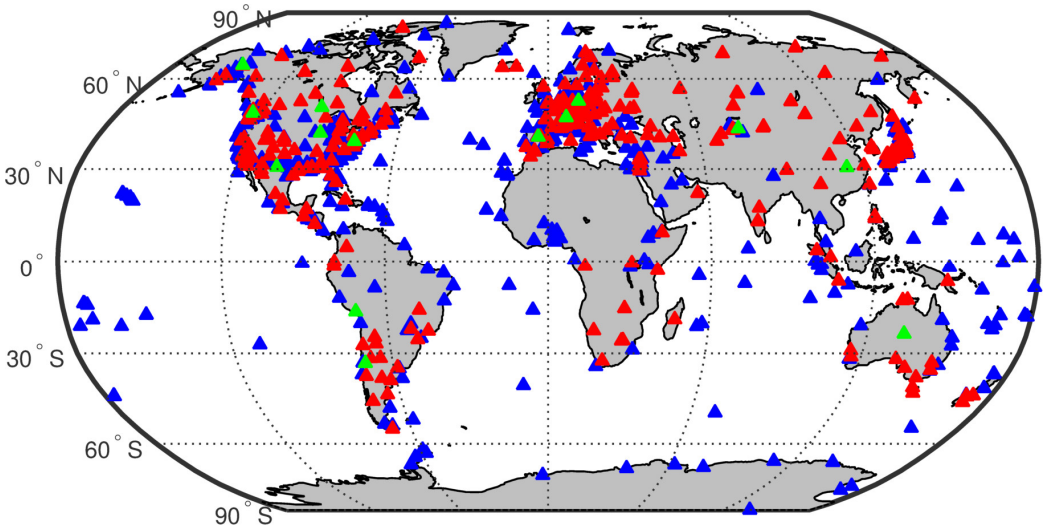

Figure 5.1: 891 GPS sites from the ITRF2008 provided from IGN (in triangles), 547 GPS sites have less than two years of observations or which are not located over the continental regions are excluded in comparison (in blue), 14 GPS time series plotted in Section 5.2 are mapped in Green triangles.

5.1.2 GRACE observed mass variations

The time variable gravity field observed by GRACE, has been providing a global view of the water storage variations, since its launch on the March 17, 2002. GRACE observations have been the subject of various water storage publications, such as glacial melting (Velicogna and Wahr, 2005, 2013; Velicogna, 2009), groundwater depletion (Rodell et al., 2009; Famiglietti et al., 2011; Muskett and Romanovsky, 2011; Huang et al., 2012), extreme hydrological events (Reager and Famiglietti, 2009; Chen et al., 2010; Steckler et al., 2010; Houborg et al., 2012; Li et al., 2012; Long et al., 2013; Thomas et al., 2014) and more. The mass variations observed by GRACE mission provides an independent way to examine the mass loading displacements at the GPS sites.

CSR Rel05 level-2 product is chosen for this inter-comparison. Besides the CSR product, JPL and GFZ also provide solutions. According to Sakumura et al. (2014), the discrepancies between different solutions lie within the error bounds of the GRACE solutions themselves. CSR Rel05 is sufficient to perform as the reference

gravity field solution rather than an averaging over different products.

A standard approach for preparing the GRACE time variable gravity field is applied. The degree-1 coefficients are added from Swenson et al. (2008). C_{20} coefficients are replaced by SLR observations (Cheng and Tapley, 2005). The de-striping filter is applied and obtained from Swenson and Wahr (2006). Gaussian smoothing with a filter width of 250 km radius in spectral domain is implemented in order to suppress the short wavelength noise, and to preserve the small-scale mass variations (Wouters et al., 2008). Before calculating the displacements, the mean field of the Stokes coefficient is removed.

After the preprocessing, the 3-D displacements of the Earth's surface can be obtained from Eq. (2.22). The GRACE mission orbits around the Earth's center of mass and naturally exists in the Center of Mass (CM) reference frame. After replacing the degree-1 coefficient (Swenson et al., 2008), the GRACE gravity field lies in the Center of Earth (CE) reference frame. Thus, the displacements obtained from GRACE are transferred from CE to the Center of Figure (CF) reference frame in order to be consistent with the GPS observations. Transformations over different reference frames are essentially adjusted using the degree one term (Blewitt, 2003):

$$\begin{bmatrix} h_1 \\ l_1 \\ k_1 \end{bmatrix}_{CF} = \begin{bmatrix} \frac{2}{3}(h_1 - l_1) \\ -\frac{1}{3}(h_1 - l_1) \\ -\frac{1}{3}h_1 - \frac{2}{3}l_1 \end{bmatrix}_{CE} \tag{5.1}$$

where CE and CF denotes the load Love number in CE and CF reference frame, respectively.

5.1.3 Other environmental induced loading displacements

In order to avoid the external influences on the un-modelled displacement, the environmental loading other than the CWS are removed from the GPS observations.

Atmospheric loading

The atmosphere covers the entire Earth's surface. Variations in atmospheric mass load and deform the Earth's crust. The monthly atmospheric loading (ATML) is forward modelled using pressures provided by the National Center for Environmental Prediction (NCEP)/National Center for Atmospheric Research (NCAR) (Kalnay et al., 1996).

Nontidal Ocean loading

GPS observed displacements include the effect of mass variations over oceans. The mass variations over the ocean are composed of the tidal and non-tidal ocean mass changes. These mass variations load the Earth's surface and induce displacements. Tidal ocean loading is normally removed at the observation level processing and will not be discussed further here. The non-tidal component is based on ocean bottom pressure from the Circulation and Climate of the Ocean (ECCO) (Fukumori, 2002; Kim et al., 2007), and it is the same dataset used in (2012).

5.2. Inter-comparison between displacements from GPS and reference sources

The GPS time series can be considered as independent observations of the environmental loading displacements. In order to understand the GPS time series as the displacement observations, inter-comparison between the displacements obtained from GPS and the models is performed here. 344 GPS sites over the continents are selected for the comparison. These are stations having more than two years of data and are not located on islands.

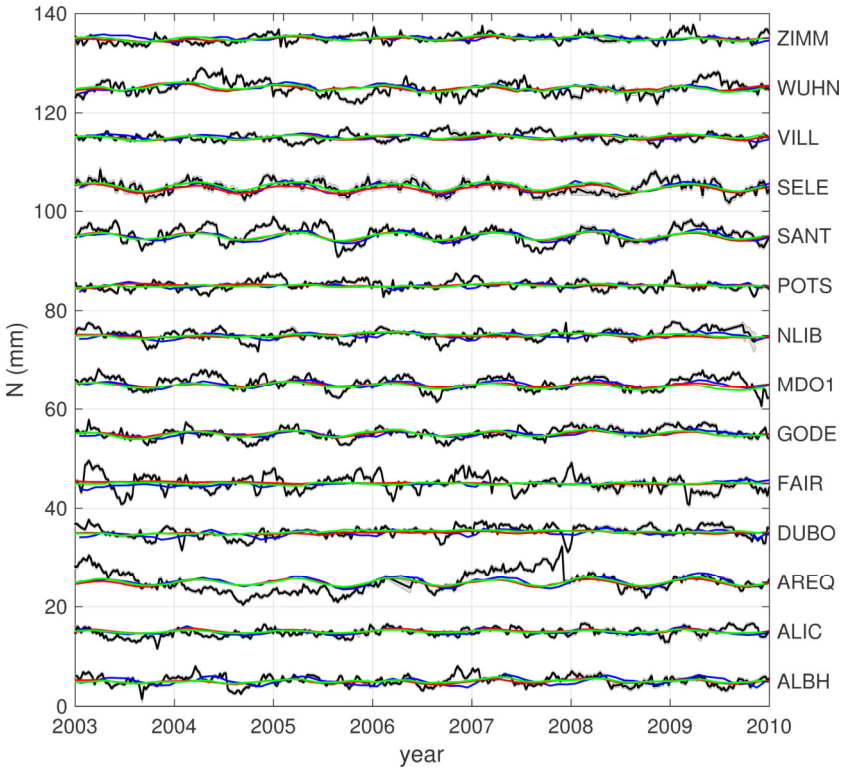

Figure 5.2: Exemplary GPS time series (black) in north direction overlapping with the forward modelled North displacements obtained from GRACE (blue), GLDAS (red) and WaterGAP (green). The corresponding GPS station names can be found on the right side of the figure. The GPS one sigma error is shown in grey. Legends are in Figure 5.4. Note that the time series are shifted for better visualization.

Fourteen exemplary GPS sites are selected out of 44 in total which have more than 12 years of observations overlapping with the displacements obtained from the GRACE and hydrological models. They are shown in Figure 5.2, Figure 5.3 and Figure 5.4 in north, east and up directions, respectively. The distribution of the GPS sites is shown by the Green triangles in Figure 5.1. The GPS displacements from ZIMM, POTS, NLIB, GODE, DUBO, AREQ and ALBH show a close match with the forward modelled displacements using GLDAS, WaterGAP, and GRACE. The other sites show more moderate matches. The peak-to-peak vertical amplitude is at the 1-2 cm level. The amplitudes of the horizontal displacements in GPS are about one third the vertical displacements. Moreover, the horizontal displacements obtained from GRACE and hydrological model are smaller than those from GPS.

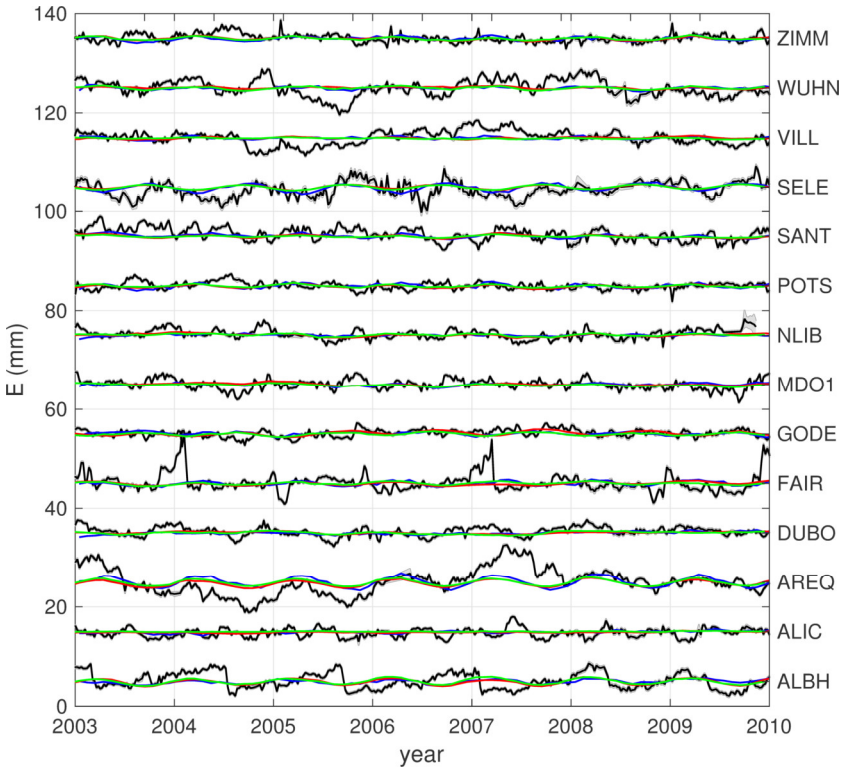

Figure 5.3: Exemplary GPS time series (black) in East direction.

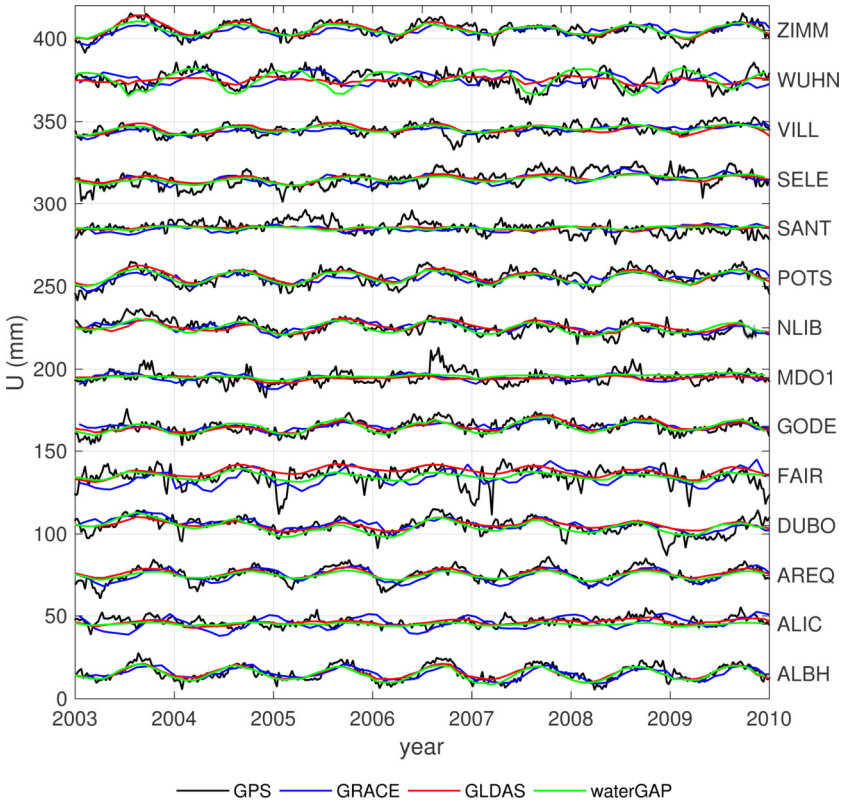

Figure 5.4: Exemplary GPS time series (black) in Up direction.

5.2.1 Statistical evaluation metrics of the inter-comparison

In order to statistically evaluate the inter-comparison of the displacement, the metrics are evaluated in terms of the correlations, Weighted Root Mean Squares (WRMS), WRMS reduction (WRMSR) and WRMS ratio (van Dam et al., 2007; Jiang et al., 2013). The displacement time series obtained from the reference sources are resampled from monthly to weekly. Then these interpolated displacements are compared with the GPS observations.

Correlation

Correlation is the statistical linear dependence between two time-series. It is defined as

$$\rho(X_1, X_2) = \frac{\sum_{i=1}^{n}[X_1(t_i) - \overline{X}_1][X_2(t_i) - \overline{X}_2]}{\sqrt{\sum_{i=1}^{n}[X_1(t_i) - \overline{X}_1]}\sqrt{\sum_{i=1}^{n}[X_2(t_i) - \overline{X}_2]}}\ , \tag{5.2}$$

where $X \in [X^N, X^E, X^U]$ and $X = [X(t_1), X(t_2), \ldots, X(t_n)]$. The correlation between two, time series shows the phase differences, and it is not sensitive to the amplitude differences between the time series. The agreement in amplitude is evaluated by using metrics that will be discussed in the next section.

WRMS and WRMSR

WRMS of the time series indicates the signal amplitude, obtained by

$$\mathrm{WRMS}(X) = \sqrt{\frac{\sum_{i=1}^{i=N} w_i X_i^2}{\sum_{i=1}^{i=N} w_i}}\ , \tag{5.3}$$

where w_i is the weight and it is inverted from the variances of the observations, as $w_i = 1/\sigma_i^2$. σ_i is the standard deviation. For the reference datasets and models, WRMS is the same as RMS when the standard deviations of the models are not available.

If the modelled displacements contain real signal, then removing a forward model

from the observations may reduce the WRMS. Then the percentage of WRMSR at one particular site is a function of the WRMS of the two, time series being compared as

$$\mathrm{WRMSR}(X_{GPS}, X_{ref}) = \frac{\mathrm{WRMS}(X_{GPS}) - \mathrm{WRMS}(X_{GPS} - X_{ref})}{\mathrm{WRMS}(X_{GPS})} \times 100\% . \quad (5.4)$$

The WRMSR measures the deviations of the phase and amplitude deviations between two, time series. The higher WRMSR means two, time series are similar. The uncertainty information from GRACE is excluded in the inter-comparison for two reasons: the objective of this study is to understand the GPS time series and the uncertainties in the GPS data; remain the consistencies between the inter-comparisons (GPS with GRACE and GPS with hydrological models). The error on the hydrological models are not available. Introducing the error information from GRACE results in inconsistency while comparing with the result with hydrological models. This is formally improper for the error propagation, but commonly adopted in similar inter-comparison studies (van Dam et al., 2007; Tesmer et al., 2011; Jiang et al., 2013).

WRMS ratio

In order to understand the signal quality of the GPS observations, a comparison between the amplitude of the signal is performed as obtaining the WRMS ratio between the GPS time series and displacements derived from the reference sources:

$$ratio_{\mathrm{WRMS}} = \frac{\mathrm{WRMS}(X_{GPS})}{\mathrm{WRMS}(X_{ref.})} . \quad (5.5)$$

This WRMS ratio, $ratio_{\mathrm{WRMS}}$, presents the amplitude ratio between the displacements from GPS and the reference sources. If the displacements obtained from the reference sources are perfect and GPS is error free, then the ratio will be equal to one.

5.2.2 Comparisons in temporal domain

After the data preparation described in the former sections, the GPS displacements are compared with the displacements from the reference sources at GPS sites around the globe. For all 344 stations, the spatial distribution of the WRMSR is plotted in Figure 5.5 (Please note the scale differences between the horizontal and vertical directions). The positive WRMSR (in warm colors) shows that the WRMS was reduced after subtracting the forward modelled displacements from the GPS observations.

Figure 5.5 shows the spatial distribution of the displacements compared in the temporal domain for the three coordinates. If the CWS induced displacement is perfect at representing the displacements and the GPS observations observed the true CWS signal, then all the WRMSR circles in this figure should be red with an amplitude of 100%. The right column presents comparison of the WRMSR for vertical coordinate. The majority of the stations (154, 68.9% for GRACE; 232, 87.1% for GLDAS and 244, 88% for WaterGAP, out of 344 stations) have their WRMS reduced. The remaining stations (WRMSR are negative) are mostly located in coastal regions where the CWS loading displacements are smaller than those further inland. WaterGAP reduces the WRMS on the greatest number of GPS sites, and from the histogram, WaterGAP performs best.

The WRMSR of the horizontal components are shown in the left (north) and middle (East) columns. In the north direction, the WRMS is reduced on 46.1%, 69.5% and 73.1% of the GPS time series using GRACE, GLDAS and WaterGAP, respectively. Let's look at the stations where the WRMS is not reduced for the WaterGAP comparison (left bottom panel in Figure 5.5). Certainly, some patterns can be observed over those stations, which are located in coastal regions and in Western Europe.

The discrepancies in the north component of the GRACE comparison are bigger than the discrepancy with the hydrological models. Less than half of the stations

have a positive WRMSR when GRACE is removed. The WRMS increases after subtracting GRACE in North America for most of the GPS sites located at latitudes greater than 40 degrees. From the left panels in Figure 5.7, it is obvious that WaterGAP is more clustering on the positive axis which meaning larger WRMSR and higher correlations. This indicates WaterGAP performs the best among the comparisons in the north direction.

In the East, fewer stations have their WRMS reduced after removing the forward modelled displacements from GPS, only 41.6%, 51.5% and 55.1% for GRACE, GLDAS and WaterGAP. The distribution of the increased WRMS sites are fewer than the comparison in vertical and north directions. The hydrological models again perform better than GRACE.

From the comparison results, the vertical displacements are consistent match between the GPS observations and displacements obtained from reference sources. Up to 88% of the GPS time series have their WRMS reduced after subtracting the WaterGAP modelled loads. This is not the case for the horizontal displacements.

$ratio_{\mathrm{WRMS}}$ is shown in Figure 5.9 with the a similar arrangement as in Figure 5.5. The corresponding histograms are presented in Figure 5.8. In contrast of the WRMSR comparison results, the WRMS ratio shows that GRACE has a better performance among the reference sources in all the three components. The amplitudes of the GRACE induced displacements are closer to the GPS observations than those of the hydrological models. For the coastal regions, the mass loading induced displacements are smaller than for the stations located inland with the same equivalent water height (EWH). Then the displacements from hydrological models, especially the vertical displacements are smaller than the GPS observations. This leads to a bigger WRMS ratio, e.g. Japan and the coast around Australia.

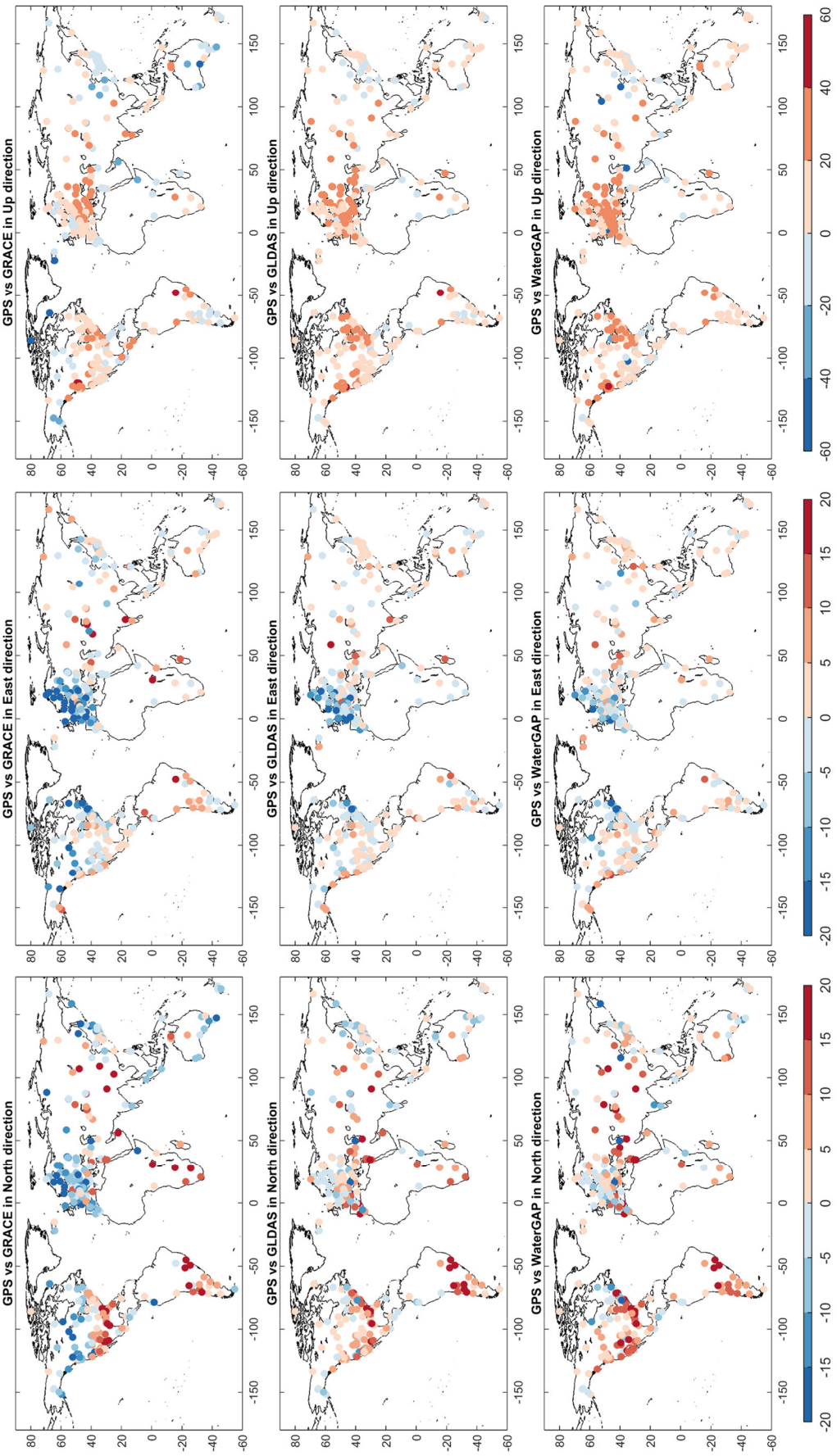

Figure 5.5: Spatial distributions of the WRMSR in percentage for the three reference CWS loads. The colour bars at the bottoms represent the colour axes of each direction.

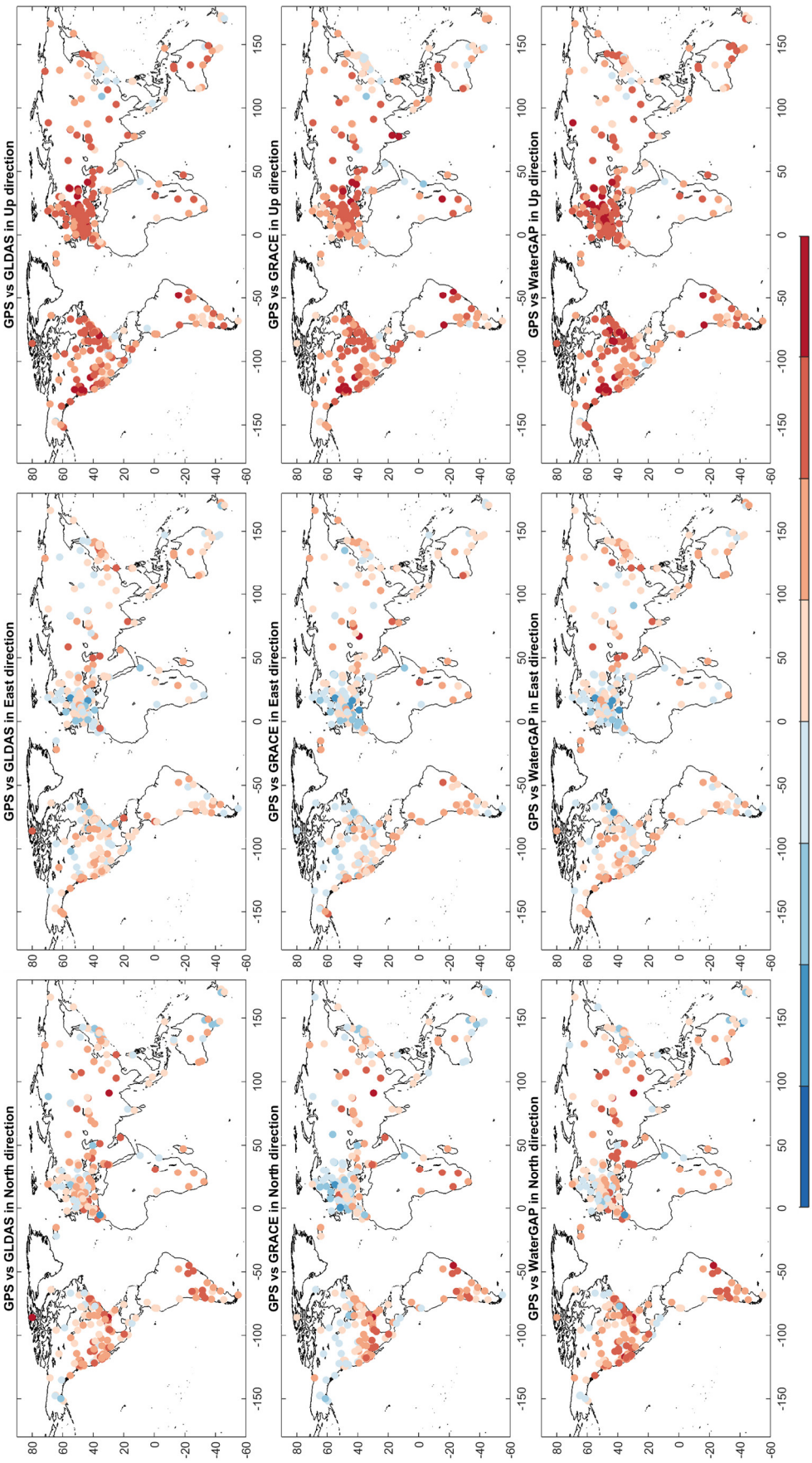

Figure 5.6: Spatial distribution of correlations between GPS and CWS obtained from GRACE, GLDAS and WaterGAP in the first, second and last rows, respectively.P

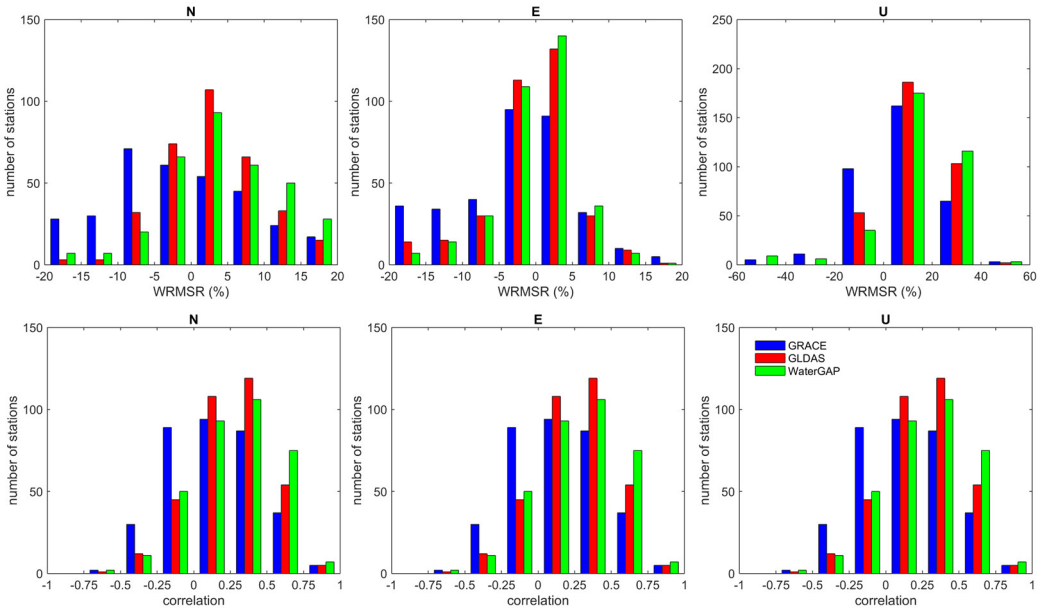

Figure 5.7: Histogram of the WRMSR and correlation coefficients for the 344 GPS sites between the GPS observations and the forward modelled displacements from GRACE, GLDAS and WaterGAP.

For the north and vertical components, the amplitudes of the displacements from GPS and GRACE are more similar than those in the east. From Figure 5.8, it is obvious that the majority of the GPS sites have WRMS ratio larger than 2 for both GRACE and hydrological models. Thus, the signal content in the east direction might be dominated by other signal or errors rather than the displacements induced by the water storage.

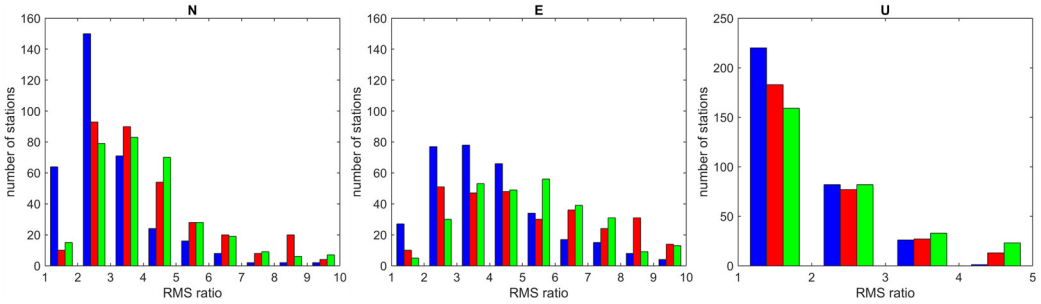

Figure 5.8: RMS ratio histograms of the GPS versus the GRACE, GLDAS and WaterGAP for the three directions.

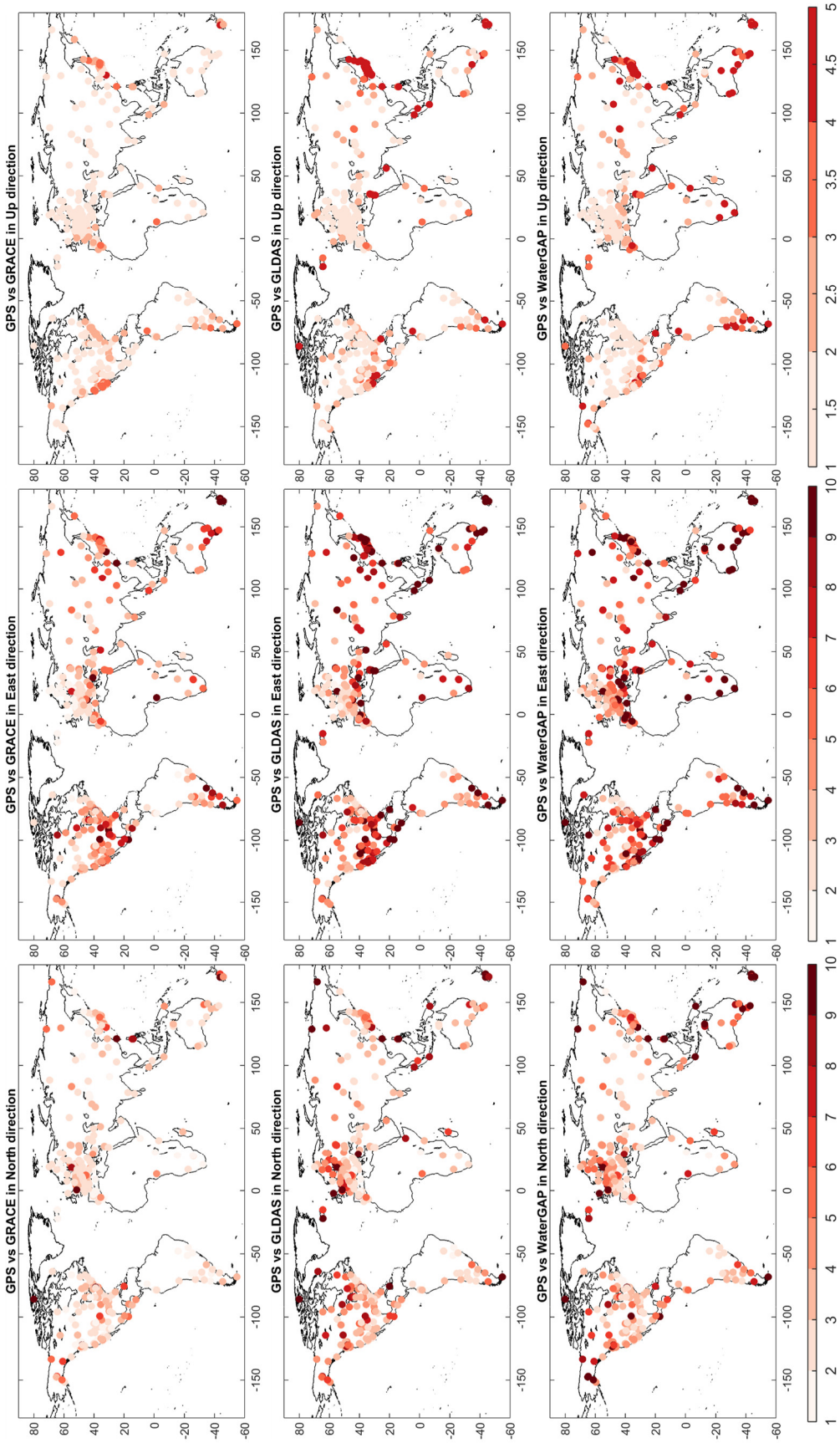

Figure 5.9: The RMS ratios between the GPS displacements and displacements obtained GRACE, GLDAS and WaterGAP in the first, second and last rows, respectively.

5.2.3 Comparison in spectra domain

In order to understand the signal content within the time series, looking at the time series in the frequency domain is a common way to analyse the error and signal content (Williams, 2004; Amiri-Simkooei, 2013). In this section, we compare the displacements in the spectral domain. The CWS time series are dominated by the seasonal, semi-annual and long-term variations(Dong et al., 2002; van Dam et al., 2007; Tesmer et al., 2011). Recently, an anomalous harmonic of 1.04 years (351.4 days) and its higher order harmonics was revealed in the GPS observations (Collilieux et al., 2007; Ray et al., 2008; Tregoning and Watson, 2009). This frequency coincides with the GPS constellation and is named as GPS draconitic frequencies.

GPS observations and the displacements obtained from the reference sources are presented in Lomb-Scargle periodogram (Lomb, 1976) as an amplitude spectra with units of a millimeter. The amplitude spectra of the displacements over the 344 GPS sites are stacked and plotted in Figure 5.10 along with the displacements obtained from reference sources. The amplitudes of the GPS observations are generally larger than the amplitudes from GRACE, GLDAS, and WaterGAP, except for the annual signals in the vertical displacements.

With the illustration of all the amplitude spectra, it is clear that GRACE and the hydrological models are consistent in their signal content for frequencies smaller than two cycles per year (cpy). When comparing GRACE to the CWS variations, we find that GRACE observes the same amplitude. The amplitude spectrum of GRACE fluctuates around 0.04, 0.03 and 0.3 mm in the north, east and up directions, respectively, for frequencies larger than two cpy. The GRACE amplitude curves are relatively flat indicating the GRACE noise level. Amplitude spectrum curves from GPS show peaks around the draconitic frequencies and gradually decease.

The vertical GPS amplitude spectrum is generally larger than the amplitude of the displacements derived from GRACE. But for the high frequencies, the amplitudes of

the displacements from GPS and GRACE are closer to each other, especially after 3.5 cpy. The amplitudes of the annual signal from GPS and GRACE match very well. In contrast to the vertical amplitude spectrum, the horizontal spectra, especially in the east, the amplitudes of the GPS time series are about one order of magnitude larger than the GRACE time series.

The displacements obtained from the CWS of the reference sources has a lower amplitude with respect to GPS time series for the whole spectrum. This can be explained from the GPS noise. As the amplitude of the annual signal in vertical direction are very close to that derived from GRACE and the annual signals are the largest signal in the time series. Unlike the annual and semi-annual frequency, the signal in GPS are within the level of the GPS error. The WRMS ratio comparison in Figure 5.8 also confirmed that GPS time series have larger amplitudes with respect to reference sources, especially for the horizontal displacements. And the noise level of the horizontal GPS time series is close to the annual signal strength derived from the reference source.

The CWS model displacements are subtracted from the GPS observations and the corresponding amplitude spectra are presented in Figure 5.11. The original GPS amplitude spectra are plotted in black.

For the vertical GPS displacements, the GPS annual amplitudes are reduced to 2.3, 2.0, and 1.9 mm from original 3.7 mm after subtracting the displacements from GRACE, GLDAS and WaterGAP, respectively. Thus 40-50% of the GPS observed vertical displacement can be explained by the CWS variations.

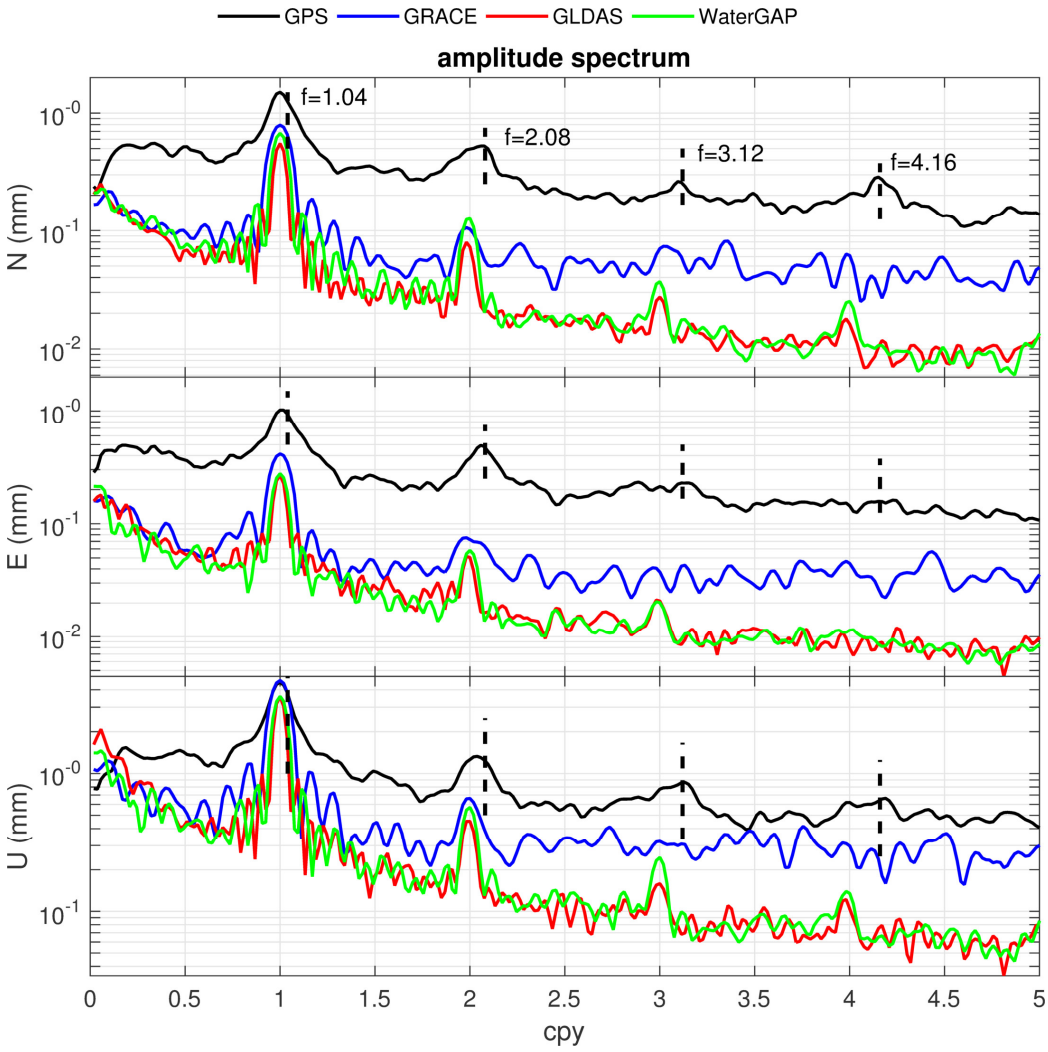

Figure 5.10: The stacked amplitude spectrum of the displacement time series at the GPS sites obtained from GPS (black), GRACE (blue), GLDAS (red) and WaterGAP (green). The black dash lines indicate the draconitic frequencies.

Conversely, no significant reduction can be found in horizontal displacements. In the north direction, after subtracting the forward modelled displacements, the annual amplitudes are reduced to 1.4, 1.3 and 1.3 mm from 1.4 mm. This reduction is not statistically significant. The reduction is not clear in the east component. In fact, after subtracting WaterGAP, the amplitude of the annual signal is increased.

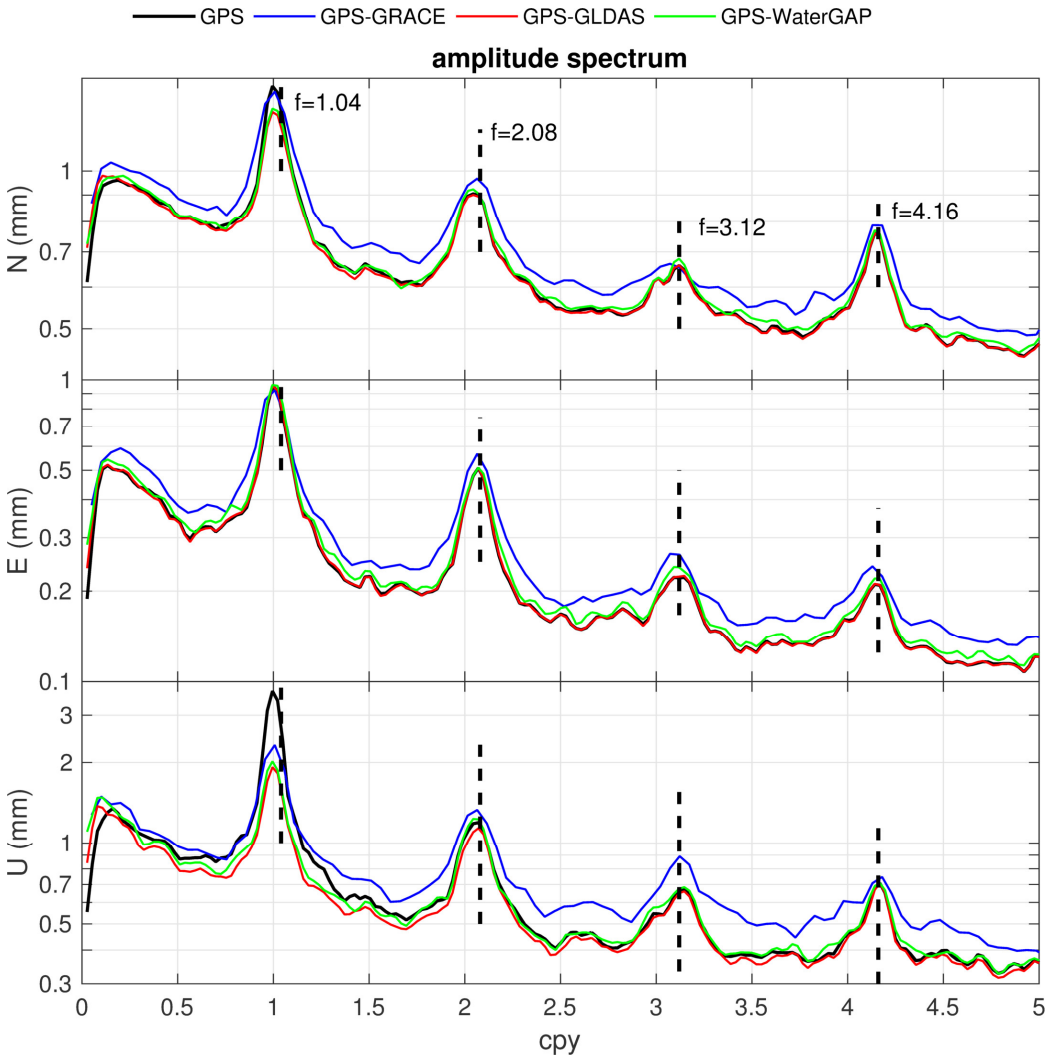

Figure 5.11: Stacked amplitude spectra of the GPS displacements after removing the displacements forward modelled by GRACE (blue), GLDAS (red) and WaterGAP (green). The spectra of the original GPS time series are plotted in black lines. The black dash lines indicate the draconitic frequencies.

For the other frequency range, after removing GRACE, the amplitude spectrum is increased. This is possibly due to the error of these independent observations, GPS and GRACE, is combined together. Similar effects are not found after subtractions of hydrological models from GPS time series.

5.2.4 The possible causes of the discrepancies

We have shown the discrepancies between the GPS and reference sources. Any of

a number of non-geophysical factors could introduce those discrepancies including the tropospheric delay (Schüler, 2001), monument thermal expansion (Yan et al., 2009), bedrock thermal expansion (Dong et al., 2002; Fang et al., 2014), phase center mismodelling (Schmid and Rothacher, 2003; Schmid et al., 2007), GPS constellation (Ray et al., 2008) etc.

Local mass loading signals have been considered as another suspected discrepancy sources (Dong et al., 2002; van Dam et al., 2007; Flouzat et al., 2009; Tesmer et al., 2011). But from the simulation study from van Dam et al. (2007), they conclude that the local signal CWS is the main source of the discrepancy.

Dong et al. (2002) summarized all the possible discrepancies sources and found that environmental loading can explain about 40% of the vertical displacements, bedrock thermal expansion can account for ~0.5 mm of the displacements. Yan et al. (2009) extended the study of (Dong et al., 2002) and found the thermal vertical displacements including the bedrock and monument displacements are generally smaller than 2 mm, with maximum displacements of 3.9 mm. Fang et al. (2014) further extended the study of (Dong et al., 2002; Yan et al., 2009) and obtained the global thermal displacements in three directions with ~2 mm for radial expansion and ~1 mm for transverse displacements.

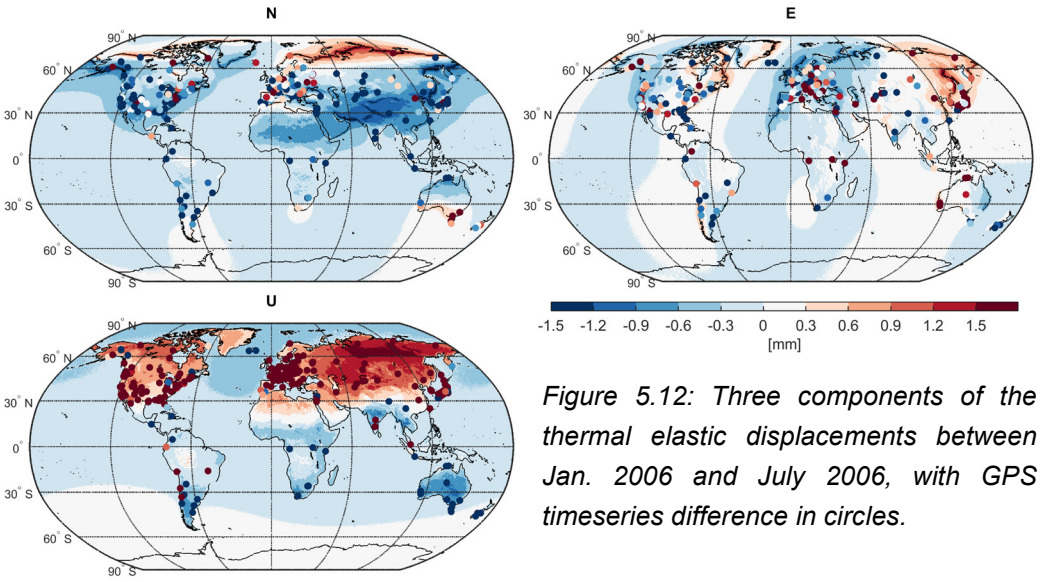

Figure 5.12: Three components of the thermal elastic displacements between Jan. 2006 and July 2006, with GPS timeseries difference in circles.

In this section, the thermal expansion displacements, plotted in Figure 5.12, are taken from (Fang et al., 2014) for the monthly temperature differences between January 2006 and July 2006. The thermal expansions at the GPS sites are bi-linearly interpolated from the global thermal expansion field. As the thermal expansions are driven by the temperature variations, the consistencies in the Figure 5.13 can be found as temperature in the northern hemisphere is higher, the vertical expansions are positive in the northern hemisphere. At the same time, the mass loads in the summer time in northern hemisphere are smaller, thus, uplifts are also driven by these mass loads. This could partly explain why GPS observes larger displacements than those sensed by GRACE. Consistency between GPS and thermal expansion can be found in the vertical and north components. In the east direction, the thermal expansions are smaller, the amplitudes of mostly continental regions are smaller than 0.3 mm (within -0.6 to -0.3 mm level in West Europe), neither the amplitude nor the sign have a consistent match between the GPS displacements and the thermal expansions, due to the small amplitudes of the thermal expansions.

Another comparison following the discussion in (Davis et al., 2004; Hao et al., 2016) presents the GPS observed displacements and the modelled displacements between January 2006 and July 2006 in Figure 5.13. The regressed ratios between

GPS and modelled displacements are presented as dashed lines in the corresponding color. As a reference, the unit slope is presented as grey dashed lines. This plot is commonly used for comparing the annual amplitude of the different observations, here it is extended to the comparison of whole signal content. Naturally, the comparison results are not as good as comparing the annual signal, as the noise is filtered out by deriving the annual signals. In this study, our objective is to understand the GPS noise and the discrepancies between GPS and modelled displacements. Thus, the original signals are used rather than only implemented at the annual period.

In Figure 5.13, the estimated vertical linear ratios are 0.42, 0.28, 0.32 and 0.05 for GRACE, GLDAS, WaterGAP and thermal expansions, respectively. The vertical ratios are well distributed along the ratio lines, especially the thermal expansions, although the amplitude of the thermal expansion (-1 mm to 2mm) is much smaller than the GPS observations (-1cm to 2 cm). In the north direction, the ratios of all the modelled displacements are around 0.1. Among all the modelled displacements, WaterGAP ratio is the highest (0.14) and GRACE ratio is the lowest (0.10). Thus, the modelled displacements can represent a small portion of the total GPS observations which corresponds to ~10%. In the east direction, the distribution is very scattered for all the modelled displacements and no promising ratio can be derived.

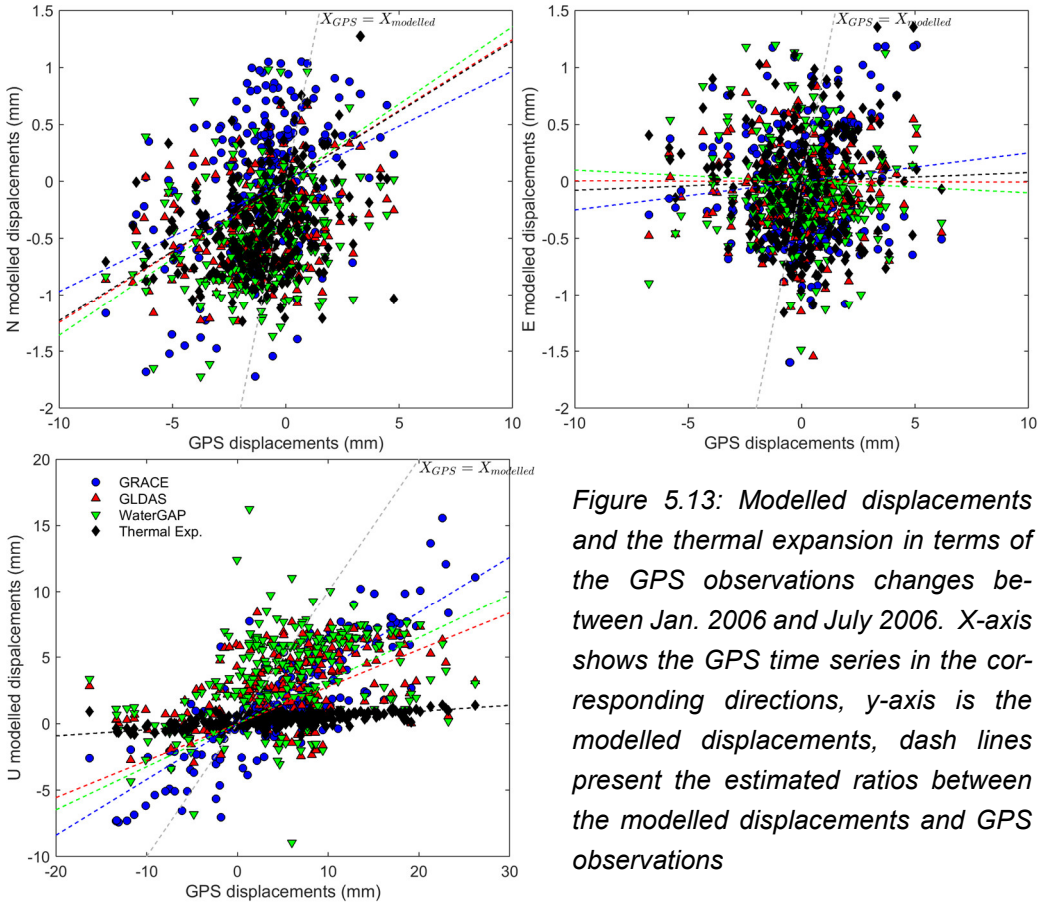

Figure 5.13: Modelled displacements and the thermal expansion in terms of the GPS observations changes between Jan. 2006 and July 2006. X-axis shows the GPS time series in the corresponding directions, y-axis is the modelled displacements, dash lines present the estimated ratios between the modelled displacements and GPS observations

From all the comparison studies presented above, it is obvious that the thermal expansion can be excluded as a main source of the discrepancies. Although consistent improvement can be presented in vertical GPS observations if removing the thermal expansion, but the amplitude of the thermal expansion (mm level) is far smaller than the discrepancies (cm level).

From the inter-comparison presented in Figure 5.5, Figure 5.8, Figure 5.10 and Figure 5.13, it is obvious that the displacements modelled from GRACE, GLDAS and WaterGAP are consistent with one another, though GRACE and WaterGAP agree better with the GPS time series. The discrepancies among the GPS and modelled displacements are much larger than discrepancies between the modelled displacements. This also indicates that the discrepancies seem to come from the GPS observations or the processing techniques, especially in the horizontal.

5.2.5 Re-estimate uncertainties of the GPS observed displacements

Before the discussion, we would like to clarify two definitions: GPS uncertainties and GPS uncertainties for loading studies. GPS uncertainties provided in GPS time series represent the quality of the GPS observations. But it is not necessary standing for the quality for the use of the loading studies as we assume all the GPS time series come from the mass redistributions. In fact, the motions observed in GPS time series can be caused by other effects.

The discrepancies between the GPS and modelled displacements are discussed in the last two sections. From the illustrated uncertainties in the Figure 5.2, Figure 5.3 and Figure 5.4, the uncertainties in the GPS time series account for the discrepancies between the GPS observations and modelled displacements. Thus, the GPS uncertainties for the loading studies need to be re-estimated for the loading studies.

GPS has long been used as an independent sensor for mass loading displacements (van Dam and Wahr, 1987; van Dam et al., 2001; Blewitt, 2003). Recently, research has demonstrated that GPS can be used to infer the continental water storage (Wu, 2003; Wahr et al., 2013; Amos et al., 2014; Fu et al., 2015). But up to recently, the uncertainties for using the GPS time series for inferring the water storage has not been fully understood. Although many studies focus on the GPS time series error sources and amplitudes (Williams, 2004; Cohenour and Van Graas, 2011; Griffiths and Ray, 2013), errors in the GPS measurements differ from the errors in the continental water storage study.

In the study comparing GPS time series to the load variations, the displacements observed in the GPS time series are assumed to represent the displacements derived from the true mass load changes plus the observation errors. Thus, direct use of GPS uncertainties is not proper for this purpose of study, as the GPS uncertainties in the time series measures the uncertainties of the GPS time series rather than

mass loading induced displacements. From the comparison of the former sections, it is obvious that GPS observes more than the signal of loading displacements, such as the thermal expansions. Amplitudes of the discrepancies between GPS and modelled displacements are larger than the uncertainties presented in the GPS time series, while displacements derived from different models and GRACE observations are consistent. To prevent over-estimating the CWS uncertainties, the GPS uncertainties need to be re-estimated.

344 GPS stations over the globe are selected as showed in Figure 5.1. After removing the annual, semi-annual and linear trend, the residuals in the displacements are considered to be errors in the GPS technique or unmodeled signal, as the CWS signal mainly consists of signal at these frequencies. First, we tried to analyzing the GPS uncertainties from the commonly used time series analysis software, CATS (Williams, 2004) and Hector (Bos et al., 2013). The results are not stable for all the GPS sites. This result is due to only a few GPS sites (44 stations) of all GPS time series used in our study have long observation time series (longer than 12 years). Thus, we estimate the errors from forward time series simulator.

GPS errors are station dependent, and from the previous studies we know that the GPS errors are pink and mainly consist of white noise, flicker noise, and random walk (Williams, 2004; Amiri-Simkooei et al., 2007; Teunissen and Amiri-Simkooei, 2008; Bos et al., 2013). Power-law noise is simulated based on (Williams, 2003) for the white noise standard deviation up to 5 mm, flicker, and random walk noise up to 3 mm. The original GPS uncertainties are below 1 mm for horizontal displacements and below 5 mm for verticals. Then GPS residuals are compared with the simulated error in the spectral domain after square spectral analysis (Lomb, 1976). Then the sum of the differences squared are obtained and presented in Figure 5.14.

In Figure 5.14, the illustrated surfaces present the equivalent square sum of the differences. The minimum square sum represents the best fit of the error model with

the GPS residuals. For the north and east directions, the minimums appear at the $(\sigma_{f=0},\sigma_{f=-1},\sigma_{f=-2})_N \rightarrow (0.7,2.9,0.1)$ and $(\sigma_{f=0},\sigma_{f=-1},\sigma_{f=-2})_E \rightarrow (0.6,3,0.3)$, where f = 0, -1 and -2 correspond to the white, flicker, and random walk noise, respectively. The vertical deviations are not conserved within the estimation range.

As the inversion method that we use here is based on the Gaussian error behaviour, this is a caveat of this inversion study. Then the GPS error is estimated based on the standard deviation of the discrepancies between the GPS time series and the forward modelled displacements for the horizontal direction. The vertical uncertainties of the GPS observation are increased five times to match the discrepancies in amplitude between GPS observations and modelled displacements.

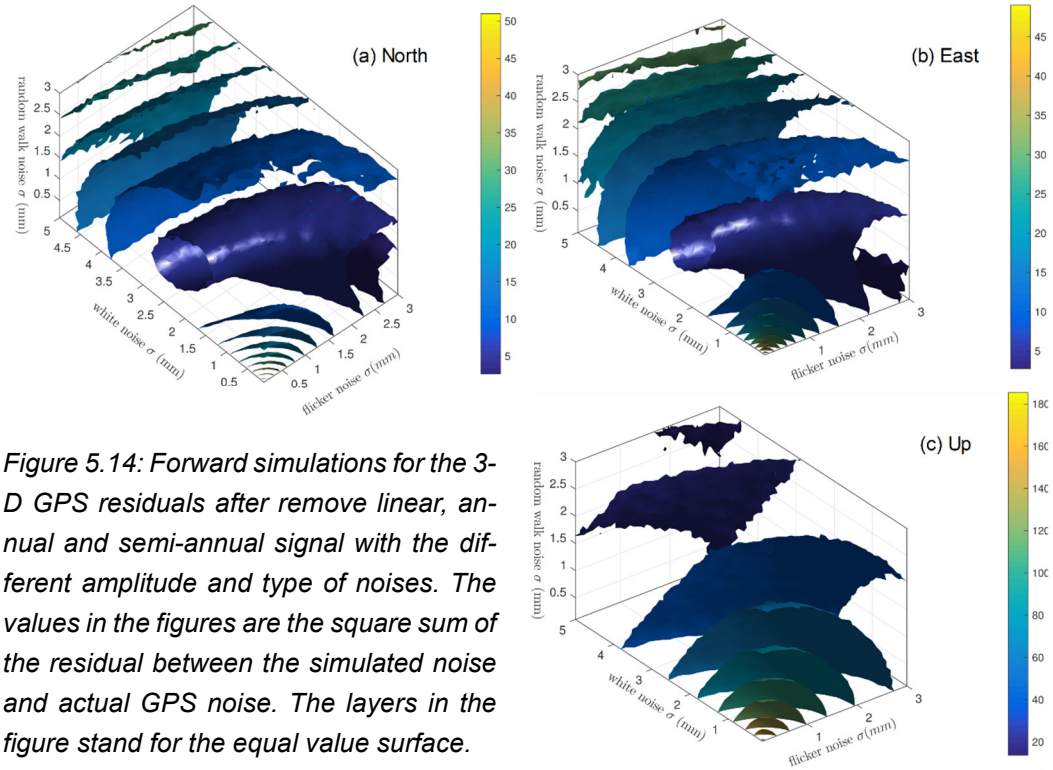

Figure 5.14: Forward simulations for the 3-D GPS residuals after remove linear, annual and semi-annual signal with the different amplitude and type of noises. The values in the figures are the square sum of the residual between the simulated noise and actual GPS noise. The layers in the figure stand for the equal value surface.

5.3. Conclusions

In this chapter, we investigated the CWS variation induced displacement observed

by the GPS and derived from GRACE and hydrological models, in order to understand the GPS signal content and its quality for determining CWS. The GPS time series and modelled displacements are compared in time and spectral domains, later the possible source of the discrepancies is discussed. The distribution of the discrepancies in spatial and spectral domains show that the main source of disagreement between the observations and the forward modelled surface displacements is not from the unresolved signal missing in the displacements (such as thermal expansion, local effect). The possible cause of the discrepancies is the error in GPS time series, such as the draconitic signals due to the GPS constellation, or from the GPS observation quality, especially for the horizontal displacements.

For the vertical displacements, 40% -50% of the GPS observation amplitudes can be explained by the CWS loading derived displacements. By subtracting the modelled displacements modelled using WaterGAP, up to 88% of the GPS stations show WRMS reduced. The remaining stations are mostly located near coastal regions where the CWS loading displacements are relatively lower than the same amplitude of loading inland. The vertical GPS displacements are generally larger than the modelled displacements. This is partly due to the error in GPS time series or other possible physical process, which so far have not been modelled, such as local mass variation loadings.

The horizontal GPS displacements are 2-3 times the amplitude of the modelled displacements when compared to both GRACE and hydrological models, on average. For the north direction, up to 73% of the stations show a reduced WRMS after subtracting WaterGAP derived displacements, but less than a half for GRACE. The quality of the horizontal GPS observations in comparison is not as good as the vertical displacements, especially for the east direction.

Significant agreements between the displacements derived from GRACE and hy-

drological models and vertical GPS time series suggest that the CWS variation observed in vertical GPS time series and GRACE are reliable, as GPS and GRACE can be considered as independent observation techniques. Significant amplitude reduction (40% - 50%) is observed in the annual signal after subtracting GRACE from GPS. Although the GPS error amplitude is relatively high in the weekly solution, the annual signal is significant for any seasonal study.

Due to the error in the GPS time series, we re-estimate the GPS uncertainties, as the original uncertainties only represent the quality of the GPS observations rather than the quality of the displacements at the GPS site. For the inversion study, the GPS horizontal uncertainty is recalculated based on the deviation with respect to the CWS loading displacement from reference sources.

Chapter 6. Conclusions

The motivation of this thesis work was to estimate the continental water storage variations from the GPS three-dimensional observations for regional studies. Inverting the continental water storage from the GPS observations at the regional scale is a typical ill-posed inversion problem that makes the inversion scheme challenging due to the generally sparse GPS network, error in the GPS time series, and the regional mass parameterizations.

Due to the low availability of the GPS data, it is not cost efficient to pre-select GPS stations for a better network, as permanent GPS stations in most of regions are already sparse. Thus, here we focus on improving the inversion study by analyzing the unresolved signals and understanding the GPS observed time series. Then we apply our developed inversion scheme in different regions.

6.1. Unresolved signals in regional study

As there is a strong concern that there will be a likely gap between the GRACE and GRACE-Follow-On missions, the geodetic and hydrological community has started to use GPS observations for inferring continental water storage (CWS). But for regional scale inversions, the loading effect from mass changes outside the region of interest are commonly neglected (Argus et al., 2014; Fu et al., 2015). In this thesis, the spatial truncation error from this omission is discussed with various simulations. We found that for the mass loading calculation in most regions around the globe, only the load outside a specific spherical distance can be ignored.

Within the 20° degrees of a site, the vertical surface displacement driven by the CWS can be approximated as global continental water storage induced vertical motion. But for desert/dry regions where the mass load is small, a larger coverage of

mass change information is suggested. Displacements induced from the far-field can be significant as displacement from the dry regions are usually very small.

Further reduction of the spatial truncation error can be achieved if the mass load from the far-field is removed using a proper model of CWS. In our simulation, after subtracting the far field effect from the hydrological model, the spatial truncation can be reduced by up to half of its original amplitude. But in this case, mismodelling error will be introduced into the displacement time series.

In this thesis work, we estimate the CWS at the basin scale. This approximation of basin averages does not consider the mass distribution within the basins. Near-field effects show the difference in the displacements between the mean basin changes and the real mass distribution. We studied this effect in the spatial and spectral domain and found that loading displacements in the vertical are dominated by lower degree signals. Omitting this near-field effect introduces significant error into the displacements (up to 0.5 mm and 5 mm for the horizontal and vertical displacements). CWS changes in the major river basins can be determined using GPS stations within ~500 km in most regions around the globe, as about 99 percent of the displacement amplitude is from this area. The correlation of the vertical displacements derived from global mass variations and mean basin mass changes are close to 1, except for a few coastal regions.

We developed an empirical averaging kernel obtained from the hydrological model to reduce the near-field effect. This averaging kernel performs as a regional scaling parameter over the basin.

6.2. Discrepancies between GPS time series and modelled displacements

GPS has been compared with GRACE and other hydrological models in many previous studies. In this thesis, we re-examine the GPS observations for the CWS study

and provide some suggestions for the inversion.

We cross validate the GPS observations with GRACE and hydrological models and confirm the findings provided in Dong et al. (2002) that 40% -50% of the GPS observed annual amplitudes can be explained by the continental water storage loading derived displacements. Comparisons here are extended to horizontal displacements. We found that the amplitude of the horizontal GPS displacements are 2-3 times of the amplitude of the modelled displacements both for GRACE and hydrological models. In general, GPS shows a better agreement in the north than in the east.

We discussed the possible sources for these discrepancies. The contribution of thermal expansion of the bedrock explains some of the discrepancies. We exclude the local signal, thermal expansion of the bedrock and the monuments as the amplitude of these sources are much smaller than the amplitude of the discrepancies. We conclude that the main reason for the discrepancies lies in the GPS observations.

The uncertainties of the GPS time series cannot present the quality of the observed loading signals. The discrepancies between the GPS and modelled displacements are much larger than the uncertainties in the GPS time series. We suggest re-estimating the GPS uncertainties based on the discrepancies for the inversion study.

6.3. Inversion schemes and their applications

Three inversion schemes are developed in this thesis: single basin inversion, multiple basin inversion, and regularized multiple basin inversion. The single basin inversion can be applied to regions where there are located very few GPS sites but strong mass loads. This situation arises in the Amazon. The multiple basin inversion can be used to estimate CWS changes in a central basin surrounded by GPS network. This situation arises in the Danube and St. Lawrence River basin. The regularized multiple basin invasion can be used to co-estimate the basin used in the multiple basin inversion.

From the inversion scheme, we found that the continental water storage inferred from the GPS three-dimensional time series consistently agrees with the storage derived from GRACE and hydrological models. Strong correlations (0.75 in Amazon, up to 0.88 in North America and 0.80 in Europe) have been found between the inferred CWS and from reference sources. This confirms that GPS can be used to infer the water storage changes.

In this thesis, we extend the regional inversions that only make use of the vertical displacements to using three-dimensional surface displacements. Significant contributions of the horizontal displacements have been found in the inversion result, with a relative contribution about 0.3 for Danube River basin. We also found that the horizontal displacements contribute signal to the inverted results making the horizontal displacements a valuable contribution to the water storage study.

Bibliography

Abramowitz, M., and I. A. Stegun, 1964, Handbook of mathematical functions: with formulas, graphs, and mathematical tables: Courier Corporation, 55.

Agnew, D. C., 2012, SPOTL: Some programs for ocean-tide loading: La Jolla CA, University of California, Scripps Institution of Oceanography Technical Report.

Alterman, Z., H. Jarosch, and C. Pekeris, 1961, Propagation of Rayleigh waves in the Earth: Geophysical Journal International, v. 4, no. Supplement 1, p. 219–241.

Amiri-Simkooei, A. R., 2013, On the nature of GPS draconitic year periodic pattern in multivariate position time series: Journal of Geophysical Research: Solid Earth, v. 118, no. 5, p. 2500–2511, doi:10.1002/jgrb.50199.

Amiri-Simkooei, A. R., C. C. J. M. Tiberius, and P. J. G. Teunissen, 2007, Assessment of noise in GPS coordinate time series: Methodology and results: Journal of Geophysical Research, v. 112, no. B7, doi:10.1029/2006JB004913.

Amos, C. B., P. Audet, W. C. Hammond, R. Burgmann, I. A. Johanson, and G. Blewitt, 2014, Uplift and seismicity driven by groundwater depletion in central California: Nature, v. 509, no. 7501, p. 483–486.

Argus, D. F., Y. Fu, and F. W. Landerer, 2014, Seasonal variation in total water storage in California inferred from GPS observations of vertical land motion: Geophysical Research Letters, v. 41, no. 6, p. 2014GL059570, doi:10.1002/2014GL059570.

Baur, O., M. Kuhn, and W. E. Featherstone, 2009, GRACE-derived ice-mass varia-

tions over Greenland by accounting for leakage effects: Journal of Geophysical Research: Solid Earth, v. 114, no. B6, p. B06407, doi:10.1029/2008JB006239.

Bevis, M. et al., 2012, Bedrock displacements in Greenland manifest ice mass variations, climate cycles and climate change.: Proceedings of the National Academy of Sciences of the United States of America, v. 109, no. 30, doi:10.1073/pnas.1204664109.

Bevis, M., E. Kendrick, A. Cser, and R. Smalley Jr., 2004, Geodetic measurement of the local elastic response to the changing mass of water in Lago Laja, Chile: Physics of the Earth and Planetary Interiors, v. 141, no. 2, p. 71–78, doi:10.1016/j.pepi.2003.05.001.

Blewitt, G., 2003, Self-consistency in reference frames, geocenter definition, and surface loading of the solid Earth: Journal of Geophysical Research, v. 108, no. B2, p. 2103, doi:10.1029/2002JB002082.

Blewitt, G., D. Lavallée, P. Clarke, and N. Konstantin, 2001, A New Global Mode of Earth Deformation: Seasonal Cycle Detected: Science, v. 294, no. 5550, p. 2342–2345, doi:10.1126/science.1065328.

Borsa, A. A., D. C. Agnew, and D. R. Cayan, 2014, Ongoing drought-induced uplift in the western United States: Science, v. 345, no. 6204, p. 1587–1590.

Bos, M. S., R. M. S. Fernandes, S. D. P. Williams, and L. Bastos, 2013, Fast error analysis of continuous GNSS observations with missing data: Journal of Geodesy, v. 87, no. 4, p. 351–360, doi:10.1007/s00190-012-0605-0.

Boussinesq, J., 1885, Applications of potentials for the study of equilibrium and movement of elastic solids: Paris: Gautier-Villars.

Boy, J.-P., M. Llubes, J. Hinderer, and N. Florsch, 2003, A comparison of tidal ocean loading models using superconducting gravimeter data: Journal of Geophysical Research: Solid Earth, v. 108, no. B4, doi:10.1029/2002JB002050.

Chen, J., 2015, Gravity Spherical Harmonics from GLDAS Monthly Water Storage Change: <ftp://ftp.csr.utexas.edu/pub/ggfc/water/GLDAS/CS_GEO/> (accessed February 9, 2016).

Chen, J. L., C. R. Wilson, and B. D. Tapley, 2010, The 2009 exceptional Amazon flood and interannual terrestrial water storage change observed by GRACE: Water Resources Research, v. 46, no. 12, p. n/a-n/a, doi:10.1029/2010WR009383.

Cheney, E., and D. Kincaid, 2012, Numerical mathematics and computing: Cengage Learning.

Cheng, M., and B. D. Tapley, 2005, Variations in the Earth's oblateness during the past 28 years: Journal of Geophysical Research: Solid Earth, v. 109, no. B9, p. B09402, doi:10.1029/2004JB003028.

Cohenour, C., and F. Van Graas, 2011, GPS Orbit and Clock Error Distributions: Navigation, v. 58, no. 1, p. 17–28, doi:10.1002/j.2161-4296.2011.tb01789.x.

Collilieux, X., Z. Altamimi, D. Coulot, J. Ray, and P. Sillard, 2007, Comparison of very long baseline interferometry, GPS, and satellite laser ranging height residuals from ITRF2005 using spectral and correlation methods: Journal of Geophysical Research: Solid Earth, v. 112, no. B12, p. B12403, doi:10.1029/2007JB004933.

Collilieux, X., L. Métivier, Z. Altamimi, T. van Dam, and J. Ray, 2011, Quality assessment of GPS reprocessed terrestrial reference frame: GPS Solutions, v. 15, no. 3, p. 219–231, doi:10.1007/s10291-010-0184-6.

van Dam, T., G. Blewitt, and M. Heflin, 1994, Atmospheric pressure loading effects on Global Positioning System coordinate determinations: Journal of geophysical research, v. 99, no. B12, p. 23939–23950.

van Dam, T., and T. A. Herring, 1994, Detection of atmospheric pressure loading using very long baseline interferometry measurements: Journal of Geophysical Research, v. 99, no. B3, p. 4505–4517, doi:10.1029/93JB02758.

van Dam, T. M., and J. M. Wahr, 1987, Displacements of the Earth's surface due to atmospheric loading: Effects on gravity and baseline measurements: Journal of Geophysical Research: Solid Earth (1978–2012), v. 92, no. B2, p. 1281–1286.

van Dam, T., J. Wahr, and D. Lavallée, 2007, A comparison of annual vertical crustal

displacements from GPS and Gravity Recovery and Climate Experiment (GRACE) over Europe: Journal of Geophysical Research, v. 112, no. B3, p. 1–11, doi:10.1029/2006JB004335.

van Dam, T., J. Wahr, P. C. D. Milly, A. B. Shmakin, G. Blewitt, D. Lavallée, and K. M. Larson, 2001, Crustal displacements due to continental water loading: Geophysical Research Letters, v. 28, no. 4, p. 651–654, doi:10.1029/2000GL012120.

van Dam, T., X. Collilieux, J. Wuite, Z. Altamimi, and J. Ray, 2012, Nontidal ocean loading: amplitudes and potential effects in GPS height time series: Journal of Geodesy, v. 86, no. 11, p. 1043–1057, doi:10.1007/s00190-012-0564-5.

Davis, J. L., P. Elósegui, J. X. Mitrovica, and M. E. Tamisiea, 2004, Climate-driven deformation of the solid Earth from GRACE and GPS: Geophysical Research Letters, v. 31, no. 24, doi:10.1029/2004GL021435.

Döll, P., H. Hoffmann-Dobrev, F. T. Portmann, S. Siebert, A. Eicker, M. Rodell, G. Strassberg, and B. R. Scanlon, 2012, Impact of water withdrawals from groundwater and surface water on continental water storage variations: Journal of Geodynamics, v. 59–60, p. 143–156, doi:10.1016/j.jog.2011.05.001.

Döll, P., F. Kaspar, and B. Lehner, 2003, A global hydrological model for deriving water availability indicators: model tuning and validation: Journal of Hydrology, v. 270, no. 1–2, p. 105–134, doi:10.1016/S0022-1694(02)00283-4.

Dong, D., P. Fang, Y. Bock, M. K. Cheng, and S. Miyazaki, 2002, Anatomy of apparent seasonal variations from GPS-derived site position time series: Journal of Geophysical Research: Solid Earth, v. 107, no. B4, p. ETG 9-1, doi:10.1029/2001JB000573.

Dziewonski, A. M., and D. L. Anderson, 1981, Preliminary reference Earth model: Physics of the earth and planetary interiors, v. 25, no. 4, p. 297–356.

Famiglietti, J. S., M. Lo, S. L. Ho, J. Bethune, K. J. Anderson, T. H. Syed, S. C. Swenson, C. R. de Linage, and M. Rodell, 2011, Satellites measure recent rates of groundwater depletion in California's Central Valley: Geophysical Research Letters, v. 38, no. 3, p. L03403, doi:10.1029/2010GL046442.

Famiglietti, J. S., J. W. Rudnicki, and M. Rodell, 1998, Variability in surface moisture content along a hillslope transect: Rattlesnake Hill, Texas: Journal of Hydrology, v. 210, no. 1–4, p. 259–281, doi:10.1016/S0022-1694(98)00187-5.

Fang, M., D. Dong, and B. H. Hager, 2014, Displacements due to surface temperature variation on a uniform elastic sphere with its centre of mass stationary: Geophysical Journal International, v. 196, no. 1, p. 194–203.

Farrell, W. E., 1972, Deformation of the Earth by surface loads: Reviews of Geophysics, v. 10, no. 3, p. 761, doi:10.1029/RG010i003p00761.

Farrell, W. E., 1973, Earth tides, ocean tides and tidal loading: Philosophical Transactions of the Royal Society of London A: Mathematical, Physical and Engineering Sciences, v. 274, no. 1239, p. 253–259.

Flouzat, M., P. Bettinelli, P. Willis, J.-P. Avouac, T. Héritier, and U. Gautam, 2009, Investigating tropospheric effects and seasonal position variations in GPS and DORIS time-series from the Nepal Himalaya: Geophysical Journal International, v. 178, no. 3, p. 1246–1259, doi:10.1111/j.1365-246X.2009.04252.x.

Francis, O., and V. Dehant, 1987, Recomputation of the Green's functions for tidal loading estimations: Marées terrestres, no. 100, p. 6962–6986.

Fritsche, M., P. Döll, and R. Dietrich, 2012, Global-scale validation of model-based load deformation of the Earth's crust from continental watermass and atmospheric pressure variations using GPS: Journal of Geodynamics, v. 59–60, p. 133–142, doi:10.1016/j.jog.2011.04.001.

Fu, Y., D. F. Argus, and F. W. Landerer, 2015, GPS as an independent measurement to estimate terrestrial water storage variations in Washington and Oregon: Journal of Geophysical Research: Solid Earth, v. 120, no. 1, p. 2014JB011415, doi:10.1002/2014JB011415.

Fukumori, I., 2002, A Partitioned Kalman Filter and Smoother: Monthly Weather Review, v. 130, no. 5, p. 1370–1383, doi:10.1175/1520-0493(2002)130<1370:APKFAS>2.0.CO;2.

Gegout, P., 2013, Modeling and Mitigating Loading Effects on Geodetic Sites, *in* Vienna, Austria: p. 9216.

Greatbatch, R. J., 1994, A note on the representation of steric sea level in models that conserve volume rather than mass: Journal of Geophysical Research, v. 99, no. C6, p. 12767, doi:10.1029/94JC00847.

Griffiths, J., and J. R. Ray, 2013, Sub-daily alias and draconitic errors in the IGS orbits: GPS Solutions, v. 17, no. 3, p. 413–422, doi:10.1007/s10291-012-0289-1.

Hansen, P. C., 2010, Discrete inverse problems: insight and algorithms: Philadelphia, Society for Industrial and Applied Mathematics, Fundamentals of algorithms, 213 p.

Hansen, P. C., 1998, Rank-deficient and discrete ill-posed problems: numerical aspects of linear inversion: Philadelphia, Pa, SIAM.

Hao, M., J. T. Freymueller, Q. Wang, D. Cui, and S. Qin, 2016, Vertical crustal movement around the southeastern Tibetan Plateau constrained by GPS and GRACE data: Earth and Planetary Science Letters, v. 437, p. 1–8, doi:10.1016/j.epsl.2015.12.038.

Heiskanen, W. A., and H. Moritz, 1967, Physical geodesy: Bulletin géodésique, v. 86, no. 1, p. 491–492, doi:10.1007/BF02525647.

Heki, K., 2001, Seasonal Modulation of Interseismic Strain Buildup in Northeastern Japan Driven by Snow Loads: Science, v. 293, no. 5527, p. 89–92.

Hirschi, M., S. I. Seneviratne, S. Hagemann, and C. Schär, 2007, Analysis of seasonal terrestrial water storage variations in regional climate simulations over Europe: Journal of Geophysical Research: Atmospheres, v. 112, no. D22, p. D22109, doi:10.1029/2006JD008338.

Hirschi, M., S. I. Seneviratne, and C. Schär, 2006, Seasonal Variations in Terrestrial Water Storage for Major Midlatitude River Basins: Journal of Hydrometeorology, v. 7, no. 1, p. 39–60, doi:10.1175/JHM480.1.

Hirschi, M., P. Viterbo, and S. I. Seneviratne, 2006, Basin-scale water-balance esti-

mates of terrestrial water storage variations from ECMWF operational forecast analysis: Geophysical Research Letters, v. 33, no. 21, p. 1–6, doi:10.1029/2006GL027659.

Houborg, R., M. Rodell, B. Li, R. Reichle, and B. F. Zaitchik, 2012, Drought indicators based on model-assimilated Gravity Recovery and Climate Experiment (GRACE) terrestrial water storage observations: Water Resources Research, v. 48, no. 7, p. n/a-n/a, doi:10.1029/2011WR011291.

Huang, J., J. Halpenny, W. van der Wal, C. Klatt, T. S. James, and a. Rivera, 2012, Detectability of groundwater storage change within the Great Lakes Water Basin using GRACE: Journal of Geophysical Research, v. 117, no. B8, p. 1–26, doi:10.1029/2011JB008876.

Jackson, T. J., and D. E. Le Vine, 1996, Mapping surface soil moisture using an aircraft-based passive microwave instrument: algorithm and example: Soil Moisture Theories and Observations, v. 184, no. 1–2, p. 85–99, doi:10.1016/0022-1694(95)02969-9.

Jansen, M. J. F., B. C. Gunter, and J. Kusche, 2009, The impact of GRACE, GPS and OBP data on estimates of global mass redistribution: Geophysical Journal International, v. 177, no. 1, p. 1–13, doi:10.1111/j.1365-246X.2008.04031. x.

Jiang, W., Z. Li, T. van Dam, and W. Ding, 2013, Comparative analysis of different environmental loading methods and their impacts on the GPS height time series: Journal of Geodesy, v. 87, no. 7, p. 687–703, doi:10.1007/s00190-013-0642-3.

Kalnay, E. et al., 1996, The NCEP/NCAR 40-Year Reanalysis Project: Bulletin of the American Meteorological Society, v. 77, no. 3, p. 437–471, doi:10.1175/1520-0477(1996)077<0437:TNYRP>2.0.CO;2.

Kim, S.-B., T. Lee, and I. Fukumori, 2007, Mechanisms Controlling the Interannual Variation of Mixed Layer Temperature Averaged over the Niño-3 Region: Journal of Climate, v. 20, no. 15, p. 3822–3843, doi:10.1175/JCLI4206.1.

Kusche, J., and E. J. O. Schrama, 2005, Surface mass redistribution inversion from global GPS deformation and Gravity Recovery and Climate Experiment

(GRACE) gravity data: Journal of Geophysical Research, v. 110, no. B9, p. 1–14, doi:10.1029/2004JB003556.

Kusche, J., E. J. O. Schrama, and M. J. F. Jansen, 2007, Continental hydrology retrieval from GPS time series and GRACE gravity solutions, *in* P. Tregoning, and C. Rizos, eds., Dynamic Planet: Springer Berlin Heidelberg, International Association of Geodesy Symposia, p. 517–522.

Landerer, F. W., and S. C. Swenson, 2012, Accuracy of scaled GRACE terrestrial water storage estimates: Water Resources Research, v. 48, no. 4, p. W04531, doi:10.1029/2011WR011453.

Li, B., M. Rodell, B. F. Zaitchik, R. H. Reichle, R. D. Koster, and T. M. van Dam, 2012, Assimilation of GRACE terrestrial water storage into a land surface model: Evaluation and potential value for drought monitoring in western and central Europe: Journal of Hydrology, v. 446–447, no. 0, p. 103–115, doi:10.1016/j.jhydrol.2012.04.035.

Lomb, N. R., 1976, Least-squares frequency analysis of unequally spaced data: Astrophysics and space science, v. 39, no. 2, p. 447–462.

Long, D., B. R. Scanlon, L. Longuevergne, A. Y. Sun, D. N. Fernando, and H. Save, 2013, GRACE satellite monitoring of large depletion in water storage in response to the 2011 drought in Texas: GRACE-BASED DROUGHT MONITORING: Geophysical Research Letters, v. 40, no. 13, p. 3395–3401, doi:10.1002/grl.50655.

Longman, I. M., 1963, A Green's function for determining the deformation of the Earth under surface mass loads: 2. Computations and numerical results: Journal of Geophysical Research, v. 68, no. 2, p. 485–496, doi:10.1029/JZ068i002p00485.

Love, A. E. H., 1909, The Yielding of the Earth to Disturbing Forces: Proceedings of the Royal Society of London. Series A, Containing Papers of a Mathematical and Physical Character, v. 82, no. 551, p. 73–88.

Lutgens, F. K., E. J. Tarbuck, and D. Tasa, 1995, Essentials of geology: Prentice Hall.

Mayer-Gürr, T., N. Zehentner, B. Klinger, and A. Kvas, 2014, ITSG-Grace2014: a

new GRACE gravity field release computed in Graz, *in* GRACE science team meeting (GSTM).

McMillan, M., H. Corr, A. Shepherd, A. Ridout, S. Laxon, and R. Cullen, 2013, Three-dimensional mapping by CryoSat-2 of subglacial lake volume changes: Geophysical Research Letters, p. n/a-n/a, doi:10.1002/grl.50689.

Merriam, J. B., 1992, Atmospheric pressure and gravity: Geophysical Journal International, v. 109, no. 3, p. 488–500, doi:10.1111/j.1365-246X.1992.tb00112.x.

Moritz, H., 1980, Advanced physical geodesy: Advances in Planetary Geology, v. 1.

Müller Schmied, H., S. Eisner, D. Franz, M. Wattenbach, F. T. Portmann, M. Flörke, and P. Döll, 2014, Sensitivity of simulated global-scale freshwater fluxes and storages to input data, hydrological model structure, human water use and calibration: Hydrol. Earth Syst. Sci. Discuss., v. 11, no. 2, p. 1583–1649, doi: 10 5194/hessd-11-1583-2014.

Muskett, R. R., and V. E. Romanovsky, 2011, Alaskan Permafrost Groundwater Storage Changes Derived from GRACE and Ground Measurements: Remote Sensing, v. 3, no. 2, p. 378–397, doi:10.3390/rs3020378.

Petrov, L., and J.-P. Boy, 2004, Study of the atmospheric pressure loading signal in very long baseline interferometry observations: Journal of Geophysical Research: Solid Earth, v. 109, no. B3, p. B03405, doi:10.1029/2003JB002500.

Petrov, Yu. P., and V. S. Sizikov., 2005, Well-posed, ill-posed, and intermediate problems with applications: De Gruyter Mouton.

Plag, H., and T. van Dam, 2002, Solid Earth deformation and gravity changes due to surface loading: Status and scientific problems: IERS Workshop on Combination Research and \ldots, p. 1–22.

Ray, J., Z. Altamimi, X. Collilieux, and T. van Dam, 2008, Anomalous harmonics in the spectra of GPS position estimates: GPS Solutions, v. 12, no. 1, p. 55–64, doi:10.1007/s10291-007-0067-7.

Ray, J., X. Collilieux, P. Rebischung, T. M. van Dam, and Z. Altamimi, 2011, Consistency of crustal loading signals derived from models and GPS: Inferences for GPS positioning errors, Invited abstract G51B-06: San Francisco, USA.

Reager, J. T., and J. S. Famiglietti, 2009, Global terrestrial water storage capacity and flood potential using GRACE: Geophysical Research Letters, v. 36, no. 23, doi:10.1029/2009GL040826.

Rietbroek, R., 2014, Retrieval of Sea Level and Surface Loading Variations from Geodetic Observations and Model Simulations, phdthesis: Universitäts-und Landesbibliothek Bonn.

Rietbroek, R., M. Fritsche, S.-E. Brunnabend, I. Daras, J. Kusche, J. Schröter, F. Flechtner, and R. Dietrich, 2012, Global surface mass from a new combination of GRACE, modelled OBP and reprocessed GPS data: Journal of Geodynamics, v. 59–60, p. 64–71, doi:10.1016/j.jog.2011.02.003.

Rodell, M. et al., 2004, The Global Land Data Assimilation System: Bulletin of the American Meteorological Society, v. 85, no. 3, p. 381–394, doi:10.1175/BAMS-85-3-381.

Rodell, M., and J. S. Famiglietti, 1999, Detectability of variations in continental water storage from satellite observations of the time dependent gravity field: Water Resources Research, v. 35, no. 9, p. 2705–2723, doi:10.1029/1999WR900141.

Rodell, M., I. Velicogna, and J. S. Famiglietti, 2009, Satellite-based estimates of groundwater depletion in India: Nature, v. 460, no. 7258, p. 999–1002, doi:10.1038/nature08238.

Rosenbaum, U., H. R. Bogena, M. Herbst, J. A. Huisman, T. J. Peterson, A. Weuthen, A. W. Western, and H. Vereecken, 2012, Seasonal and event dynamics of spatial soil moisture patterns at the small catchment scale: Water Resources Research, v. 48, no. 10, p. W10544, doi:10.1029/2011WR011518.

Sakumura, C., S. Bettadpur, and S. Bruinsma, 2014, Ensemble prediction and intercomparison analysis of GRACE time-variable gravity field models: Geophysical Research Letters, v. 41, no. 5, p. 1389–1397, doi:10.1002/2013GL058632.

Sauber, J., G. Plafker, B. F. Molnia, and M. A. Bryant, 2000, Crustal deformation associated with glacial fluctuations in the eastern Chugach Mountains, Alaska: Journal of Geophysical Research: Solid Earth, v. 105, no. B4, p.

8055–8077, doi:10.1029/1999JB900433.

Schmid, R., and M. Rothacher, 2003, Estimation of elevation-dependent satellite antenna phase center variations of GPS satellites: Journal of Geodesy, v. 77, no. 7–8, p. 440–446, doi:10.1007/s00190-003-0339-0.

Schmid, R., P. Steigenberger, G. Gendt, M. Ge, and M. Rothacher, 2007, Generation of a consistent absolute phase center correction model for GPS receiver and satellite antennas: Journal of Geodesy, v. 81, no. 12, p. 781–798, doi:10.1007/s00190-007-0148-y.

Schrama, E. J., 2005, Three algorithms for the computation of tidal loading and their numerical accuracy: Journal of Geodesy, v. 78, no. 11–12, p. 707–714.

Schüler, T., 2001, On ground-based GPS tropospheric delay estimation, Ph.D: Universitat der Bundeswehr Munchen.

Seitz, F., and M. Krügel, 2009, Inverse Model Approach for vertical Load Deformations in Consideration of Crustal Inhomogeneities, *in* H. Drewes, ed., Geodetic Reference Frames: Berlin, Heidelberg, Springer Berlin Heidelberg, p. 23–29.

Sjöberg, L. E., 2005, A discussion on the approximations made in the practical implementation of the remove–compute–restore technique in regional geoid modelling: Journal of Geodesy, v. 78, no. 11, p. 645–653, doi:10.1007/s00190-004-0430-1.

Sneeuw, N., 2000, A Semi-Analytical Approach to Gravity Field Analysis from Satellite Observations, Dissertation: München, Technische Universität München.

Sneeuw, N., 2006, Physical geodesy: Institute of Geodesy, Stuttgart University.

Spratt, R. S., 1982, Modelling the effect of atmospheric pressure variations on gravity: Geophysical Journal International, v. 71, no. 1, p. 173–186, doi:10.1111/j.1365-246X.1982.tb04991.x.

Steckler, M. S., S. L. Nooner, S. H. Akhter, S. K. Chowdhury, S. Bettadpur, L. Seeber, and M. G. Kogan, 2010, Modeling Earth deformation from monsoonal flooding in Bangladesh using hydrographic, GPS, and Gravity Recovery and Climate Experiment (GRACE) data: Journal of Geophysical Research: Solid

Earth, v. 115, no. B8, p. B08407, doi:10.1029/2009JB007018.

Swenson, S., D. Chambers, and J. Wahr, 2008, Estimating geocenter variations from a combination of GRACE and ocean model output: Journal of Geophysical Research: Solid Earth, v. 113, no. B8, p. B08410, doi:10.1029/2007JB005338.

Swenson, S. C., and P. C. D. Milly, 2006, Climate model biases in seasonality of continental water storage revealed by satellite gravimetry: Water Resources Research, v. 42, no. 3, p. W03201, doi:10.1029/2005WR004628.

Swenson, S., and J. Wahr, 2002, Methods for inferring regional surface-mass anomalies from Gravity Recovery and Climate Experiment (GRACE) measurements of time-variable gravity: Journal of Geophysical Research: Solid Earth (1978–2012), v. 107, no. B9, p. ETG–3.

Swenson, S., and J. Wahr, 2006, Post-processing removal of correlated errors in GRACE data: Geophysical Research Letters, v. 33, no. 8, p. L08402, doi:10.1029/2005GL025285.

Swenson, S., J. Wahr, and P. C. D. Milly, 2003, Estimated accuracies of regional water storage variations inferred from the Gravity Recovery and Climate Experiment (GRACE): REGIONAL WATER STORAGE ESTIMATES FROM GRACE: Water Resources Research, v. 39, no. 8, p. n/a-n/a, doi:10.1029/2002WR001808.

Tapley, B. D., S. Bettadpur, J. C. Ries, P. F. Thompson, and M. M. Watkins, 2004, GRACE measurements of mass variability in the Earth system.: Science (New York, N.Y.), v. 305, no. 5683, p. 503–5, doi:10.1126/science.1099192.

Tesmer, V., P. Steigenberger, T. van Dam, and T. Mayer-Gürr, 2011, Vertical deformations from homogeneously processed GRACE and global GPS long-term series: Journal of Geodesy, v. 85, no. 5, p. 291–310, doi:10.1007/s00190-010-0437-8.

Tesmer, V., P. Steigenberger, M. Rothacher, J. Boehm, and B. Meisel, 2009, Annual deformation signals from homogeneously reprocessed VLBI and GPS height time series: Journal of Geodesy, v. 83, no. 10, p. 973–988, doi:10.1007/s00190-009-0316-3.

Teunissen, P. J., 2000, Adjustment theory: an introduction: Delft University Press Delft.

Teunissen, P. J. G., and A. R. Amiri-Simkooei, 2008, Least-squares variance component estimation: Journal of Geodesy, v. 82, no. 2, p. 65–82.

Thomas, A. C., J. T. Reager, J. S. Famiglietti, and M. Rodell, 2014, A GRACE-based water storage deficit approach for hydrological drought characterization: Geophysical Research Letters, v. 41, no. 5, p. 1537–1545, doi:10.1002/2014GL059323.

Tikhonov, A. N., and V. I. A. Arsenin, 1977, Solutions of ill-posed problems: Winston, Scripta series in mathematics.

Tregoning, P., and C. Watson, 2009, Atmospheric effects and spurious signals in GPS analyses: Journal of Geophysical Research, v. 114, no. B9, p. 1–15, doi:10.1029/2009JB006344.

Tregoning, P., C. Watson, G. Ramillien, H. McQueen, and J. Zhang, 2009, Detecting hydrologic deformation using GRACE and GPS: Geophysical Research Letters, v. 36, no. 15, p. L15401, doi:10.1029/2009GL038718.

Velicogna, I., 2009, Increasing rates of ice mass loss from the Greenland and Antarctic ice sheets revealed by GRACE: Geophysical Research Letters, v. 36, no. 19, p. L19503, doi:10.1029/2009GL040222.

Velicogna, I., and J. Wahr, 2005, Greenland mass balance from GRACE: Geophysical Research Letters, v. 32, no. 18, p. L18505, doi:10.1029/2005GL023955.

Velicogna, I., and J. Wahr, 2013, Time-variable gravity observations of ice sheet mass balance: Precision and limitations of the GRACE satellite data: Geophysical Research Letters, v. 40, no. 12, p. 3055–3063, doi:10.1002/grl.50527.

Wahr, J., T. van Dam, K. Larson, and O. Francis, 2001, GPS measurements of vertical crustal motion in Greenland: Journal of Geophysical Research, v. 106, no. D24, p. 33755–33759, doi:10.1029/2001JD900154.

Wahr, J., S. A. Khan, T. van Dam, L. Liu, J. H. van Angelen, M. R. van den Broeke, and C. M. Meertens, 2013, The use of GPS horizontals for loading studies,

with applications to northern California and southeast Greenland: Journal of Geophysical Research: Solid Earth, v. 118, no. 4, p. 1795–1806, doi:10.1002/jgrb.50104.

Wahr, J., M. Molenaar, and F. Bryan, 1998, Time variability of the Earth's gravity field: Hydrological and oceanic effects and their possible detection using GRACE: Journal of Geophysical Research, v. 103, no. B12, p. 30205–30229, doi:10.1029/98JB02844.

Wang, H.-S., L.-W. Xiang, P. Wu, H. Steffen, L. Jia, L.-M. Jiang, and Q. Shen, 2013, Effects of the Tibetan Plateau Crustal Structure on the Inversion of Water Trend Rates Using Simulated GRACE/GPS Data: Terrestrial, Atmospheric and Oceanic Sciences, v. 24, no. 4I, p. 505–512.

Williams, S. D. P., 2004, Error analysis of continuous GPS position time series: Journal of Geophysical Research, v. 109, no. B3, doi:10.1029/2003JB002741.

Williams, S. D. P., 2003, The effect of coloured noise on the uncertainties of rates estimated from geodetic time series: Journal of Geodesy, v. 76, no. 9–10, p. 483–494, doi:10.1007/s00190-002-0283-4.

Wouters, B., D. Chambers, and E. J. O. Schrama, 2008, GRACE observes small-scale mass loss in Greenland: Geophysical Research Letters, v. 35, no. 20, doi:10.1029/ 2008GL034816.

Wu, X., 2003, Large-scale global surface mass variations inferred from GPS measurements of load-induced deformation: Geophysical Research Letters, v. 30, no. 14, p. 1–4, doi:10.1029/2003GL017546.

Wu, X., M. B. Heflin, E. R. Ivins, D. F. Argus, and F. H. Webb, 2003, Large-scale global surface mass variations inferred from GPS measurements of load-induced deformation: Geophysical Research Letters, v. 30, no. 14, doi:10.1029/2003GL017546.

Wu, X., M. B. Heflin, H. Schotman, B. L. A. Vermeersen, D. Dong, R. S. Gross, E. R. Ivins, A. W. Moore, and S. E. Owen, 2010, Simultaneous estimation of global present-day water transport and glacial isostatic adjustment: Nature Geosci, v. 3, no. 9, p. 642–646, doi:10.1038/ngeo938.

Wu, X., J. Ray, and T. van Dam, 2012, Geocenter motion and its geodetic and geophysical implications: Journal of Geodynamics, v. 58, no. 0, p. 44–61, doi:10.1016/ j.jog.2012.01.007.

Yan, H., W. Chen, and L. Yuan, 2016, Crustal vertical deformation response to different spatial scales of GRACE and GCMs surface loading: Geophysical Journal International, v. 204, no. 1, p. 505–516, doi:10.1093/gji/ggv385.

Yan, H., W. Chen, Y. Zhu, W. Zhang, and M. Zhong, 2009, Contributions of thermal expansion of monuments and nearby bedrock to observed GPS height changes: Geophysical Research Letters, v. 36, no. 13, p. 1–5, doi:10.1029/2009GL038152.

Appendix A. GPS stations used in North America

ID	latitude (degree)	longitude (degree)	ID	latitude (degree)	longitude (degree)
ADKS	29.79	264.41	NANO	49.30	235.91
AL70	31.78	274.04	NCDK	36.18	284.25
ALBH	48.39	236.51	NCG1	36.07	280.26
ALGO	45.96	281.93	NCG5	36.07	280.26
ANP1	39.01	283.39	NDBC	30.36	270.39
ANTO	29.49	261.42	NETP	29.79	264.67
AOML	25.74	279.84	NIST	40.00	254.74
ARP3	27.84	262.94	NISU	40.00	254.74
ASHV	35.60	277.45	NJI2	40.74	285.82
AUS5	30.31	262.24	NLIB	41.77	268.43
AZCN	36.84	252.09	NPRI	41.51	288.67
AZCO	31.39	250.07	NRC1	45.45	284.38
BAIE	49.19	291.74	ODS5	31.87	257.69
BAKE	64.32	264.00	P105	39.39	247.50
BARH	44.40	291.78	P121	41.80	247.30
BAYR	43.45	276.11	PASO	31.77	253.59
BEA5	30.16	265.82	PATT	31.78	264.28
BLYT	33.61	245.29	PGC5	48.65	236.55
BREW	48.13	240.32	PICL	51.48	269.84
CAGS	45.59	284.19	PIE1	34.30	251.88
CCV3	28.46	279.46	PNCY	30.21	274.32
CHA1	32.76	280.16	PRDS	50.87	245.71
CHB1	45.65	275.53	PSU1	40.81	282.15
CHL1	38.78	284.91	PUC1	39.60	249.19
CHR1	36.93	283.99	QIKI	67.56	295.97
CHUR	58.76	265.91	RED1	39.56	284.43
CORC	27.74	262.56	RESO	74.69	265.11
CPXF	46.84	237.74	SAG1	43.63	276.16
DNRC	39.16	284.48	SASK	52.20	253.60
DRAO	49.32	240.38	SAV1	32.14	278.30

ID	latitude (degree)	longitude (degree)	ID	latitude (degree)	longitude (degree)
DUCK	36.18	284.25	SEAT	47.65	237.69
DWH1	47.77	237.92	SHE2	46.22	295.45
DYER	37.74	241.96	SHK1	40.47	285.99
EKY1	27.60	277.24	SOL1	38.32	283.55
ENG1	29.88	270.06	STB1	44.80	272.69
EPRT	44.91	293.01	STJO	47.60	307.32
ESCU	47.07	295.20	SUM1	34.83	257.49
FLIN	54.73	258.02	TN22	35.39	274.62
FMC1	34.70	283.32	TXES	32.37	263.14
FRDN	45.93	293.34	UNIV	42.29	275.61
GAL1	29.33	265.26	USMX	29.82	250.32
GLPT	37.25	283.50	USNA	38.98	283.52
GODE	39.02	283.17	USNO	38.92	282.93
HAMM	30.51	269.53	VALD	48.10	282.44
HLFX	44.68	296.39	VCIO	36.07	260.78
HNPT	38.59	283.87	VIMS	37.61	284.31
HOUS	29.78	264.57	VTSP	43.28	287.52
IDDR	43.75	248.89	WDC1	38.92	282.93
IQAL	63.76	291.49	WDC3	38.92	282.93
JCT1	30.48	260.20	WES2	42.61	288.51
KELS	46.12	237.10	WILL	52.24	237.83
KJUN	30.22	267.96	WIS1	46.71	267.99
KUUJ	55.28	282.26	WNFL	31.90	267.22
KYSC	37.06	275.38	WSLR	50.13	237.08
LEBA	39.43	275.72	YELL	62.48	245.52
LKHU	29.91	264.85	YESX	28.38	251.08
LUMC	29.26	269.34	AMCX	38.80	255.48
MCD1	27.85	277.47	ANGX	29.30	264.52
MDO1	30.68	255.99	MCNX	32.70	276.44
MEM2	35.47	269.79	MLFX	32.09	272.61
MIL1	43.00	272.11	PORX	43.07	289.29
MOB1	30.23	271.98	UNBX	45.95	293.36
NAIN	56.54	298.31	USNX	38.92	282.93
			MIAX	25.73	279.84

Appendix B. GPS stations used in Europe

ID	latitude (degree)	longitude (degree)	ID	latitude (degree)	longitude (degree)
ABER	57.14	357.92	MOPI	48.37	17.27
ALAC	38.34	359.52	MORP	55.21	358.32
ALME	36.85	357.54	NEWL	50.10	354.46
ANKR	39.89	32.76	NPLD	51.42	359.66
ANTA	36.83	30.61	NSSP	40.23	44.50
BELL	41.60	1.40	NSTG	55.01	358.56
BOGI	52.48	21.04	OBET	48.08	11.28
BOGO	52.48	21.04	ONSA	57.40	11.93
BOR1	52.28	17.07	OPMT	48.84	2.34
BORK	53.56	6.75	ORID	41.13	20.79
BRST	48.38	355.50	OS0G	57.40	11.93
BRUS	50.80	4.36	PADO	45.41	11.90
BUCU	44.46	26.13	PENC	47.79	19.28
BUDP	55.74	12.50	POLV	49.60	34.54
BZRG	46.50	11.34	POTS	52.38	13.07
CANT	43.47	356.20	PTBB	52.30	10.46
CEBR	40.45	355.63	REDU	50.00	5.15
CHIZ	46.13	359.59	RIGA	56.95	24.06
COSE	39.20	16.31	SASS	54.51	13.64
COST	44.16	28.66	SCOA	43.40	358.32
CRAO	44.41	33.99	SHEE	51.45	0.74
CREU	42.32	3.32	SJDV	45.88	4.68
DLFT	51.99	4.39	SKE0	64.88	21.05
DRES	51.03	13.73	SOFI	42.56	23.40
DUBR	42.65	18.11	SPLT	43.51	16.44
EBRE	40.82	0.49	SPT0	57.72	12.89
EIJS	50.76	5.68	STAS	59.02	5.60
FFMJ	50.09	8.67	SULP	49.84	24.01
GANP	49.04	20.32	SVTL	60.53	29.78
GENO	44.42	8.92	TERS	53.36	5.22

ID	latitude (degree)	longitude (degree)	ID	latitude (degree)	longitude (degree)
GLSV	50.36	30.50	TGDE	58.01	7.56
GOPE	49.91	14.79	TORI	45.06	7.66
GRAS	43.76	6.92	TRAB	41.00	39.78
GRAZ	47.07	15.49	TRON	63.37	10.32
HELG	54.17	7.89	TUBI	40.79	29.45
HERS	50.87	0.34	UNPG	43.12	12.36
HERT	50.87	0.33	UPAD	45.41	11.88
HFLK	47.31	11.39	UZHL	48.63	22.30
HOER	54.76	8.29	VAAS	62.96	21.77
HRM2	51.45	358.72	VALE	39.48	359.66
HRRN	37.18	39.00	VENE	45.44	12.33
IENG	45.02	7.64	VIL0	64.70	16.56
ISTA	41.10	29.02	VILL	40.44	356.05
JOEN	62.39	30.10	VIS0	57.65	18.37
JOZ2	52.10	21.03	VLUC	40.23	15.27
JOZE	52.10	21.03	WAB2	46.92	7.46
KARL	49.01	8.41	WARN	54.17	12.10
KHAR	50.01	36.24	WLAD	54.80	18.42
KLPD	55.72	21.12	WROC	51.11	17.06
KOSG	52.18	5.81	WSRT	52.92	6.61
LAMA	53.89	20.67	WTZA	49.14	12.88
LROC	46.16	358.78	WTZJ	49.14	12.88
M0SE	41.89	12.49	WTZR	49.14	12.88
MAD2	40.43	355.75	WTZS	49.15	12.88
MAR6	60.60	17.26	WTZT	49.14	12.88
MARS	43.28	5.35	WTZZ	49.14	12.88
MAT1	40.65	16.71	YEBE	40.53	356.91
MATE	40.65	16.70	ZECK	43.79	41.57
MDVJ	56.02	37.22	ZIM2	46.88	7.47
MDVO	56.03	37.22	ZIMM	46.88	7.47
MEDI	44.52	11.65	ZWE2	55.70	36.76
MERS	36.57	34.26	ZWEN	55.70	36.76
METS	60.22	24.40	OBEX	48.09	11.28
METZ	60.22	24.40	PFAX	47.52	9.79
MIKL	46.97	31.97	TLSX	43.56	1.48

MOBJ	55.12	36.57	ZIMX	46.88	7.47
MOBN	55.12	36.57			